## *Structural studies on Functional Materials using Solid-State NMR, Powder X-ray Diffraction and DFT Calculations*

SOLEILHAVOUP, ANNE

# Structural studies on Functional Materials using Solid-State NMR, Powder X-ray Diffraction and DFT Calculations

Anne Soleilhavoup

Durham University

Supervisors : Dr. Paul Hodgkinson and Prof. John S. O. Evans

Ph.D.Thesis

Department of Chemistry

Durham University

2009

## Declaration of statement and copyright

The work described in this thesis is entirely my own, except where I have acknowledged help from a named person or given a reference to a published source or a thesis.

The research presented was performed in the Department of Chemistry, University of Durham between January 2006 and January 2009, the results of which have not been submitted for a degree in this or any other university. This thesis conforms to the word limit set out in the Degree Regulations of the University.

# Glossary of symbols and abbreviations

| | |
|---|---|
| NMR | Nuclear Magnetic Resonance |
| $I$ | spin quantum number |
| $\gamma$ | gyromagnetic ratio |
| $B_0$ | external magnetic field |
| PAS | Principal Axes System |
| JIS | J-coupling between spins I and S |
| CSA | Chemical Shift Anisotropy |
| EFG | Electric Field Gradient |
| MAS | Magic Angle Spinning |
| SQ | Single Quantum |
| DQ | Double Quantum |
| INADEQUATE | Incredible Natural Abundance DoublE QUAntum Transfer Experiment |
| DFT | Density Functional Theory |
| LDA | Local Density Approximation |
| GGA | Gradient Generalised Approximation |
| DLS | Distance Least Squares |
| TOBSY | TOtal through-Bond correlation SpectroscopY |
| RFDR | Radio-Frequency-Driven Recoupling |
| ppm | part per million |
| GIPAW | Gauge Including Projector Augmented Waves |
| eV | Electron Volt |
| NTE | Negative Thermal Expansion |
| RUM | Rigid Unit Modes |
| QRUM | Quasi Rigid Unit Modes |
| EXAFS | Extended X-ray absorption fine structure |
| PIA | Pressure Induced Amorphisation |
| XANES | X-ray Absorption Near Edge Structure |
| XAS | X-ray Absorption Spectroscopy |
| PTFE | PolyTetraFluoroEthylene |
| RMC | Reverse Monte-Carlo |

# Acknowledgements

My first and sincere regards go to Dr. Paul Hodgkinson and Prof. John S.O. Evans who warmly welcomed me as part of their research groups. This work was largely achieved thanks to their kind supervision and their support.

This work also involved several collaborations which were concluded by some of the reported results. I would therefore like to thank Dr. Stewart Clark for his precious advices and explanations on the CASTEP code, Dr. Mark Fox for performing GAUSSIAN calculations, Dr. Matthew Tucker for the conversion of $ZrW_2O_8$ into its high pressure form of and Dr. Rob Schurko for his $^{91}Zr$ NMR investigations on $ZrW_2O_8$ (although not presented in this thesis).

Being part of two research groups, I got the chance to meet and work close to their members over this period. I would therefore like to address many grateful thoughts to Prof. Robin K. Harris, Dr. David Apperley and Fraser Markwell for their amiability and friendly sharing of knowledge. I also really want to thank my colleagues and friends from the SSNMR group and the "Evans team": Vadim, Sarah, Andy I, Andy R, Tim, Graham, Loc, Lars, Dave, Julia, Anuji, Sam, Xiaojun, Abdullah, Allan, Deborah, Paul, Jeay, Naomi, Charles, May, Tom, Francesca, Erin, Alex, Oliver, Yuandi, Victoria, Zoe.

These acknowledgements need to be completed by an additional list of friends who, thanks to their support, also contributed to the fulfilment of this work: Milena, Yoyo, Elena, Alessandra, Laura, Elisa, Ben, Peter, Julie, Linda, Barbara, Sandrine, Laurent, Ry, Cécile, Maykel, Farhan, Jesus, Zhanglu and many others.

A ma famille,

# Abstract

**Chapter 1** gives a brief description of the main analytical and theoretical techniques used in this work. After an overview of solid-state NMR, the INADEQUATE and POST-C7 experiments performed in our $^{31}P$ studies are explained. The DFT method and its application to NMR problems using the CASTEP software package is also introduced. Basic powder X-ray diffraction concepts and their use in the DLS (Distance Least Square) method are also explained.

**Chapter 2** reviews some of the previous studies using $^{17}O$ and $^{31}P$ solid state NMR relevant to this work. Finally, the optimisation procedure of the different parameters used for the CASTEP calculations is explained.

**Chapter 3** looks at the structures of $(MoO_2)_2P_2O_7$ pyrophosphate. One dimensional variable temperature MAS NMR experiments clearly show the existence of a phase transition between 150°C and room temperature passing via an incommensurate phase. As the temperature decreases, the symmetry of the high temperature phase lowers leading to a superstructure almost indistinguishable in the diffraction data. However, these room temperature data can be refined against several possible model structures with 1D and 2D NMR experiments being used to distinguish between these models.

The J-coupling driven experiments (spin-echo, refocused INADEQUATE) have been shown to be useful to obtain information on $P_2O_7$ units. The INADEQUATE experiment was used to highlight through bonds connectivities within such units while the spin-echo experiment was mainly used to measure J-coupling values related to P-O-P bond angles.

The dipolar coupling driven experiments (POST C7) are used to look at short and long spatial interactions between $^{31}P$ sites within the structure. Indeed, the dipolar couplings between the different $^{31}P$ sites can be analytically determined and related to the 2D experiments.

**Chapter 4** presents the work done on the three $^{17}O$ labelled phases of $ZrW_2O_8$ synthesised under different pressure conditions. One-dimensional NMR spectra and CASTEP calculations of the two crystalline phases are performed, compared and discussed. The $^{17}O$ MAS NMR spectrum for the third amorphous phase, clearly excludes some of the hypotheses reported previously in the literature.

Variable temperature NMR experiments on the ambient pressure phase are also presented showing a significant variation in chemical shift for one of the oxygen sites as the temperature decreases. DFT calculations on model structures generated from total neutron scattering data are shown to reproduce the $^{17}O$ NMR thermal behaviour confirming the proposed mechanism responsible for the negative thermal expansion in this compound.

**Chapter 5** is dedicated to studies on tungsten trioxide, and previous literature on temperature dependent phase transitions in this compound is reviewed. The synthesis of the $^{17}O$ labelled $WO_3$ is detailed and the effect of different synthetic procedures on the pathway of the phase transitions are highlighted. Correlation between subtle structural changes and $^{17}O$ NMR parameters are described using structures reported in the literature and CASTEP calculations. A linear correlation was shown between the O-W distances around a given oxygen and the isotropic chemical shift, as well as the quadrupolar coupling constant. Discontinuities in these linear correlations were observed for $WO_3$ phases separated by a first order phase transition.

Although these simple correlations are true for disparate ranges of W-O bond distances, they appear to be more complex when looking at oxygens with more similar local environments.

## Contents

# Chapter 1. Introduction to characterisation techniques

## 1.1. NMR in solids

### 1.1.1. General overview

NMR spectroscopy observes the interaction of the constituent nuclear spins of a sample with an external magnetic field. The intrinsic composition of a given type of nucleus (number of unpaired neutrons and protons) determine its spin quantum number $I$. For a given nucleus, $I$ can adopt either integer or half integer values, and is associated with $2I+1$ states. These are degenerate (have the same energy) in the absence of an external magnetic field. When placed into a magnetic field, the degeneracy of these energy levels is removed and $2I+1$ distinct energy levels arise distinguished by the $m_I$ magnetic quantum number ($m_I$=-$I$, -$I$+1,…$I$-1,$I$) (see Figure 1-1). The energy of these levels in a magnetic field $B_0$ is:

$$E(m_I) = -\hbar m_I \gamma B_0$$

Where the gyromagnetic ratio, $\gamma$, is a fundamental property of a given isotope and $\hbar$ is the reduced Planck's constant.

This splitting of the energy levels when a magnetic field is applied is called the Zeeman effect. The energy difference between two consecutive levels is :

$$\Delta E = \hbar \gamma B_0 = h\nu_{NMR}$$

Hence the NMR frequency $\nu_{NMR}$ is:

$$\nu_{NMR} = \frac{\gamma B_0}{2\pi}$$

If we consider two consecutive energy levels, $E_1$ and $E_2$ ($E_1$<$E_2$), at equilibrium, their corresponding $n_1$ and $n_2$ populations for a $N$ spins system follows a Boltzmann distribution:

$$n_i = \frac{1}{2} N \exp(-E_i / k_B T) \quad (i=1, 2)$$

Where $k_B$ is the Boltzman constant.

Hence

$$\frac{n_1}{n_2} = \exp\left(\frac{-\Delta E}{k_B T}\right)$$

In an NMR experiment, the transition between two successive energy levels is created by perturbing the system using a magnetic radiation ($B_1$). At the NMR frequency, the Boltzman equilibrium of the spin population existing between the different energy levels is modified. The NMR response is measured as the spins are going back to their equilibrium distributions. The difference in populations between these successive energy levels is very small since $\Delta E << k_B T$. This makes NMR a very low sensitivity technique.

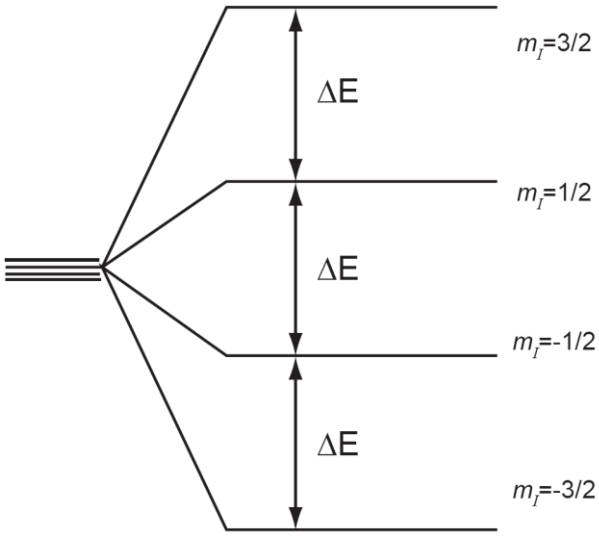


**Figure 1-1 Influence of an external magnetic field $B_0$ on a $I$=3/2 nucleus (Zeeman effect).**

When considering only the Zeeman interaction, an NMR signal will therefore depend on the strength of external magnetic field $B_0$ and the gyromagnetic ratio of the observed isotope. However, several other interactions can affect the energy levels and render NMR very sensitive to small local changes.

### 1.1.2. Tensorial representation of the magnetic interactions

All the magnetic interactions experienced by an atom (shielding, J-coupling, dipolar and quadrupolar couplings) are anisotropic as they depend on their orientation with respect to $B_0$. In the general case, a given interaction $T$ can be described as a second order tensor. In the laboratory frame, the tensor is represented by a 3x3x3 matrix.

$$T_{lab} = \begin{bmatrix} T_{xx} & T_{xy} & T_{xz} \\ T_{yx} & T_{yy} & T_{yz} \\ T_{zx} & T_{zy} & T_{zz} \end{bmatrix}$$

Where $x$, $y$ and $z$ refer to the laboratory axes.

By diagonalising this matrix, the interaction can be described in its own axis system called the Principal Axis System (PAS) of the interaction. A new matrix is obtained:

$$T_{PAS} = \begin{bmatrix} T_{11} & 0 & 0 \\ 0 & T_{22} & 0 \\ 0 & 0 & T_{33} \end{bmatrix}$$

This axis system is shown in Figure 1-2.

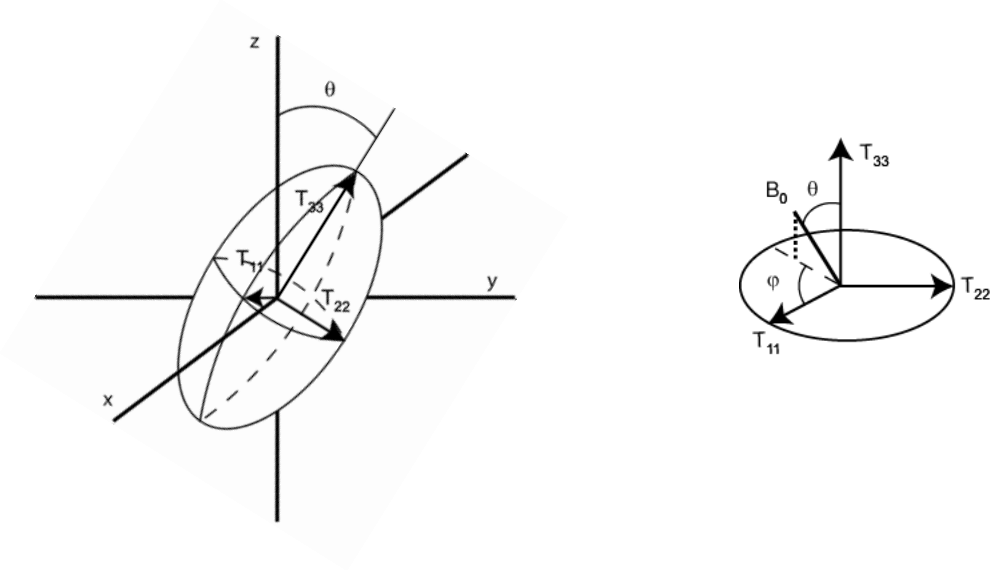


**Figure 1-2 Tensorial representation of an interaction.**

Some of the useful quantities used in NMR analysis can be extracted from this tensor amongst which, the isotropic contribution $T_{iso}$ is given by:

$$T_{iso} = \frac{1}{3}\left(T_{11} + T_{22} + T_{33}\right)$$

The anisotropy of the interaction $\delta_T$ is described:

$$\delta_T = T_{33} - T_{iso}$$

For a spherical tensor ($T_{11}$=$T_{22}$=$T_{33}$=$T_{iso}$) the tensor is therefore isotropic and $\delta_T$ = 0.

The deviation from an axial symmetry ($T_{11}$=$T_{22}$) is referred to as the asymmetry of the interaction and given by:

$$\eta_T = \frac{T_{22} - T_{11}}{\delta_T}$$

All the NMR interactions can be described as a sum of an isotropic and an anisotropic contribution. For interactions relatively small compared to the Zeeman interaction, this sum is expressed as follows:

$$T_{iso} + T_{aniso} = T_{iso} + \delta_T \left[ P_2\left(\cos\theta\right) - \frac{\eta_T}{2}\sin^2\theta_T \cos^2\varphi_T \right]$$

Where $P_2(\cos\theta) = \frac{\left(3\cos^2\theta - 1\right)}{2}$ is the second order Legendre polynomial and $\theta_T$ and $\varphi_T$ are the angles describing the orientation of the tensor as shown in Figure 1-2.

In the following, we use this tensorial model to describe the different magnetic interactions encountered in NMR. If the strength of the interaction is significantly large relative to the Zeeman interaction, the perturbation experienced by the system has to be considered to a larger rank order. This is often the case for quadrupolar coupling and will be described in section 1.1.6.

### 1.1.3. Chemical shifts

If we consider an atom within a sample, the magnetic field experienced by this atom will be slightly different depending on its electronic environment. In the presence of the external magnetic field $B_0$, the circulation of the electrons around a given nucleus creates a small local magnetic field, *B'*, in the opposite direction to $B_0$ and the field effectively interacting with a nucleus $i$ ($B_{eff}$) can therefore be written:

$$B_{eff} = B_0 - B' = B_0(1-\sigma_i)$$

Where $\sigma_i$ is the chemical shielding and depends on the local electronic structure around the nucleus $i$. Therefore, when $B_{eff}$ is experienced by the nucleus, the difference between two successive energy levels becomes:

$$\Delta E = \hbar\gamma B_0(1-\sigma_i) = h\nu_{NMR}$$

In a tensorial representation, the chemical shielding interaction $\sigma_i$ can be expressed for a given atom by both an isotropic (dependent on its local environment) and anisotropic (dependent on the orientation relative to the magnetic field $B_0$) part. The effect of the anisotropy and the asymmetry on a powdered sample (distribution of orientations relative to $B_0$), on the distribution of chemical shieldings are shown in Figure 1-3. The chemical shift anisotropy (CSA) therefore represents the range of frequencies covered by this distribution and is typically of several kHz.

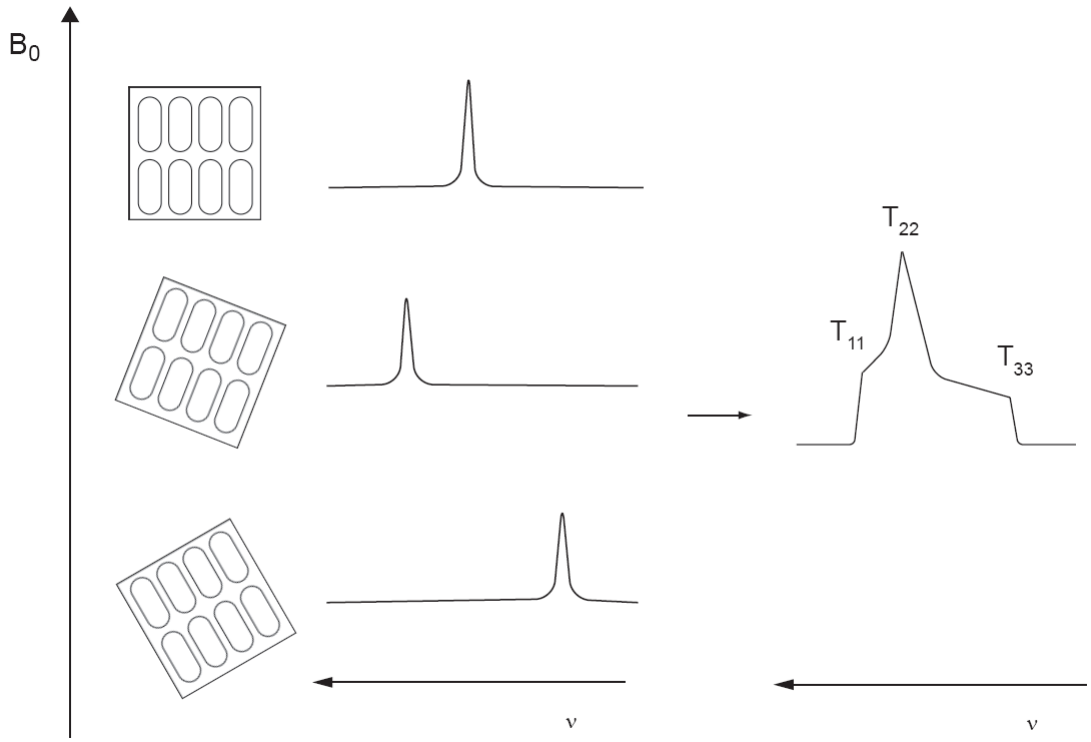


**Figure 1-3 Influence of the orientations of the crystallites on the chemical shift in a powdered sample.**

The NMR frequency observed for a given nucleus, $\nu_{NMR}$, is therefore a function of its chemical shielding and $B_0$. For different $B_0$ magnetic field strengths (different instruments or field strength decay over time), the NMR frequency observed for a same spin varies. In practice, the NMR frequency has therefore to be expressed relative to the frequency of a spin in a reference compound ($\nu_{ref}$). The difference between the two frequency values is called the chemical shift defined as $\delta_i = \nu_{ref} - \nu_i$ and can be directly related to the chemical shielding differences.

### 1.1.4. Scalar coupling

The environment of a given nucleus can also be perturbed by magnetic fields arising from surrounding nuclei. A surrounding atom X with a non-zero spin number $(I)$ possesses $2I$+1 possible orientations for this local magnetic field but for demonstration we will just look here at the interaction between two ½ spins, $S$ and $I$. Spin $I$ can experience the influence of the magnetic moment of spin S through bonding electrons (whose sign depends on m and which is typically of few tens of Hz). This additional magnetic field is much smaller than the external magnetic field $B_0$ but will influence the splitting of the energy levels as shown in Figure 1-4. Similarly, $S$ will experience the influence of the magnetic moment of $I$. Such an interaction is referred as through–bond spin-spin coupling (or J-coupling). The resulting energy levels are expressed as:

$$E = -m_I \nu_I - m_S \nu_S + J_{IS} m_I m_S$$

Where $m_I$ and $m_S$ are the magnetic quantum numbers for $I$ and $S$ respectively and $J_{IS}$ is the scalar coupling constant.

For a two ½ spins system, $m_I$ and $m_S$ can both adopt ½ (spin $\alpha$) and -½ (spin $\beta$) values and therefore their energy levels are expressed as in Table 1-1.

**Table 1-1 Expression of the energy level for a two ½ spins system placed in an external magnetic field $B_0$. With (right column) and without (left column) the presence of J-coupling interaction**

| IS spin states | Energy levels of a two spin (I and S) system in a presence of $B_o$ | Energy levels in a J-coupled system |
|---|---|---|
| $\beta\beta$ | $+1/2\upsilon_I+1/2\upsilon_S$ | $1/2\upsilon_I+1/2\upsilon_S+1/4J_{IS}$ |
| $\beta\alpha$ | $+1/2\upsilon_I-1/2\upsilon_S$ | $1/2\upsilon_I-1/2\upsilon_S-1/4J_{IS}$ |
| $\alpha\beta$ | $-1/2\upsilon_I+1/2\upsilon_S$ | $-1/2\upsilon_I+1/2\upsilon_S-1/4J_{IS}$ |
| $\alpha\alpha$ | $-1/2\upsilon_I-1/2\upsilon_S$ | $-1/2\upsilon_I-1/2\upsilon_S+1/4J_{IS}$ |

The coupling results in the appearance of two pairs of resonances separated by $J_{IS}$ around the $I$ and S frequencies in the experimental spectra (Figure 1-4).

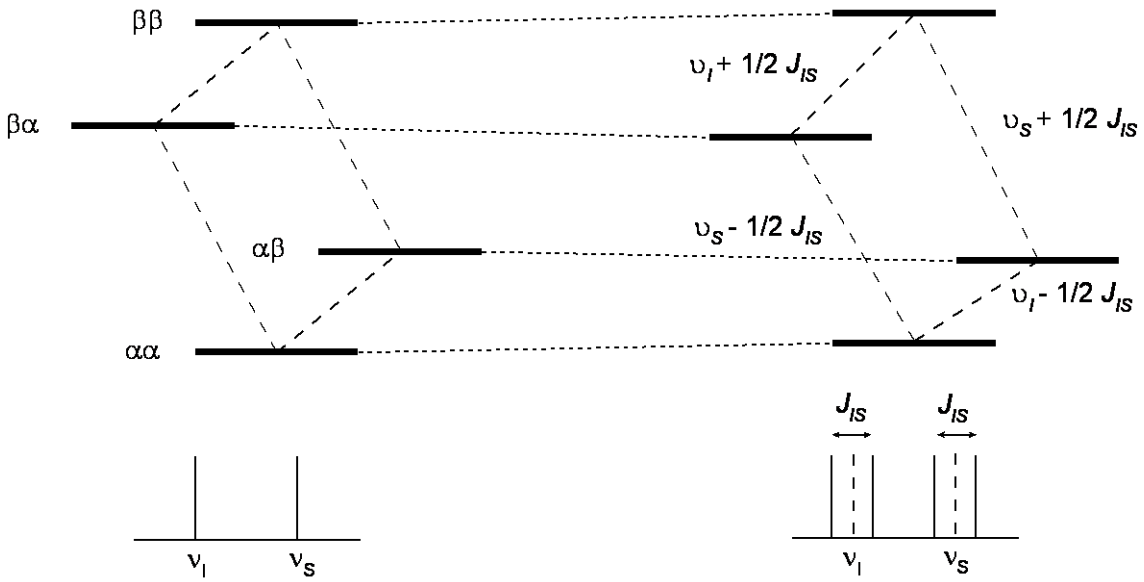


**Figure 1-4 Influence of the through-bond interaction between two spins 1/2 ($I$ and $S$) on the energy levels.**

In solids, observation of such a weak splitting interaction is normally unobservable due to the broad linewidth and measurement of this interaction is usually done through indirect methods (see spin-echo, section 1.2.1).

### 1.1.5. Dipolar coupling

Coupling between two spins can also occur through direct spatial coupling. A non-zero spin nucleus can be pictured as a small dipole with a magnetic moment. The dipolar coupling depends on the orientation of the spin relative to $B_0$. The dipolar interaction is completely anisotropic but has an axial symmetry ($\eta_D$=0). If we consider two spins $I$ and $S$ separated by a distance $r$ placed in an external magnetic field, the dipolar coupling between them can be expressed as follows:

$$D_{IS} = -\frac{\mu_0}{2\pi}\frac{\hbar\gamma_I\gamma_S}{r_{IS}^3}\left(P_2(\cos\theta)\right) = \delta_D\left(P_2(\cos\theta)\right)$$

Where $\delta_D$ is the dipolar coupling constant.

This phenomenon leads to one dipolar coupling effect for each orientation of the molecules in a sample and results in broad signals in the NMR spectrum reflecting this anisotropy.

### 1.1.6. Quadrupolar coupling

Up to this point, scalar and dipolar coupling have been discussed for spin ½ nuclei. However, about 75% of the nuclei in the periodic table have a spin number $I$ >1/2. Those nuclei are called quadrupolar and their nuclear magnetic properties are influenced by the interaction of the electric field gradients around the nuclei (EFG) and the nuclear quadrupolar moment. Unlike other magnetic interactions, the quadrupolar interaction amplitude can reach very high values (up to several tens of MHz). Since this

interaction is large relative to the Zeeman interaction, its effects have to be calculated to first and second order.

Figure 1-5 shows the corrections to the Zeeman energy levels induced by first and second order quadrupolar interaction. The first order correction to the Zeeman energy levels is expressed by:

$$\nu_Q^{(1)}(m_I) = -\frac{3(2m_I - 1)}{8I(2I-1)} \times C_Q \left[ P_2(\cos\theta) + \eta_Q \sin^2\theta \cos^2\varphi \right]$$

In order to avoid unnecessarily complex description, the second order perturbation will be described for an axially-symmetrical case ($\eta_Q$=0) here as :

$$\nu_Q^{(2)}(m_I) = -\frac{{C_Q}^2}{\nu_0} f(I) \times \left[ \frac{3}{10} + \frac{6}{7} P_2(\cos\theta) - \frac{81}{70} P_4(\cos\theta) \right]$$

Where $P_4(\cos\theta) = \dfrac{\left(35\cos^4\theta - 30\cos^2\theta + 3\right)}{8}$ is the second order Legendre polynomial and $C_Q$ is the quadrupole coupling constant.

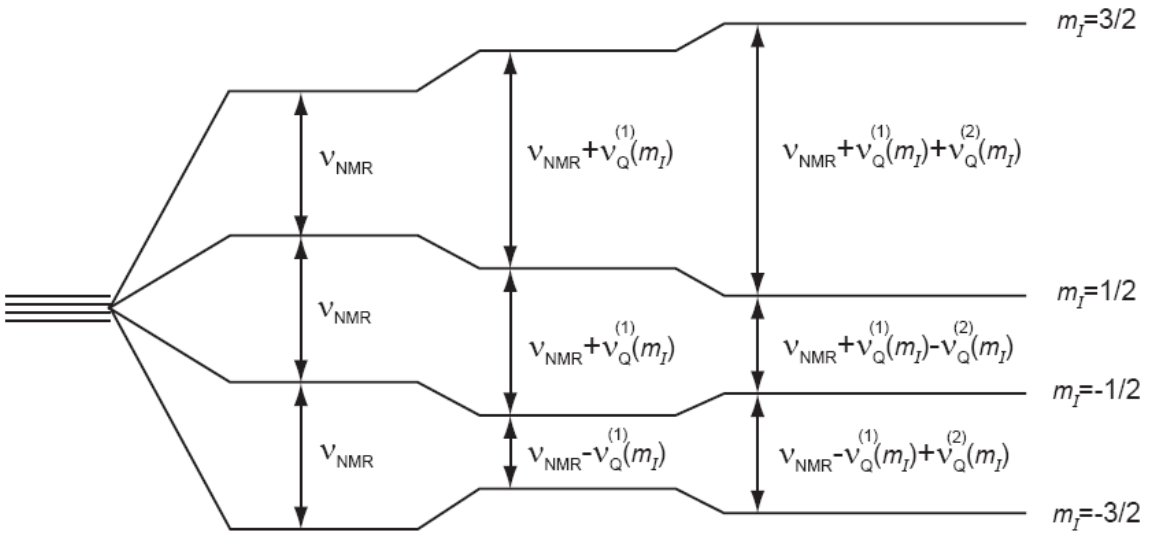


**Figure 1-5 Influence of the first and second order quadrupolar interaction on the energy levels of a *I*=3/2 nucleus.**

Both equations contain an isotropic and an anisotropic component and the second order term is influenced by two angular dependent terms. The double dependence makes quadrupolar nuclei more difficult to study (see below) but can also be used to bring additional information about the surrounding symmetry or chemical environment (thanks to the quadrupolar parameters $\eta_Q$ and $C_Q$).

### 1.1.7. Magic angle spinning in solids

In liquid systems, the fast random tumbling of the molecules cancels out the chemical shift distribution mentioned in section 1.1.3, resulting in a single sharp resonance in the NMR spectrum at the average (isotropic) value of the chemical shifts. However in solids, the fixed orientation of the crystallites relative to $B_0$ leads to broad signals which are a sum of all individual crystallite resonances. In order to simulate the motion phenomenon that occurs in liquid, averaging can be made using the rotation of the sample at high spinning speeds. This rotation then leads to a time (related to the rotor spinning speed) and an orientation (related to the angle between the sample and the magnetic field) dependence for the interactions. If the sample spinning frequency is higher than the anisotropy of the interaction, then the time dependent anisotropic part is averaged and becomes negligible and only the spatially dependent term remains. The space dependent remaining part of the anisotropy is dependant for all the interactions mentioned above on the same polynomial $P_2(\cos\theta) = \frac{\left(3\cos^2\theta - 1\right)}{2}$, that is zero for a $\theta$ value of $\theta$ = 54.73°, the so called “Magic Angle”.

The anisotropic parts of the chemical shift (up to hundreds of kHz), J-coupling (typically of few tens of Hz) and dipolar (several kHz) interactions can be removed by Magic Angle Spinning (MAS) if smaller or comparable to the spinning speed. When the spinning frequency is smaller than the anisotropy of the interaction, broadenings and splitting described above persist in the experimental spectra.

In the case of the chemical shift interaction, for a spinning frequency less than the chemical shift anisotropy, the isotropic line presents on both sides sidebands spaced by the spinning frequency[(1)]**.** These sidebands are called the spinning sidebands and their intensities depend on the symmetry on the chemical shift anisotropy. Therefore extracting the intensities of these sidebands can be related to the orientation of the shielding parameters[(2)]. However, in the case of overlapping resonances, this measurement becomes impossible. For most of the work here we have ignored spinning sidebands and focus on the centerbands only.

Residual dipolar coupling can also be observed and broadens the NMR spectra. This broadening can be reduced or removed by rotating the sample at higher spinning rates or by employing lower $B_0$ fields.

Under magic angle spinning, the anisotropic part of the quadrupolar interaction at first order is removed while part of the second order anisotropy (the $P_4$ ($\cos\theta$) dependent part) remains. The remaining anisotropy leads to a broadening of the NMR signal and nuclei with a large quadrupolar interaction are sometimes unobservable. Several techniques have been developed to remove this second order perturbation but will not be discussed here.

## 1.2. Probes of through-bond interactions

### 1.2.1. Spin-echo experiment

The spin-echo sequence is usually used to remove inhomogeneous effects responsible for the broadening of an NMR signal. Homogeneous broadening is due to the fast transverse relaxation of a spin to its equilibrium position and depends only on its environment. However, external inhomogeneous contributions (such as external field inhomogeneities or chemical shift distributions) can generate different Larmor frequencies for equivalent spins within the sample. This leads to an extra broadening of the signal. The spin echo experiment removes these inhomogeneous effects and is therefore used to determine the transversal relaxation rate of a spin. As we show here, the spin-echo sequence can also be used to determine J-coupling values.

The pulse sequence of the spin echo experiment is shown in Figure 1-6. The first 90° pulse flips the magnetization to the xy plane. This evolves over a $\tau$ period before being refocused along the y axis by a 180° pulse. It then evolves over a second period of length $\tau$ before acquiring the signal. The intensity of the NMR signal at the end of the 2τ period is:

$$I(2\tau) = I(0)\exp\left(\frac{-2\tau}{T_2^{'}}\right)$$

Where $T'_2$ is the transverse relaxation time.

Under fast MAS and for spin ½ nucleus, the magnetisation is not influenced by dipolar (if completely removed by the fast rotation) or quadrupolar coupling. However, if a homonuclear J-coupling exists between two nuclei, the spin-echo signal is modulated by J-coupling over the $2\tau$ period. The intensity of the NMR signal at after $2\tau$ becomes :

$$I(2\tau) = I(0)\times\cos(2\pi J\tau)\times\exp\left(\frac{-2\tau}{T_2^{'}}\right)$$

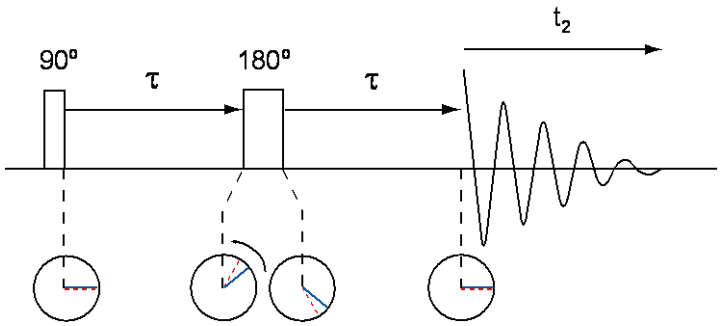


**Figure 1-6 Pulse sequence scheme for the spin–echo sequence.**

By acquiring experiments with different evolution delay τ, the evolution of the intensity of the signal can be fitted in order to extract both the $T'_2$ constant and the J-coupling interaction strength.

### 1.2.2. Pre-saturated refocused INADEQUATE parameters optimisation

Double quantum experiments to probe homonuclear connectivities between spin 1/2 nuclei were first introduced in the liquid state by Bax et *al.*[3]. The INADEQUATE experiment was implemented for $^{13}C$ in the solid state by Lesage et *al.*[4] and its presaturated version is presented in Figure 1-7. In pyrophosphates, studied in our work, the $^{31}P$ chemical shift anisotropy can be large and therefore not completely removed by MAS[5, 6]. To prevent the apparition of spinning sidebands in the ω1 dimension, several experimental parameters (spectral width, t1 time increment) have to be synchronised with the rotor period.

For samples with long longitudinal relaxation times ($T_1$) (again such as in the ones studied in this thesis), the acquisition time of a 2D spectrum can be significant. A common procedure to reduce this acquisition time is to employ a presaturation sequence and decrease the time between two successive experiments. The presaturation parameters (number of acquisition pulses, delay between 90° pulses) have to be optimised to obtain reproducible results. The number of presaturation pulses can be optimised but the delay between 90° pulses has to be longer that the $T'_2$ determined by spin-echo experiment.

Better sensitivity would be achieved using a single quantum (SQ) pulse sequence[7] but the use of double quantum filter in the INADEQUATE sequence results in a clearer 2D spectra. Indeed, by removing the SQ interactions, diagonal autocorrelation peaks can be removed and couplings between spins of small chemical shift differences are distinguished.

In order to get the maximum signal converted into the double quantum coherence, the intensity of the first row has to be optimised. After refocusing the magnetisation using a spin-echo sequence (see above), a double quantum (DQ) coherence is created by applying a second 90° pulse and it evolves at the double quantum frequency (the sum of the frequencies of the two coupled sites) over a $t_1$ period. The signal is then converted back to an observable signal by applying a second spin-echo pulse block.

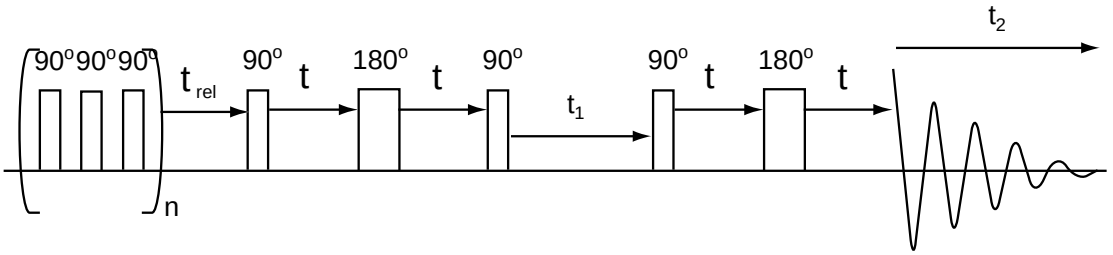


**Figure 1-7 Presaturated refocused INADEQUATE pulse sequence.**

The 2D spectra from this sequence has been shown to be very successful for samples with a reasonable number of $^{31}P$ sites[8, 9]. The dipolar coupling and the chemical shift anisotropy are, in most

cases, removed by fast magic angle spinning but can remain and lead to some artefacts in the 2D spectra.

### 1.2.3. Interpretation of INADEQUATE spectra

The quantum mechanical description of the evolution of the spin system has been developed in reference 10 and summarises the conditions over which correlation peaks occur during an INADEQUATE experiment. For spins with distinct chemical shifts, $\nu_1$ and $\nu_2$, the magnetisation evolves under J-coupling and relaxation over the $2\tau$ period and cross peaks appear across the diagonal of the spectra at a frequency of $\nu_1^{iso} + \nu_2^{iso}$ in the t1 (2Q or DQ) dimension.

Spins are totally magnetically equivalent when their chemical shifts and chemical shift anisotropies are identical. Structurally, this is observed for spins related by a centre of inversion. For two equivalent spins, no correlation peak is observed on the INADEQUATE diagonal. However, two spins with identical chemical shifts can have different chemical shift anisotropy tensors. In this case even in the absence of J-coupling, a diagonal peak can also be observed if the chemical shift anisotropy strength and the dipolar coupling between the spins is larger than the spinning speed. This is due to $n$=0 rotational resonance effect[10] ($\nu_1^{iso} - \nu_2^{iso} = n\nu_r = 0$). Under these conditions, the dipolar coupling between the two sites can be reintroduced and lead to cross peaks even in the absence of J-coupling. The intensities of the peaks arising from this effect decreases when the strength of the $B_0$ magnetic field and the spinning speed are increased.

Figure 1-8 presents an example of a $^{31}$P 2D MAS INADEQUATE spectrum of $TiP_2O_7$ recorded with a spinning speed of at 12 kHz in a 400 MHz magnet. This structure contains six $P_2O_7$ groups with one of them formed by two magnetically equivalent phosphorus (related by a centre of inversion)[11]. Following the explanations given above, five cross peaks should be observed across the diagonal and the sixth one shouldn't be observed. Figure 1-8 indeed shows five pairs of cross peaks across the diagonal. However, we can as well observed four peaks lying along the diagonal. These peaks are due to the rotational resonance effect described above and their intensity has been shown to decrease significantly at higher fields and higher spinning speeds.

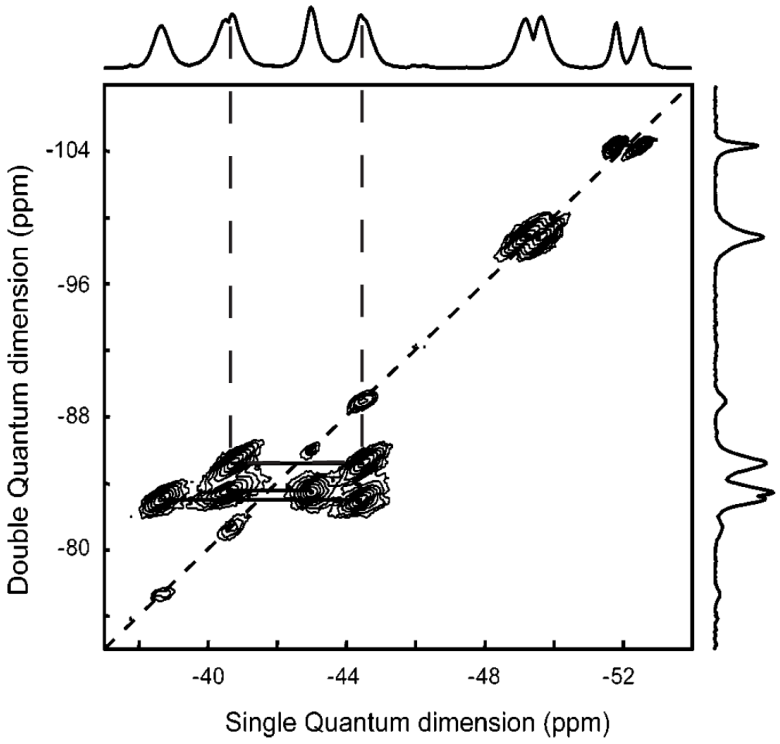


**Figure 1-8 2D INADEQUATE experiment of $TiP_2O_7$ at 12 kHz. The figure was adapted from reference [12]. The top spectrum shows the 1D projection of the NMR resonances in $TiP_2O_7$. The right hand spectra is a projection of the cross peaks. The dotted lines show the connectivities between two sites interacting through J-coupling, and represent a single P-O-P linkage.**

This rotational resonance effect (due to a strong dipolar coupling between two spins) can also have other effects on an NMR spectrum: shorter $T_1$[13, 14], effect on the lineshapes (splitting) or exchange of Zeeman order.

## 1.3. Dipolar coupling driven experiments

As mentioned in section 1.1.5, dipolar coupling is dependent on the orientation of the spins relative to the magnetic field. Therefore, it cannot directly be observed in the liquid state as fast motion of molecule cancels out its effect. In a solid-state MAS NMR experiment, fast rotation of the sample also leads to a reduction or the total cancellation of the anisotropic contribution of this interaction. Therefore, “recoupling” procedures have to be used to restore the through-space dipole-dipole couplings and therefore probe spatial interactions.

### 1.3.1. SQ-DQ POST-C7 experiment

In this thesis, the SQ-DQ POST-C7[15] sequence was used to observe these spatial interactions. The corresponding pulse sequence is shown in Figure 1-9. As in the INADEQUATE experiment, this pulse sequence uses the passage through a double quantum coherence (DQ) to obtained simplified spectra and is therefore advantageous to use for complex structures. The POST-C7[16] block in this pulse sequence reintroduces the dipolar coupling interaction removed by MAS. During the $t_1$ period the magnetisation therefore evolves at the double quantum frequency before being reconverted into

observable coherence by a second identical POST-C7 block. Nuclei with similar dipolar coupling will then be seen on the same projection on the 2Q dimension.

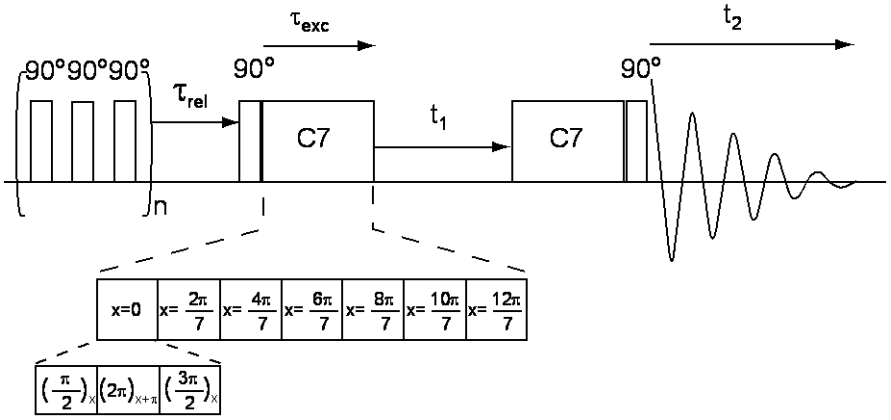


**Figure 1-9 Pulse scheme for 2D experiment using a POST-C7 for recoupling dipolar interaction in a rotating solid.**

The time length of this C7 block determines the contact time under which the dipolar coupling is converted into the double quantum coherence. For shorter $\tau_{exc}$, only nuclei interacting with stronger dipolar coupling will recouple. By varying the length of $\tau_{exc}$, different dipolar interaction strengths can be probed.

### 1.3.2. Interpretation of 2D POST-C7 spectra

In the INADEQUATE experiment, connectivities between coupled spins are probed. However, no information on the strength on the coupling can be extracted. In the POST-C7 experiment however, the variation of the exchange time ($\tau_{exc}$) can give information on the strength of the spatial interaction between two spins. 2D spectra using two different $\tau_{exc}$ times are shown in Figure 1-10.

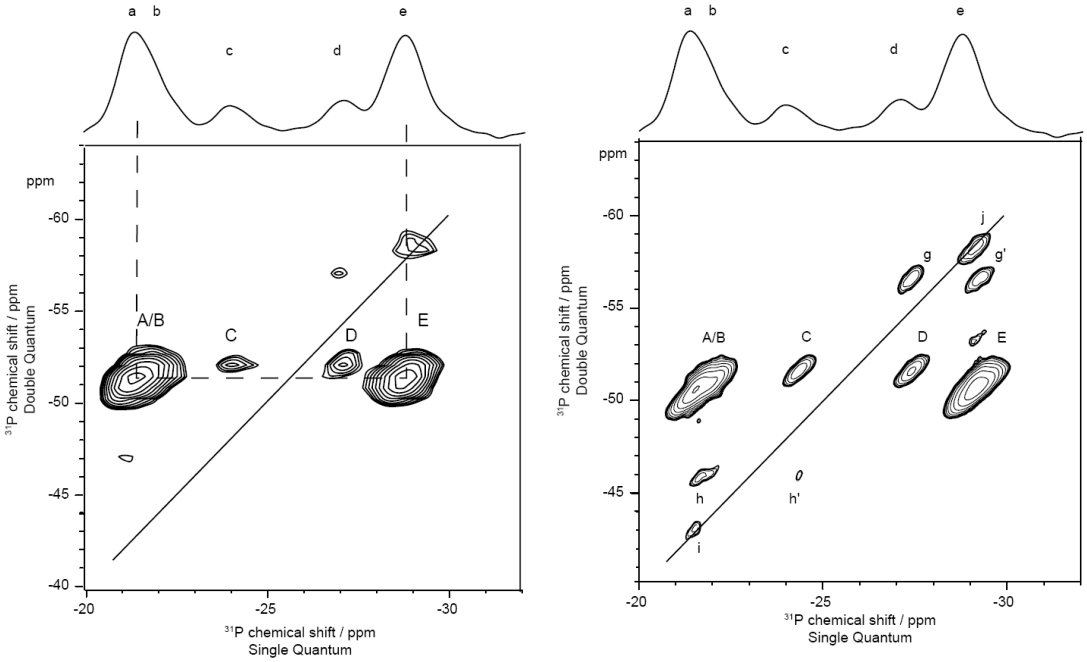


**Figure 1-10 2D POST-C7 experiment with a mixing time of 0.143 ms and 0.358 ms extracted from Chapter 3.**

We can read these spectra by looking at the peaks arising across the diagonal. As for the INADEQUATE described above, a pair of peaks across this diagonal shows that the two corresponding $^{31}$P sites interact via dipolar coupling. The strength of the dipolar coupling between two spins decreases as the spins get further apart. The two spectra in Figure 1-10 show this effect as for longer mixing times, more correlations peaks are observed. The peaks arising at short mixing times correspond to spins interacting through large dipolar couplings. The intensity of the different cross pairs as a function of a mixing time has been used with different dipolar experiments to assign the NMR resonances in compounds of known crystal structures[(17)]. However, in this 2Q experiment, the poor signal to noise ratio obtained at low $\tau_{exc}$ and the lack of resolution between resonances limit somehow such analysis.

## 1.4. CASTEP software for calculating NMR parameters

From the discussion in section 1.1, the nuclear magnetic response of a given spin could in principle be calculated by determining the difference in energy levels while considering all the external interaction and coupling described above. Using the Born-Oppenheimer approximation (the atomic positions are fixed when compared to the fast motion of electrons), the nuclear kinetic energy is neglected. The Schrödinger equation describing the electronic structure of a system can be written as a linear combination of monoelectronic atomic orbitals $\psi_i$ as follows:

$$H\psi_i = \left( -\sum_i \frac{\hbar^2}{2m_e} \nabla_i^{\,2} + V_{ext} + V_{eff} \right) \psi_i = E\psi_i$$

Where the first term corresponds to the kinetic energy of the electrons and nuclei, $V_{e\text{xt}}$ is the external potential of the nuclei and $V_{eff}$ the effective potential and describes the potential between an electron and all others electrons in the system (Hartree potential). In the Hartree-Fock approach, the exchange between the electrons (two electrons cannot simultaneously be found at identical position) is treated exactly but the correlation (representing the probability of presence of an electron considering its distances to the other electrons) is neglected. The approximated Hartree-Fock energy is expressed:

$$E_{HF} = \left( -\sum_i \frac{\hbar^2}{2m_e} \nabla_i^{\,2} + V_{ext} + \sum_i \sum_{j>i} \frac{e^2}{4\pi\varepsilon_0 r_{ij}} \right)$$

Solving the Hartree-Fock Schrödinger equation for N electrons therefore corresponds to determining N-one electron wavefunctions and therefore lead to a 3N parameters problem (each electronic position being described in a 3D space).

The precision of the Hartree-Fock calculations depends mainly on the level of accuracy with which the monoelectronic wavefunctions are described. An infinitely large basis set of wavefunctions would lead to the exact $E_{HF}$ value. Though this method is giving reasonably accurate results in a reasonable calculation time for some systems, there is few limitations of importance that have to be considered. First, Hartree Fock method is based on approximation and overestimate the correlation interaction between electrons and the real energy of the system can never be reached. Secondly, the complexity for computing such calculations increases with the number of electrons and wave functions involved. Therefore, accurate computations on large systems or systems containing heavy atoms can become extremely challenging.

In the density functional theory (DFT) approach however, the total energy of the system is no longer expressed by a sum of N monoelectronic functions (3N degrees of freedom) but as a function of a 3 dimensional electron density object, $\rho(r)$, that is defined for any position in the crystal (3 degrees of freedom):

$$E\left[\rho(r)\right] = \int dr V_{ext}(r)\rho(r) + F\left[\rho(r)\right]$$

Where $F\left[\rho(r)\right] = E_K\left[\rho(r)\right] + E_H\left[\rho(r)\right] + E_{XC}\left[\rho(r)\right]$ describing the electron kinetic energy ($E_K\left[\rho(r)\right]$), the Hartree Coulomb term ($E_H\left[\rho(r)\right]$) and the exchange-correlation functional($E_{XC}\left[\rho(r)\right]$). Reducing the 3N parameters Hartree-Fock problem to a three dimensional problem (DFT) problem leads to a huge reduction of the computational cost required. Written as such the energy is described exactly but in practice, the main approximation in DFT calculations arises from approximating $E_{XC}$ functional. Different approximations can be used (i.e LDA, GGA) to described $E_{XC}$ and contribute largely to the accuracy of the calculations.

CASTEP is a computer code using Density Functional Theory (DFT) to predict physical properties in materials. In the presence of a magnetic field, the Hamiltonian of the system is modified. The chemical shift anisotropy (CSA) and electric field gradient tensors (EFG) can be calculated. To make the calculations as efficient as possible, a few manipulations can be made to describe the density functional. The wavefunction is represented by a planewave basis set. To simplify the representation of this wavefunction, CASTEP uses pseudo-potentials to describe the electrons in the core regions of the atoms and plane waves are used to describe the valence electrons. This description is referred in the literature as the GIPAW method. An infinite basis set and an exact description of the $E_{XC}$ functional can in principal lead to the exact energy of the system. However, in practice, both the $E_{XC}$ functional and the wavefunction are approximated.

In CASTEP, the size of the planewave basis set (and therefore the accuracy of the wavefunction description) is determined by the cutoff energy. The accuracy of the calculations also depends on the sampling of the structure. This is done via the k-point spacing or k-point grid. The quality of this sampling is described by the number of k-point.

As the energy of the system depends on the wavefunction, an appropriate set of planewaves has to be found to determine the lowest energy of the system. This is achieved in DFT using self-consistent field method (SCF).

In a geometry optimisation process, the same SCF process occurs but the energy is calculated for different sets of atomic positions (respecting symmetry and user defined constraints). When the lower energy is reached, the corresponding set of coordinates leads to the optimised structure.

## 1.5. Optimisation of the parameters for CASTEP calculations.

In this thesis, we will present results from DFT NMR calculations on three different systems: $^{17}O$ calculations on $WO_3$ and $ZrW_2O_8$ and $^{31}P$ NMR on $(MoO_2)_2P_2O_7$. In order to perform accurate ab-initio calculations, it is essential to optimise consistently certain parameters associated with the calculations. As described in Chapter 1, the choice of an infinite basis set will lead to an exact solution of the energy of the system. However, due to the limitation of computer power as well as the available computing time, the size of the basis set has to be chosen in order to lead to accurate results in a reasonable amount of time. The determination of the right basis set size is performed in the GIPAW method by optimising the cutoff energy parameter ($E_{cut}$) fixing the number of planewaves per unit volume. When the cutoff energy is varied from a small to a large value the energy of the atomic energies of the system decreases until reaching an asymptote. The optimum cutoff energy value is strongly dependent on the core radius of the smallest element in the structure (in our examples O) and the oxygen atomic energy is therefore used to determine the optimal cutoff energy.
The accuracy of the structure sampling also has to be set. This is done via the k-point spacing or k-point grid.

To ensure the suitabilty of the optimisation of those two parameters, optimisation calculations should ideally be done on the compound studied. In the case of very large and time consuming calculations, optimisations on smaller systems are usually appropriate if these are for electronically similar materials. In the case of both $WO_3$ and $ZrW_2O_8$, we therefore performed the optimisations directly on the considered system, each of the optimisation step requiring relatively short calculation times (details given below). For calculations on $(MoO_2)_2P_2O_7$ however, optimisations can easily be made on the simpler high temperature structure (60 atoms per unit cell) whereas calculations on the larger model superstructures (240 atoms respectively) would require large amount of time on supercomputing facilities. For those later structures, the parameters used in our calculations are taken from the high temperature form.

In order to perform accurate DFT calculations, we first optimised the values of the cutoff energy for the three structures studied. The plots shown in Figure 1-12 show the evolution of the calculated energy for the different constituent atoms of our structures for a k-point spacing of 0.2.

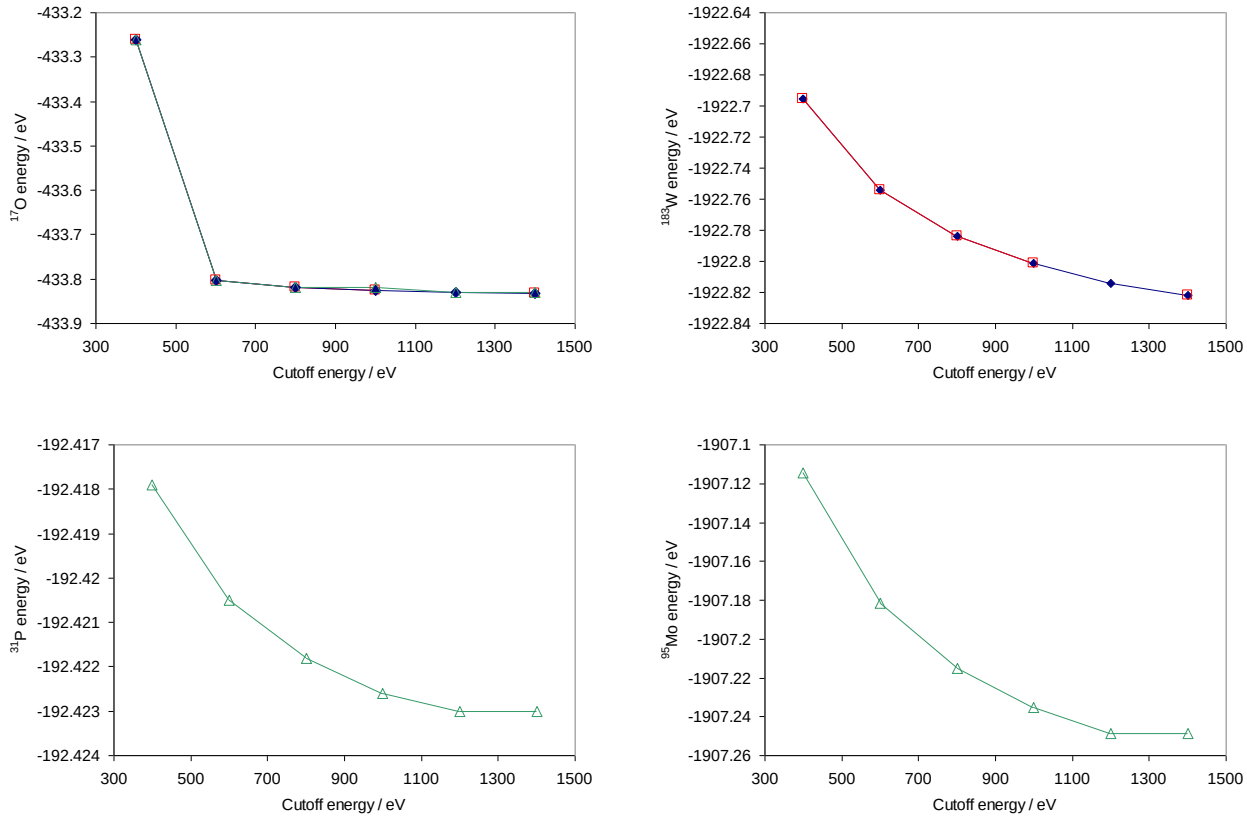


**Figure 1-11 Evolution of the atomic energies as a function of the cutoff energy for $WO_3$ (red squares), $ZrW_2O_8$ (blue diamonds) and $(MoO_2)_2P_2O_7$(green triangles) using a k-point spacing of 0.2.**

These plots show that excellent accuracy for $^{17}O$ parameters calculations can be obtained for cutoff energies of 500 eV. Similarly, the $^{31}P$ energies converge at relatively low cutoff energies values and

the choice of 900 eV to study this nucleus should be sufficient. However, for heavier atoms ($^{91}$Zr and $^{183}$W), convergence is reached only for much higher cutoff energy values.

Therefore, if one was only interested in looking at $^{17}$O or $^{31}$P NMR properties (as we present in this work) a cutoff energy of 900 eV appears to be sufficient. However, we chose a cutoff energy of 1200 eV to ensure that the energies of all the atoms involved converged properly. By choosing such a high energy cutoff, the times of our calculation was increased, however, the results from our calculations were and will potentially be used for further NMR studies on $^{91}$Zr and $^{183}$W in these compounds.

The accuracy of the calculations also depends on how precisely the structure is sampled. This is determined by the number of k-points and the accuracy of the calculations increases with the number of k-points used (see previous section).

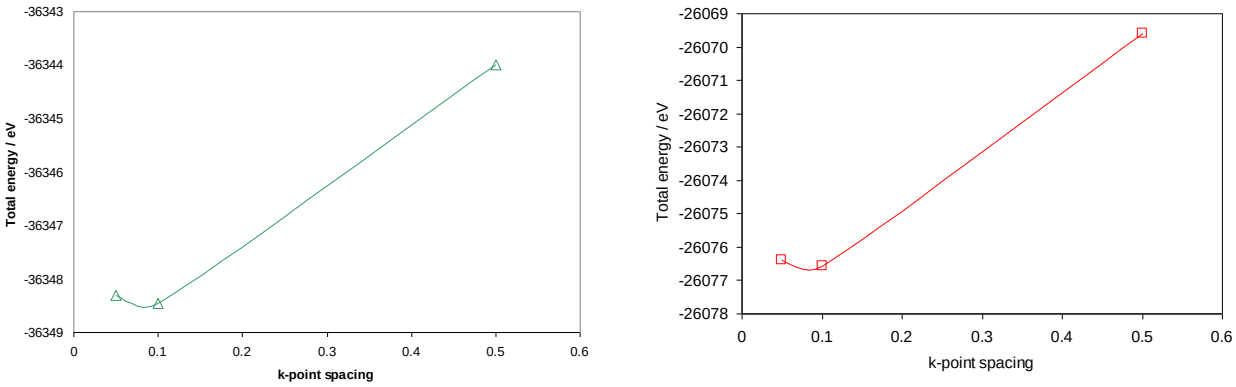


**Figure 1-12 Evolution of the final energy of $WO_3$ (red squares) and $(MoO_2)_2P_2O_7$ (green triangles) as a function of the k-point spacing using a Cutoff energy of 1200 eV.**

In Figure 1-12 we show that again the energy of the system is highly dependant on the k-point sampling. The smaller the k-point spacing, the more k-points are used to sample the periodic structure. However, for larger unit cells, an identical k-point spacing would lead to worse k-point sampling (fewer k-point in the Brillouin zone). Therefore, although the minimum energy seems to be reached for a k-spacing of 0.1, in our calculations, we chose use a k-point spacing of 0.05 to consistently potentially perform calculations on larger structures.

## 1.6. Powder diffraction techniques

### 1.6.1. General overview

A crystal can be described as an ordered arrangement of atoms. The positions of the atoms within the unit cell can be expressed as a function of three fractional coordinates x, y and z. The 3D nature of the structure means it is convenient to introduce planes denoted (hkl) where h, k and l are Miller indices and used to describe the orientation of the planes relative to their intersection with the unit cell axes. When electromagnetic radiation of a suitable wavelength is sent onto an array of unit cells (a crystal) at a given $\theta$ angle, the interference phenomenon that arises can be treated as if it occurs by radiation

being reflected from the (hkl) planes within the structure. If we consider a beam of in-phase waves sent onto an infinite number of planes, most of the diffracted waves will have randomly related phases and therefore will cancel each other out. For a crystalline structure, the only cases where the interferences will be constructive can be represented as in Figure 1-13.

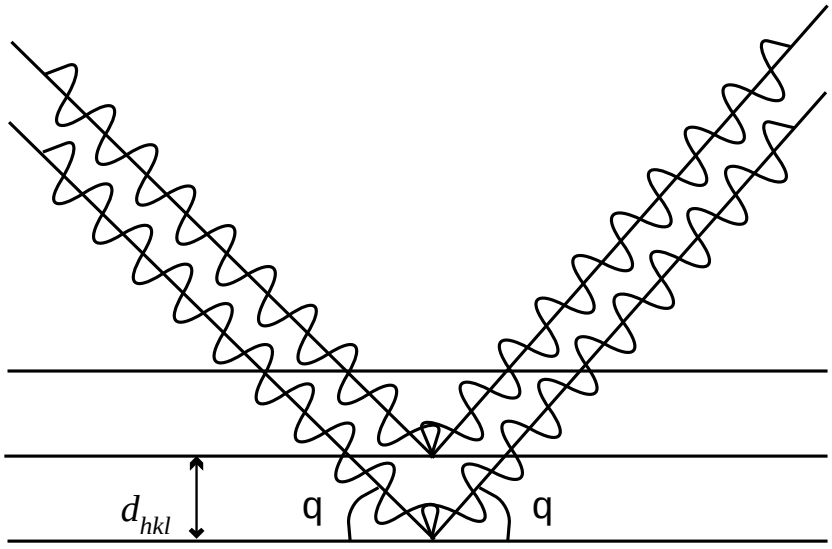


**Figure 1-13 Schematic representation of the geometrical conditions to produce constructive interference when applying a monochromatic radiation onto a crystal.**

This picture shows that the path between two consecutive parallel planes should be equal to an integer multiple of the incident wavelengths for the resulting radiation to be in-phase and to create constructive interference that can be detected. This is expressed by Bragg's law:

$$2d_{hkl}\sin\theta = n\lambda$$

The most common crystal structure determination techniques use X-ray and neutron radiation as their wavelengths are of the same order of magnitude as interatomic distances. The two techniques are similar because they both follow the principles described above. However, the interaction between matter and X-rays or neutrons is quite different and interpretation of the resulting diffraction experiment can very often lead to complementary information. X-rays interact directly with the electrons surrounding the nucleus and, therefore, the scattering factor increases with the number of electrons present. The intensity of the diffracted beam, is therefore more influenced by heavy atoms. In a structure where both heavy and light atoms are present, contributions to reflections from light atoms can be low. The use of X-ray diffraction in such a sample would then provide reliable information on the position of the electron-rich elements while the uncertainty on other atomic positions might be significant. Neutrons interact not with electrons but with the nucleus itself. Two consecutive elements in the periodic table that are hardly distinguishable by X-rays can therefore scatter neutrons very differently and be differentiated. In the systems studied in this work, however the main advantage of neutrons is that the scattering power of light elements (such as oxygen) can be comparable to heavy elements and therefore bring complementary information to X-ray data.

Most commonly, diffraction experiments are performed using constant wavelength monochromatic radiation. In a single crystal experiment, the crystal can be rotated in 3D bringing different (hkl) planes into the diffracting (Bragg) condition. Individual reflections can then be measured and integrated using 2D detectors allowing structure determination. When dealing with a powdered sample, the crystallites are orientated in different directions and the projection on a photographic film or 2D image of the reflection for a given $d_{hkl}$ plane would result in a circle and not a dot as in the single crystal experiment. Moreover, depending on the intrinsic symmetry of the crystal, some hkl reflections (those with identical $d_{hkl}$) will fall onto the same circle and therefore become indistinguishable. In practice, powder diffraction data are not recorded on a film but by a "single line" detector and the powder pattern is then represented as a plot of integrated intensity as a function of the diffracted $2\theta$ angle. A given peak in the powder pattern can therefore correspond to one or several overlapping reflections. This loss of resolution between the different reflections makes structure solution (via indexation, integration, solution and refinement) much more challenging than in a single crystal experiment.

The dots/peak positions in a diffraction pattern are determined by the symmetry and the size of the unit cell. The intensities of the peaks depend on the arrangement of the scattering density within the sample (i.e the atoms present and their corresponding coordinates).

### 1.6.2. Rietveld refinement

It is straightforward to simulate a diffraction pattern from a structure whose unit cell parameters and atomic positions are known. One can then compare experimental data to a reported or proposed structure. If the two patterns (calculated and experimental) present convincing similarities, a refinement of the structure can be attempted so that calculated pattern fits the experimental data better. One thus obtains a better description of the structure. Several criteria of fit are conventionally defined for such analysis and are documented in this thesis using the Bruker DIFFRAC$^{plus}$ TOPAS v4 software conventions described below.

The normal refinement of the structure can be done by the Rietveld method[18, 19] where experimental and calculated patterns are expressed as $y_i(\mathrm{obs})$ and $y_i(\mathrm{calc})$ respectively and the difference between the two is minimised as quantified by the $R$-weighted pattern:

$$R_{wp} = \sqrt{\frac{\sum_i w_i \left[ y_i(obs) - y_i(calc) \right]^2}{\sum_i w_i \left[ y_i(obs) \right]^2}}$$

Where $y_i(obs)$ is the value of the data at a data point $i$, $w_i = \frac{1}{\sigma(y_i(obs))^2}$ is the weighting of a data point $i$ (with $\sigma(y_i(obs)) = \sqrt{y_i(obs)}$ being the normal error assured for observation).

If $p$ parameters are refined for an experimental pattern of n data points a statistically expected $R$-factor ($R_{exp}$) can be expressed as:

$$R_{\exp} = \sqrt{\frac{(n-p)}{\sum_{i=1}^{n} w_i (y_i(obs))^2}}$$

The best fit is obtained for a minimal $R_{wp}$ value and the goodness of fit can then be expressed by:

$$gof = \sqrt{\chi^2} = \left( \frac{R_{wp}}{R_{\exp}} \right)$$

However, the weighting parameter found in both $R_{wp}$ and $R_{exp}$ expression can sometimes lead to a wrong appreciation of the quality of a fit, in particular in the case of samples with strong background signal or poor signal to noise ratio. The validity of a Rietveld refinement should therefore be verified using an additional criterion based on single crystal data refinement techniques. The agreement between the observed integrated intensity of a given reflection ($I_{hkl}(obs)$) and a modelled integrated intensity ($I_{hkl}(calc)$) extracted independently from the experimental profile can be quantified by calculating the $R_{Bragg}$ factor expressed by:

$$R_{Bragg} = \frac{\sum_{hkl} \left| I_{hkl}(obs) - I_{hkl}(calc) \right|}{\sum_{hkl} \left| I_{hkl}(obs) \right|}$$

A high Bragg factor can therefore directly reveal a bad agreement between experimental data and a proposed structure.

### 1.6.3. Distance Least Squares (DLS) method

The DLS method was first introduced by Meier and Villiger[20]. In this method, the atomic positions, usually obtained from a known starting structure, are adjusted in order to fit some distances and bond angles values conditions. The ideal bond lengths and angles ( $D_0^j$ ) are defined by the user and the optimised model from a DLS refinement is obtained by minimising the following quantity:

$$\rho_\omega^2 = \sum_j \sum_{m,n} \omega_j^2 \left( D_{m,n}^{(j)} - D_0^{(j)} \right)^2$$

Where $\omega_j$ is the weight assigned to a given bond length of type $j$. $D_0^j$ and $D_{m,n}^j$ are the ideal and calculated new $j$ type distances for an atom between atoms $m$ and $n$ with a given sets of atomic coordinates.

In this work, we use DLS method to generate model structures and investigate how local distortions might influence NMR parameters.

## 1.7. References


1. M. A. Alla, E. I. Kundla, E. T. Lippmaa, *Jetp Letters* **27**, 194-197 (1978).
2. M. M. Maricq, J. S. Waugh, *Journal of Chemical Physics* **70**, 3300-3316 (1979).
3. A. Bax, R. Freeman, T. A. Frenkiel, *Journal of the American Chemical Society* **103**, 2102-2104 (1981).
4. A. Lesage, C. Auger, S. Caldarelli, L. Emsley, *Journal of the American Chemical Society* **119**, 7867-7868 (1997).
5. F. Fayon, G. Le Saout, L. Emsley, D. Massiot, *Chemical Communications*, 1702-1703 (Aug 21, 2002).
6. M. Feike, R. Graf, I. Schnell, C. Jager, H. W. Spiess, *Journal of the American Chemical Society* **118**, 9631-9634 (Oct 9, 1996).
7. M. Baldus, B. H. Meier, *Journal of Magnetic Resonance Series A* **121**, 65-69 (Jul, 1996).
8. P. Hartmann, C. Jana, J. Vogel, C. Jager, *Chemical Physics Letter* **258**, 107-112 (7 May 1996, 1996).
9. R. J. Iuliucci, B. H. Meier, *Journal of the American Chemical Society* **120**, 9059-9062 (Sep 9, 1998).
10. M. H. Levitt, D. P. Raleigh, F. Creuzet, R. G. Griffin, *Journal of Chemical Physics* **92**, 6347-6364 (1990).
11. S. T. Norberg, G. Svensson, J. Albertsson, *Acta Crystallographica Section C-Crystal Structure Communications* **57**, 225-227 (Mar, 2001).
12. F. Fayon, D. Massiot, M. H. Levitt, J. J. Titman, D. H. Gregory, L. Duma, L. Emsley, S. P. Brown, *Journal of Chemical Physics* **122** (May 15, 2005).
13. E. R. Andrew, A. Bradbury, R. G. Eades, V. T. Wynn, *Physics Letters* **4**, 99-100 (1963).
14. D. P. Raleigh, M. H. Levitt, R. G. Griffin, *Chemical Physics Letters* **146**, 71-76 (Apr 29, 1988).
15. M. Hohwy, H. J. Jakobsen, M. Eden, M. H. Levitt, N. C. Nielsen, *Journal of Chemical Physics* **108**, 2686-2694 (1998).
16. Y. K. Lee, N. D. Kurur, M. Helmle, O. G. Johannessen, N. C. Nielsen, M. H. Levitt, *Chemical Physics Letters* **242**, 304-309 (Aug 18, 1995).
17. X. Helluy, C. Marichal, A. Sebald, *Journal of Physical Chemistry B* **104**, 2836-2845 (Apr 6, 2000).
18. H. M. Rietveld, *Acta Crystallographica* **22**, 151-& (1967).
19. H. M. Rietveld, *Journal of Applied Crystallography* **2**, 65-& (1969).
20. W. M. Meier, H. Villiger, *Zeitschrift Fur Kristallographie Kristallgeometrie Kristallphysik Kristallchemie* **129**, 411-& (1969).

# Chapter 2. Literature review

## 2.1 Introduction

Understanding the structures and the technological applications of inorganic solids have always been matters of great interest. In this thesis, experimental and theoretical techniques were combined to investigate the behaviours of three inorganic compounds of structural and physical interest. The combination of the three major solid-state techniques reviewed in Chapter 1 (solid-state NMR, diffraction studies and ab-initio calculations) can provide information on the structural behaviour of these compounds. Due to the intrinsic properties of the elements present, different obstacles to obtaining accurate structures are encountered by the two experimental techniques.

In this thesis, $^{31}$P and $^{17}$O solid-state NMR investigations are considered. The main challenge we meet when looking at materials with similar $^{31}$P sites in pyrophosphates by NMR comes from the insufficient resolution of the numerous $^{31}$P resonances in samples. In $^{17}$O NMR studies, the second order quadrupolar broadening and the overlap of resonances often make information difficult to extract. This effect is also worsened by the poor sensitivity of $^{17}$O and leads to a poor signal to noise ratio. However, in both cases, the NMR spectra are exploitable when related to structures determined by diffraction methods.

In oxides, the accurate determination of atomic positions often requires using combined data resulting from both X-ray and neutron studies. Moreover, obtaining high quality single crystals can also be challenging or impossible so experiments have to be performed on powdered samples resulting in loss of information and a more difficult analysis.

The results of ab-initio calculations of NMR parameters can be compared to experimental data. In the case of good agreement, they are used to determine parameters that would otherwise be difficult to extract experimentally. They can also be used to predict the behaviour of model structures.

We will first review here previous $^{31}$P NMR and diffraction studies used for structure determination of pyrophosphates. We will then present how limitations in the interpretation of $^{17}$O NMR experiments have been overcome by the introduction of ab-initio calculation techniques.

## 2.2 $^{31}$P NMR

### 2.2.1 Relationships between structures and $^{31}$P NMR parameters

The $^{31}$P nucleus is well suited for NMR studies. Its natural abundance is 100% and it also has a high magnetic sensitivity ($6.63 \times 10^{-2}$ for $^{31}$P and $1.59 \times 10^{-2}$ for $^{13}$C). Another advantage of studying this nucleus is that as a ½ spin, its NMR signal is not broadened by quadrupolar effects.

Despite the ease of obtaining high quality spectra, it has been difficult to find direct relationships between the structures of phosphorus compounds and their NMR parameters. Looking at some orthophosphates, Turner *et al*. related the isotropic chemical shift values to the number of electrons in the $\pi$ orbitals or to the nature of the neighbouring cations[(1)]. However, these correlations are applicable only to a very restricted number of orthophosphates (involving similar bond angles and neighbouring ligands) and are not suitable help the determination of the much wider range of existing phosphorus compounds. A more general and comprehensible correlation was proposed by Cheetman et *al*.[(2)] who found that a relationship exists between $\delta_{iso}$ and the summed oxygen atom bond strengths in a wide range of phosphates compounds known. This bond strength quantity described by Brown and Shannon[(3)] is related to the bond lengths and makes this correlation more interesting since the chemical shift values can be connected directly to a structural characteristic of the system.

Due to the wide variety of crystalline phosphorus compounds and the large number of studies performed, the following review focuses mainly on pyrophosphate compounds which are the most relevant to this work.

### 2.2.2 Structure of $AP_2O_7$ compounds

$AP_2O_7$ compounds (A= Th, U, Pb, Ce, Hf, Zr, Ti, Mo, W, Re, Pb, Sn, Ge or Si)[(4)] exist with a cubic structure which may be described as a network of corner sharing of $PO_4$ tetrahedra and $AO_6$ octahedra. A simple polyhedral representation of the structure is shown in Figure 2-1a). The $PO_4$ units are arranged in pairs sharing a common oxygen. The three remaining oxygens of each tetrahedron form a P-O-A linkage. The highest symmetry space group possible for $AP_2O_7$ is $Pa\bar{3}$ in which the unique $P_2O_7$ groups has a linear P-O-P angle with its oxygen lying on the centre of inversion of the structure (Figure 2-1a)). At high temperature, $AP_2O_7$ compounds appear by diffraction data to have this ideal cubic structure presumably due to the dynamic disorder of the P-O-P linkage giving a 180° bond angle on average. As the temperature decreases, the structure becomes more complex as some P-O-P bond angles are “frozen” at a conformation away from a 180˚ angle. The possible space groups derived from the $Pa\bar{3}$ supergroup for angles bending away from linear configuration are presented in Table 2-1[(5, 6)] and a polyhedral representation of the 3x3x3 superstructure is shown in Figure 2-1b).

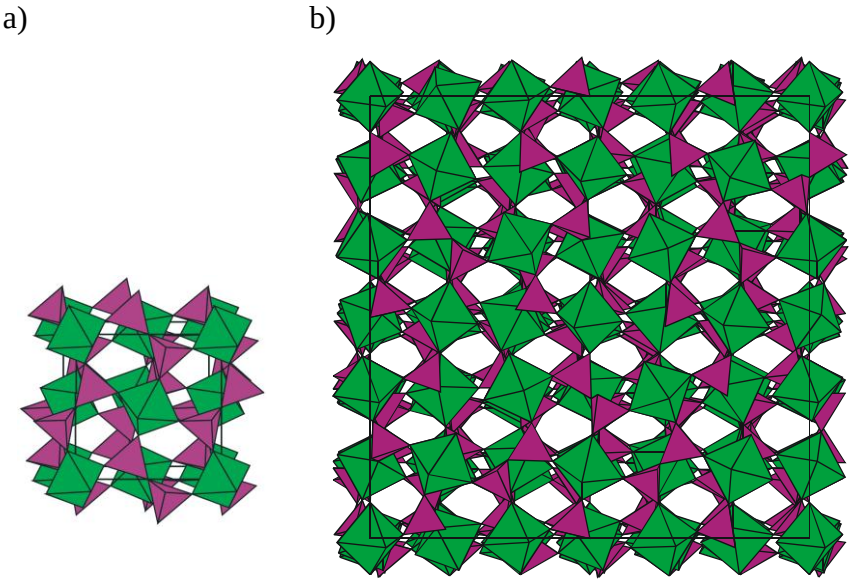


**Figure 2-1 Representation of a partial view of the 1x1x1 high symmetry/temperature structure (a) and the 3x3x3 superstructure (b) of $MP_2O_7$ in the cubic $Pa\bar{3}$ subgroup described by Tillmanns *et al*[7].**

In these compounds, two $^{31}P$ sites can be related by a centre of inversion and are referred to as equivalent as they present the same chemical shifts and the same chemical shift anisotropy (see Chapter 1). All the other $^{31}P$ are inequivalent. The subgroups present different numbers of equivalent or inequivalent $^{31}P$ sites and $P_2O_7^{2-}$ groups. Correlating these symmetry properties and results of solid-state NMR experiments reduces the number of possible subgroups that a structure can adopt, and can sometimes determine without any ambiguity the symmetry of an $AP_2O_7$ compound.

**Table 2-1 Possible space groups for the superstructure of $AP_2O_7$ compounds resulting from the distortions of the ideal high temperature 1x1x1 cubic structure ($Pa\bar{3}$) and the corresponding numbers of $^{31}P$ sites and $P_2O_7$ groups. The table taken from references 5 and 6.**

| Space group | No. of $P_2O_7$ groups with two equivalent P sites | No. of $P_2O_7$ groups with two inequivalent P sites | No. unique P sites |
|---|---|---|---|
| $Pa\bar{3}(1\times1\times1)$ | 1 | | 1 |
| $Pa\bar{3}$ | 1 | 5 | 11 |
| $P2_13$ | | 11 | 22 |
| $R\bar{3}$ | 2 | 18 | 38 |
| $R3$ | | 38 | 76 |
| $Pbca$ | 1 | 13 | 27 |
| $Pca2_1$ | | 27 | 54 |
| $P2_12_12_1$ | | 27 | 54 |
| $P2_1/c$ | 2 | 26 | 54 |
| $Pc$ | | 54 | 108 |
| $P2_1$ | | 54 | 108 |
| $P\bar{1}$ | 4 | 52 | 108 |
| $P1$ | | 108 | 216 |

Since the powder diffraction studies on these materials can often be ambiguous, solid-state NMR has been performed to great effect on a number of materials in the family. The techniques developed will be of relevance to the materials investigated in this thesis.

Three first members of this family that have mainly been studied by diffraction and NMR methods are $SiP_2O_7$[7], $TiP_2O_7$[8] and $ZrP_2O_7$[4]. In these three compounds, X-ray diffraction and 1D NMR[5] initially concluded a 3x3x3 $Pa\bar{3}$ structure was present.

In $SiP_2O_7$, diffraction data analysis by Tillmanns *et al.*[7] predicted eleven non-equivalent phosphorus sites and concluded a $Pa\bar{3}$ space group. The first MAS NMR experiment on $SiP_2O_7$ were carried out by Hartmann *et al.* in 1996[9]. Two-dimensional dipolar coupling driven experiments were used to distinguish the cubic component from a mixture of five different $SiP_2O_7$ polymorphs and also to confirm the structure suggested by Tillmanns *et al.*[7].

The structure of the cubic $SiP_2O_7$ was further investigated by Iuliucci and Meier[10] by 2D exchange NMR spectroscopy using J-coupling (through bond) correlations (Figure 2-2). In the TOBSY experiment (as in the INADEQUATE described in Chapter 1), the cross peaks between the centerbands of the pattern identify pairs of phosphorus that belong to the same P-O-P unit. The experiment performed on $SiP_2O_7$ shown in Figure 2-2 therefore reveals five pairs of two inequivalent phosphorus linked by a bridging oxygen and one pair (P4/P4) where the two identical phosphorus are related by a center of inversion within the P-O-P unit (not correlated to any other in the centerbands pattern). This observation (see Table 2-1) confirms the $Pa\bar{3}$ structure proposed by Tillmanns et *al.*.

The TOBSY (Total through Bond Correlation Spectroscopy)[11] experiment was also used to determine the P-O-P bond angles by measuring the chemical shift anisotropy tensor orientations relative to the molecular frame.

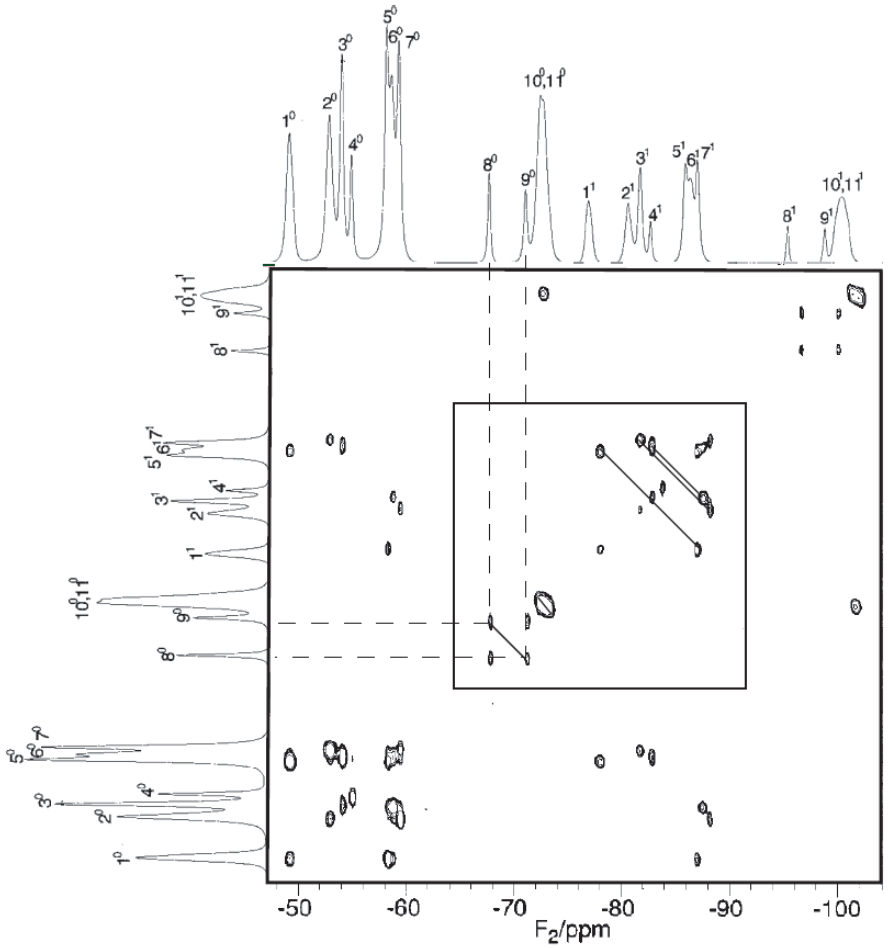


**Figure 2-2 2D $^{31}$P TOBSY spectra of $SiP_2O_7$ recorded at room temperature with a MAS frequency of 4.63 kHz and a mixing period of 21 ms[(10)]. The dotted lines connect the resonances of sites belonging to a same $P_2O_7$ unit. The solid line show the through bond P-O-P connectivities. The square at the center of the spectra shows the centerbands region.**

Looking at the relative intensities of the cross peaks between the centerbands and the spinning sidebands in the 2D experiment, the determination of the orientation of the CSA tensor following a procedure described by deJong *et al*.[(12)] was used to determine the P-O-P bond angles. 1D spin-echo experiment and Herzfeld-Berger[(13)] analysis were used to determine the J-coupling values. The Herzfeld-Berger[(13)] analysis lead to P-O-P bond angles of 148°, 147°, 150° for three of the spin-pairs (P(1)/P(5), P(2)/P(7) and P(3)/P(6)) consistent with the one obtained with diffraction data (144.4°, 143.5°, 146.5° respectively) and a J-coupling value J=23 Hz. The weak intensity P(8)-P(9) cross peaks confirmed that the P-O-P bond angle between these two phosphorus sites is close to 180°. The J-coupling value for this pair was found to be $J_{89}$=17 Hz. For the P(10)/P(11) pair, the overlap of two resonances does not allow such deductions but the presence of strong cross peaks between their different sideband orders indicates that these pairs must be bent away from 180° which again corroborate the diffraction data. These studies suggested that the J-coupling values increase with the P-O-P bond angle. In this work we describe other types of analysis to relate the J-coupling to bond angles but an opposite behaviour is observed.

The structure of $TiP_2O_7$ has also been investigated using $^{31}P$ NMR experiments[8]. At first sight, the 1D spectrum (Figure 2-3 a)) shows only 9 or 10 components for this structure. The observation of the intensities and the shapes of the patterns suggests that some signals have a triple multiplicity consistent with the hypothesis of $Pa\bar{3}$ symmetry similar to the $SiP_2O_7$ structure described by Tillmanns *et al.*[7] at the room temperature (with bond angles ranging from 139° to 145°). The 1D MAS NMR pattern also shows shifts in some of the peaks positions (at -15, -50 and –75 ppm) as the temperature is decreased (from 25 °C to -75 °C).

1D NMR experiments and different 2D MAS NMR have been used to assign the different chemical shifts[14]. Combining NMR data with the model provided for $SiP_2O_7$ (Figure 2-1), clear assignment of the different sites to corresponding NMR frequencies has been performed. As shown in Table 2-1, the different supercell space groups can be characterised by their number of $P_2O_7^{4-}$ units. The intensities obtained by deconvolution of the 1D spectrum are consistent with both $Pa\bar{3}$ and $P2_13$ space groups for the 3x3x3 superstructure. Although a $P2_1/3$ structure is expected to show a higher degree of spectral overlap, the determination of the number of $P_2O_7$ units within the compound can give very valuable complementary information to distinguish between these two space groups. Through-bond connectivities between two $^{31}P$ of a common $P_2O_7^{4-}$ unit were determined using 2D TOBSY experiment revealing $^3J_{iso}(^{31}P,^{31}P)$ interaction but this time only looking at the centerbands region (Figure 2-3).

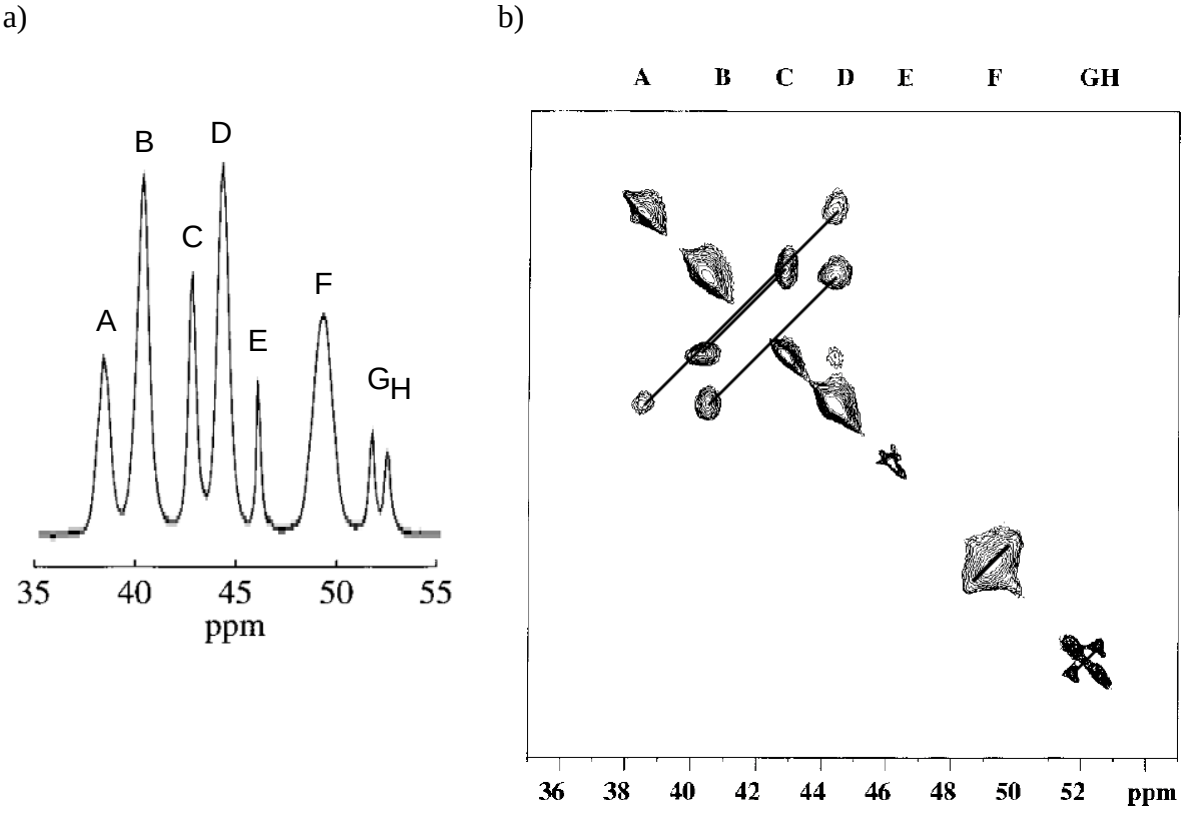


**Figure 2-3 1D $^{31}P$ NMR spectra (a) and 2D TOBSY MAS $^{31}P$ NMR experiment (b) on $TiP_2O_7$ recorded at 5.2 kHz[14]. The solid line show the through bond P-O-P connectivities.**

In Figure 2-3 b), the off-diagonal cross peaks show pairs of $^{31}$P sites sharing a bridging oxygen atom. In $TiP_2O_7$, five $P_2O_7$ units are revealed in which the two $^{31}$P sites are inequivalent. The $^{31}$P(E) peak represents a P-O-P group in which the two $^{31}$P are magnetically equivalent (related by inversion symmetry) and therefore not interacting through J-coupling. This shows clearly the presence of eleven peaks consistent with the $Pa\bar{3}$ space group. This two dimensional spectrum also allows one to distinguish peaks which were not resolved in the 1D spectrum ($^{31}$P(F)).

The information given by these two analyses were validated by two dipolar coupling experiments. 2D dipolar coupling driven experiments were performed with different mixing times (from 1.1 ms to 24.6 ms). Short mixing time experiments show almost the same spectrum as obtained with 2D TOBSY, because only large intra $P_2O_7^{4-}$- group interactions are probed. At longer mixing times, the 2D patterns show more cross peaks arising from weaker inter $P_2O_7^{4-}$ group dipolar coupling interactions. A set of 12 experiments with mixing times ranging from 1.1 ms to 24.6 ms were performed and the evolution of the intensity of the signals as a function of the mixing time was analysed. The experimental build-up curves of each cross peaks (intensity vs mixing time) were compared to that predicted for each $^{31}$P site considering the X-ray diffraction data and a purely dipolar Hamiltonian. Such comparison has given very good agreement in previous studies on $Cd_3(PO_4)_2$[15]. In the case of $TiP_2O_7$ useful structure supporting information was obtained, but the lack of resolution of certain peaks meant that it was impossible to relate each build up curve to a single experimental interaction.

Whilst NMR concluded that $SiP_2O_7$ and $TiP_2O_7$ had a $Pa\bar{3}$ symmetry with 11% of P-O-P bonds linear, different conclusions have been reached for $ZrP_2O_7$. In $ZrP_2O_7$, the presence of an a-glide within the structure predicted from electron diffraction data suggested that the superstructure subgroup could be either cubic $Pa\bar{3}$ or orthorhombic Pbca[4, 5]. The structure would then either present eleven $^{31}$P sites and five unique $P_2O_7$ groups or 27 $^{31}$P sites and 13 unique $P_2O_7^{4-}$ units respectively within its unit cell (Table 2-1). Here again, powder diffraction methods are limited and therefore NMR techniques were used in order to provide complementary information.

The 1D spectra for this compound, shown in Figure 2-4, could be seen and fitted as a superposition of eleven $^{31}$P peaks and $ZrP_2O_7$ has for long has been accepted to be a $Pa\bar{3}$ superstructure[5]. Even though refinements on neutron diffraction data for $Pa\bar{3}$ space group gave unreasonable interatomic distances (1.44 Å<P-O<1.66 Å and 1.91 Å<Zr-O<2.24 Å while typical values should be around 1.50 Å and 2 Å respectively) and doubts about this 1D spectra interpretation were expressed[16], this assumption was for long trusted.

Further NMR experiments on $ZrP_2O_7$ were carried out six years later by introducing variable spinning speed 1D and 2D dipolar interaction driven MAS NMR experiments[17]. The variable spinning speed 1D MAS experiments are shown in Figure 2-4.

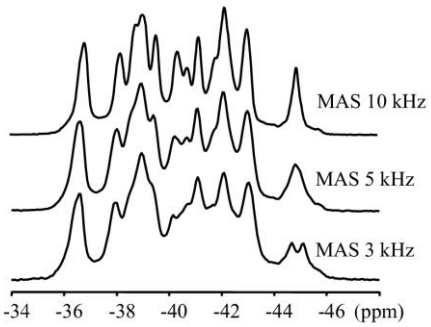


**Figure 2-4 1D $^{31}$P MAS NMR spectra of $ZrP_2O_7$ recorded at different spinning speeds**

It can be noted that the overall pattern changes quite significantly at different spinning speeds with the lines becoming sharper as the spinning speed increases. The broadening of the peaks at lower spinning speeds can be attributed to the existence of residual dipolar couplings between some of the phosphorus in the structure under MAS. The dipolar coupling is also responsible for the splitting of the $^{31}$P resonance situated around -44.5 ppm for a spinning speed of 3 kHz which disappears while reaching 10 kHz. The 1D $^{31}$P NMR spectra of pyrophosphates should therefore be interpreted carefully as such artefact could be misleading on the number of inequivalent $^{31}$P atoms present in the structure.

In Figure 2-4, the spectra recorded at 10 kHz suggests the presence of at least thirteen $^{31}$P sites within the studied sample. Therefore, if these 13 peaks arise from a single phase of $ZrP_2O_7$, the possibility of $ZrP_2O_7$ belonging to the 3x3x3 $Pa\bar{3}$ space group can be excluded. To confirm that all these peaks belong to the same phase and to disprove the hypothesis that some peaks might arise from impurities, a 2D exchange MAS experiment was performed. The so-called RFDR (Radio Frequency Driven Recoupling)[18-20] experiment uses the dipolar interaction in order to transfer the polarization between the $^{31}$P sites within the compound. This experiment showed correlations between all peaks displayed in the 1D spectrum confirming a single phase sample. This work therefore clearly confirmed that $ZrP_2O_7$ does not belong to 3x3x3 cubic $Pa\bar{3}$ but to the orthorhombic *Pbca* subgroup, the hypothesis of the $ZrP_2O_7$ superstructure belonging to the $Pa\bar{3}$ subgroup with only eleven unique $^{31}$P sites being ruled out.

Later, Fayon et *al.*[17] completed these results with a double quantum through bond (SQ-DQ refocused INADEQUATE) and through space (POST-C7) experiment[6]. The 2D MAS experiments are shown in Figure 2-5. These two techniques have been introduced in Chapter 1. The main advantage of using double quantum techniques is probably the unambiguous determination nature of the connecting P-O-P pairs provided by a clearer spectrum than the one that can be obtain by their single quantum analogues (as the TOBSY and RFDR experiments mentioned above for through bond and through space experiments respectively). In a double quantum 2D through-bond spectra (Figure 2-5a)), two equivalent $^{31}$P sites (related by a centre of inversion) do not give rise to any cross correlation peak. However, a double quantum dipolar (through-space) coupling driven experiment these equivalent sites will appear as diagonal cross peaks.

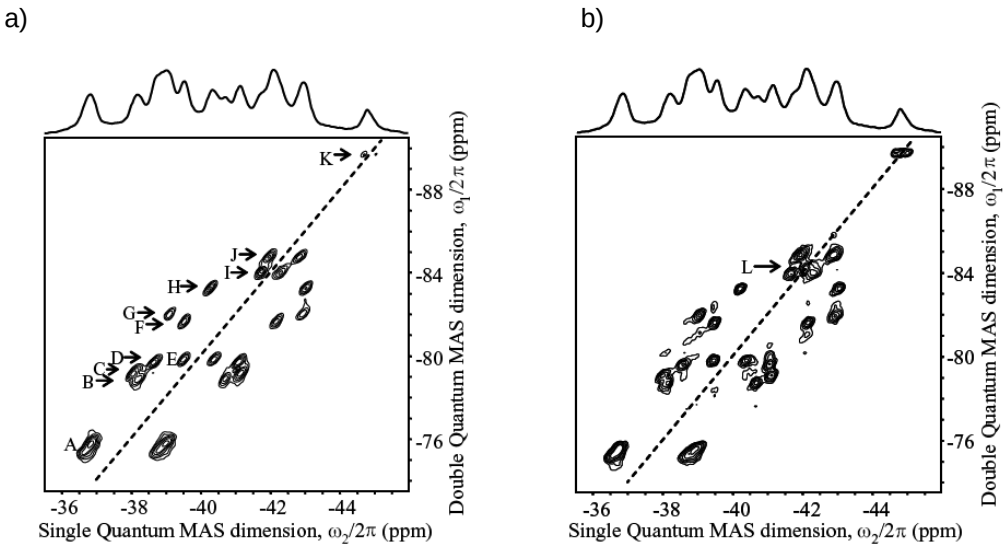


**Figure 2-5 2D single-quantum-double quantum MAS $^{31}$P NMR experiments for $ZrP_2O_7$ involving a) through-bonds interactions (INADEQUATE) and b) through-space interactions (POST C7[21]).**

The 2D INADEQUATE MAS spectrum (Figure 2-5a)) exhibits only P-O-P connectivities. The intensities of the different cross peaks have been used to get information on the number of overlapping $^{31}$P resonances present. From this study it was clear that the material contained thirteen Pa-O-Pb and one Pa-O-Pa group uniquely determining the space group Pbca. To obtain further information on how the P-O-P pairs are arranged relatively to each other on a longer range within the unit cell, through space interactions can be used by employing Double quantum MAS NMR experiments (POST-C7) using various mixing times as described earlier for $TiP_2O_7$.

Some $AP_2O_7$ compounds can adopt even more complex structures at room temperature. In compounds such as $\gamma$-$GeP_2O_7$[22] or $SnP_2O_7$[23], the direct interpretation of the 1D spectra is not conceivable as the majority of the $^{31}$P sites are unresolved (see Figure 2-6).

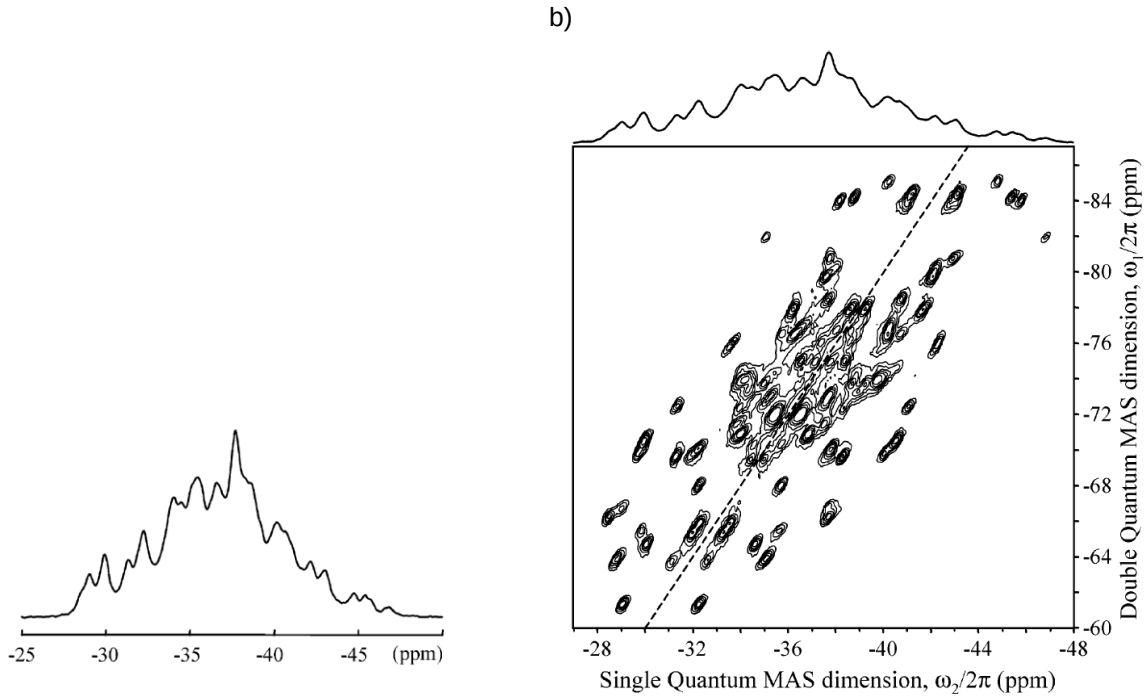


**Figure 2-6 a) 1D $^{31}$P MAS NMR and b) 2D INADEQUATE $^{31}$P NMR spectra of $SnP_2O_7$ recorded at a 10 kHz spinning frequency on a 300 MHz spectrometer.**

The spectrum in Figure 2-6 gives some ideas about the potential complexity of such pyrophosphate structures. The combination of the different NMR techniques described above concluded that γ-$GeP_2O_7$ or $SnP_2O_7$ these materials contain 216 and 108 phosphorus sites respectively.

## 2.3 $^{17}$O NMR

The presence of oxygen in many functional materials and the sensitivity of the $^{17}$O NMR parameters to variations of the structure make it an extremely promising nucleus to investigate by solid-state NMR. However, the characteristics of oxygen nuclei make such investigation by NMR difficult. Oxygen has three stable isotopes but only one of these ($^{17}$O) is observable by NMR. The low natural abundance of $^{17}$O (only 0.037%) and a low sensitivity ($2.91 \times 10^{-2}$ for $^{17}$O and $1.59 \times 10^{-2}$ for $^{13}$C) mean that enrichment with $^{17}$O sources are needed in order to obtain 1D NMR spectra in a reasonable amount of time. Moreover, $^{17}$O is a quadrupolar nucleus (I=5/2) and the second order effect of the quadrupolar interaction can lead to a broadening of the NMR signal and complicate the interpretation of data.

Thus, though this element is of major importance to understand, solid-state NMR studies have been limited both because of the cost of $^{17}$O enrichment and the complexity of the experiments required to obtain high resolution spectra. The principles and the applications of $^{17}$O solid state NMR have been reviewed[24-26].

In the work reported here, investigations were made using $^{17}$O to probe local structure in $WO_3$ and $ZrW_2O_8$ systems. In both cases, changes in temperature involve variations in the W-O distances and M-O-W bond angles (M=Zr or W). We used $^{17}$O NMR data and ab-initio calculations to correlate these

structural changes to the NMR parameters. We set the scene here by reviewing some of the previous attempts in correlating such parameters using $^{17}O$ NMR experiments and ab-initio calculations.

### 2.3.1 Structural interpretation of experimental $^{17}O$ NMR parameters

Although the determination of $^{17}O$ NMR parameter experimentally can be challenging, we review here some of the $^{17}O$ NMR works in which the NMR parameters (mainly isotropic chemical shift and quadrupolar coupling constants) were extracted and correlated to structural features.

Several works reported in the literature present the M-O distances around a given oxygen as an important factor in determining its isotropic chemical shift. For example, in ionic perovskites ($ABO_3$) and $A_2BO_3$ compounds (B=Ti, Zr, Sn, Nb, Al)[27], the nature of the B cation (and therefore the polarizing power of a given B-O bond as well as the B-O bond length) was shown to influence $^{17}O$ isotropic chemical shifts ($\delta_{iso}$) in such a way that structures with longer B-O bond lengths have more positive $\delta_{iso}$ values. Values were found to range from $\delta_{iso}$=372-564 ppm in titanates and $\delta_{iso}$=280-376 ppm in zirconates for average bond lengths of 1.995 Å and 2.093 Å respectively.

Later, studies on titanodiphenilsiloxanes (A=Si or Ti)[28] shown that each type of A-O-B linkage exhibits a certain range of chemical shifts depending on the nature of A and B. The $^{17}O$ isotropic chemical shifts of Si-O-Ti linkages were found in these studies to be intermediate (from 250 ppm to 400 ppm) of those found for Si-O-Si (from 0 ppm to 200 ppm) and Ti-O-Ti (above 500 ppm) linkages. Similarly, in sol-gels studies, chemical shift ranges were found around 0 ppm, 150 ppm and from 295 to 395 ppm for oxygens involved in Si-O-Si, Zr-O-Si and Zr-O-Zr linkages respectively.

Studies on compounds involving Ti-O bondings (sol-gel glasses or crystalline samples)[28-31] showed that the width of the range and the values of chemical shifts can also increase with the Ti coordination number. In these compounds[28], the presence of $^{17}O$ signal within a wide frequency range for Ti-$O_6$ oxygen type (from 300 to 375 ppm) suggests a very high sensitivity of the $^{17}O$ isotropic chemical shift to local structural details.

In crystalline pyrophosphates compounds ($\beta$-$Mg_2P_2O_7$, $Na_4P_2O_7$ , $\sigma$-$Ba_2P_2O_7$)[32], the isotropic shifts of the P-O-P bridging oxygens (P-O-P linkages) are larger than the “terminal” (P-O-M linkages) ones but no clear correlation between $\delta_{iso}$ and other parameters was shown. These studies also suggested that the $^{17}O$ isotropic chemical shifts could decrease with the P-O-P bond angles values. However, previous studies from the same group presented opposite behaviour for silica zeolites[33] and phosphate glasses[34] while looking at Si-O-Al and P-O-P bond angles respectively[33, 34]. Moreover, investigations by Bull *et al*.[35] on ferrierite zeolite refuted the existence of such simple correlation between $^{17}O$ NMR parameters and Si-O-Si bond angles. Ab initio calculations on silicates performed later on also could not spot clear correlations between Si-O-Si bond angle and $^{17}O$ $\delta_{iso}$[36-38].

The quadrupolar coupling values were found to vary as a function of the coordination of the oxide sites ranging from 1.2 MHz for tetrahedrally coordinate site up to 6 MHz for trigonally coordinate sites[39]. In their studies titanodiphenilsiloxanes, Gervais et *al.*[28] also mentioned a variation of the $C_Q$ with the nature of the A-O-B linkages. The oxygens in Si-O-Si linkage show larger $C_Q$ values than the ones in Ti-O-Si or Si-O-Al.

In ionic solids, $^{17}O$ chemical shift values seem therefore clearly influenced by the nature of the M-O bonds and the coordination of the surrounding cations. However, Schramm and Oldfield[40] predicted that the importance of the effect of the nature of the B ion on the $^{17}O$ chemical shift becomes less for more covalent systems. These structural parameters seem to also influence the $C_Q$ values

### 2.3.2 Determination of NMR parameters using ab-initio calculations

Quantum calculations have been also widely used to determine NMR parameters and the EFG (quadrupolar parameters) components of $^{17}O$ in various systems. First steps have been made using cluster calculations based on atomic orbital basis. Using such approximations, Grandinetti et *al.*[41-43] used GAUSSIAN to calculate $^{17}O$ EFG tensors on model clusters of silicates and germanates tetrahedral oxides. They confirmed Schramm and Oldfield's observations on the influence of the X cation electronegativity on the $C_Q$ values[40]. However, they pointed that both the quadrupolar asymmetry ($\eta_Q$) and the quadrupolar coupling ($C_Q$) are also likely to be affected by X-O-X ($\Omega$) bond angles. They found a correlation between the Si-O-Si bond angle and the amplitude of the $C_Q$ and $\eta_Q$ values. However, only the quadrupolar coupling constants seem to also be sensitive to Si-O bond lengths variation (at a given bond angle value). The relationships between this X-O-X angle ($\Omega$) and those two parameters are described by equation (1) and (2).

$$\eta_Q(\Omega) = b\left(\frac{1}{2} - \frac{\cos(\Omega)}{\cos(\Omega)-1}\right)^{\beta} \quad (1)$$

Extracting the experimental asymmetry parameter can lead to the determination of the X-O-X bond angle. Using the obtained values, experimental $C_Q$ values and equation (2)[43] would lead to X-O distances.

$$C_Q(d_{XO},\Omega) = a\left(\frac{1}{2} + \frac{\cos\Omega}{\cos\Omega - 1}\right)^{\alpha} + m_d \quad d_{XO} - d_{XO}^0 \quad (2)$$

A similar relationship has also been confirmed using DFT calculations on the same and larger germanate systems[44]. The accurate experimental measurement of the two quadrupolar parameters could then lead to the determination of both Si-O distances and Si-O-Si angles for each oxygen site within such structures.

The variation of the $C_Q$ parameter was compared between different groups of clusters. It was shown that families of optimised clusters with longer M-O bond distances show bigger $C_Q$ values regardless of the electronegativity of the M atom.

In their work on $SiO_2$ zeolites, Profeta et *al.*[38] looked at $^{29}Si$ and $^{17}O$ GIPAW calculated NMR parameters. The system under investigation contained up to 144 atoms per unit cell and calculations allowed the assignment of the ferrierite spectrum. No clear correlation between Si-O-Si bond angle and $^{17}O$ $\delta_{iso}$ or $C_Q$ parameter was found. However, $\eta_Q$ appeared to be correlated to the Si-O-Si bond angle but this parameter is more difficult to determine experimentally than $\delta_{iso}$ or $C_Q$.

Other DFT calculations using GIPAW method were performed by Charpentier et *al*.[36] on sodosilicate compounds and molecular dynamics simulated tetrasilicate glasses models. Calculations and experimental data gave good agreement and the bridging oxygen atoms parameters show correlation between $C_Q$ and $\eta_Q$ and Si-O-Si bond angles. For a given Si-O-Si angle, the $C_Q$ increases with the Si-O distance. However, no correlation between those parameters and the coordination number of the surrounding Na atoms were found which contradicts previous clusters studies by Clark and Grandinetti[45] cited earlier.

For non-bridging oxygen atoms, the $C_Q$ values are dependant on the types of silicon atoms they are linked to ($Q^{(3)}$or $Q^{(2)}$) due to the different average Si-O bond length while $\delta_{iso}$ seems to be insensitive to those distances variations. No clear correlation between the surrounding Na atoms geometry (Na-O distance, Si-O-Na angle, coordination number) and any of the NMR parameters has been highlighted. $C_Q$ and $\eta_Q$ were also were shown to be linearly correlated.

Recent investigations on $WO_3$ (also presented in Chapter 5) and Earth mantle[46, 47] compounds using $^{17}O$ MAS NMR experiments combined with first principle calculations (GIPAW) revealed an increase of the $\delta_{iso}$ and $C_Q$ amplitude with the M-O bond length (M=W or Si).

As mentioned in Chapter 1, the accuracy of DFT calculations can vary depending on the choice of several computational parameters. The exchange and correlation functional has to be adapted to the structure and to the type of calculations wanted. In Ca and Mg oxides and aluminosilicates, Profeta [48] found huge discrepancies between the calculated isotropic chemical shifts and experimental data on the CaO simple oxide show huge using the PBE functional especially for oxygens forming a ionocovalent bond with Ca cations. After modifications of the pseudopotential excellent agreement for $\delta_{iso}$ were obtained when applied to other structures but largely overestimate the bond lengths and the phonon frequencies. The calculations performed by Charpentier[36] using GIPAW method were made on sodosilicate compounds and molecular dynamics simulated tetrasilicate glasses models. The geometry were optimised using PARATEC code and gave a volume of the unit cell 4.5% bigger than the experimental values due to the use of generalised gradient approximation (GGA) PBE functional.

## 2.4 References


1. G. L. Turner, K. A. Smith, R. J. Kirkpatrick, E. Oldfield, *Journal of Magnetic Resonance* **70**, 408-415 (1986).
2. A. K. Cheetham, N. J. Clayden, C. M. Dobson, R. J. B. Jakeman, *Journal of the Chemical Society-Chemical Communications*, 195-197 (1986).
3. I. D. Brown, R. D. Shannon, *Acta Crystallographica Section A* **A 29**, 266-282 (1973).
4. N. Khosrovani, V. Korthuis, A. W. Sleight, T. Vogt, *Inorganic Chemistry* **35**, 485-489 (Jan 17, 1996).
5. V. Korthuis, N. Khosrovani, A. W. Sleight, N. Roberts, R. Dupree, W. W. Warren, *Chemistry of Materials* **7**, 412-417 (Feb, 1995).
6. F. Fayon, I. J. King, R. K. Harris, J. S. O. Evans, D. Massiot, *Comptes Rendus Chimie* **7**, 351-361 (Mar-Apr, 2004).
7. Tillmann.E, W. Gebert, W. H. Baur, *Journal of Solid State Chemistry* **7**, 69-84 (1973).
8. J. Sanz, J. E. Iglesias, J. Soria, E. R. Losilla, M. A. G. Aranda, S. Bruque, *Chemistry of Materials* **9**, 996-1003 (Apr, 1997).
9. P. Hartmann, C. Jana, J. Vogel, C. Jager, *Chemical Physics Letter* **258**, 107-112 (7 May 1996, 1996).
10. R. J. Iuliucci, B. H. Meier, *Journal of the American Chemical Society* **120**, 9059-9062 (Sep 9, 1998).
11. M. Baldus, B. H. Meier, *Journal of Magnetic Resonance Series A* **121**, 65-69 (Jul, 1996).
12. A. F. Dejong, A. P. M. Kentgens, W. S. Veeman, *Chemical Physics Letters* **109**, 337-342 (1984).
13. J. Herzfeld, A. E. Berger, *Journal of Chemical Physics* **73**, 6021-6030 (1980).
14. X. Helluy, C. Marichal, A. Sebald, *Journal of Physical Chemistry B* **104**, 2836-2845 (Apr 6, 2000).
15. S. Dusold, J. Kummerlen, T. Schaller, A. Sebald, W. A. Dollase, *Journal of Physical Chemistry B* **101**, 6359-6366 (1997).
16. A. M. K. Andersen, P. Norby, *Acta Crystallographica Section B-Structural Science* **56**, 618-625 (Aug, 2000).
17. I. J. King, F. Fayon, D. Massiot, R. K. Harris, J. S. O. Evans, *Chemical Communications*, 1766-1767 (Sep 21, 2001).
18. A. E. Bennett, J. H. Ok, R. G. Griffin, S. Vega, *Journal of Chemical Physics* **96**, 8624-8627 (Jun 1, 1992).
19. Y. Ishii, *Journal of Chemical Physics* **114**, 8473-8483 (May 15, 2001).
20. A. E. Bennett, C. M. Rienstra, J. M. Griffiths, W. G. Zhen, P. T. Lansbury, R. G. Griffin, *Journal of Chemical Physics* **108**, 9463-9479 (Jun 8, 1998).
21. M. Hohwy, H. J. Jakobsen, M. Eden, M. H. Levitt, N. C. Nielsen, *Journal of Chemical Physics* **108**, 2686-2694 (1998).

22. E. R. Losilla, A. Cabeza, S. Bruque, M. A. G. Aranda, J. Sanz, J. E. Iglesias, J. A. Alonso, *Journal of Solid State Chemistry* **156**, 213-219 (January 3, 2001, 2001).
23. F. Fayon, I. J. King, R. K. Harris, R. K. B. Gover, J. S. O. Evans, D. Massiot, *Chemistry of Materials* **15**, 2234-2239 (2003).
24. S. E. Ashbrook, M. E. Smith, *Chemical Society Reviews* **35**, 718-735 (2006).
25. S. E. Ashbrook, M. J. Duer, *Concepts in Magnetic Resonance A* **28A**, 183-248 (May, 2006).
26. K. J. Mackenzie, M. E. Smith, *Multinuclear solid-state NMR of inorganic materials* (Pergamon, Oxford, 2002).
27. T. J. Bastow, P. J. Dirken, M. E. Smith, H. J. Whitfield, *Journal of Physical Chemistry* **100**, 18539-18545 (Nov 21, 1996).
28. C. Gervais, F. Babonneau, D. Hoebbel, M. E. Smith, *Solid State Nuclear Magnetic Resonance* **17**, 2-14 (2000).
29. G. Mountjoy, D. M. Pickup, G. W. Wallidge, R. Anderson, J. M. Cole, R. J. Newport, M. E. Smith, *Chemistry of Materials* **11**, 1253-1258 (May, 1999).
30. T. J. Bastow, G. A. Botton, J. Etheridge, M. E. Smith, H. J. Whitfield, *Acta Crystallographica Section A* **55**, 127-132 (Mar 1, 1999).
31. P. J. Dirken, M. E. Smith, H. J. Whitfield, *Journal of Physical Chemistry* **99**, 395-401 (Jan 5, 1995).
32. D. Prochnow, A. R. Grimmer, D. Freude, *Solid State Nuclear Magnetic Resonance* **30**, 69-74 (Sep, 2006).
33. D. Freude, T. Loeser, D. Michel, U. Pingel, D. Prochnow, *Solid State Nuclear Magnetic Resonance* **20**, 46-60 (Aug-Sep, 2001).
34. M. Zeyer, L. Montagne, C. Jager, *Glass Science and Technology* **75**, 186-190 (2002).
35. L. M. Bull, B. Bussemer, T. Anupold, A. Reinhold, A. Samoson, J. Sauer, A. K. Cheetham, R. Dupree, *Journal of the American Chemical Society* **122**, 4948-4958 (May 24, 2000).
36. T. Charpentier, S. Ispas, M. Profeta, F. Mauri, C. J. Pickard, *Journal of Physical Chemistry B* **108**, 4147-4161 (Apr 1, 2004).
37. M. Benoit, M. Profeta, F. Mauri, C. J. Pickard, M. E. Tuckerman, *Journal of Physical Chemistry B* **109**, 6052-6060 (Apr 7, 2005).
38. M. Profeta, F. Mauri, C. J. Pickard, *Journal of the American Chemical Society.* **125**, 541-548 (Jan 15, 2003).
39. T. H. Walter, E. Oldfield, *Journal of Physical Chemistry* **93**, 6744-6751 (1989).
40. S. Schramm, E. Oldfield, *Journal of the American Chemical Society* **106**, 2502-2506 (1984).
41. T. M. Clark, P. J. Grandinetti, *Solid State Nuclear Magnetic Resonance* **16**, 55-62 (May, 2000).
42. T. M. Clark, P. J. Grandinetti, *Journal of Non-Crystalline Solids* **265**, 75-82 (Mar, 2000).
43. T. M. Clark, P. J. Grandinetti, *Journal of Physics-Condensed Matter* **15**, S2387-S2395 (Aug 13, 2003).
44. T. H. Sefzik, J. B. Houseknecht, T. M. Clark, S. Prasad, T. L. Lowary, Z. Gan, P. J. Grandinetti, *Chemical Physics Letters* **434**, 312-315 (Feb 5, 2007).

45. T. M. Clark, P. J. Grandinetti, P. Florian, J. F. Stebbins, *Journal of Physical Chemistry B* **105**, 12257-12265 (Dec 13, 2001).
46. A. Soleilhavoup, M. R. Hampson, S. J. Clark, J. S. O. Evans, P. Hodgkinson, *Magnetic Resonance in Chemistry* **45**, S144-S155 (2007).
47. S. E. Ashbrook, L. Le Polles, C. J. Pickard, A. J. Berry, S. Wimperis, I. Farnan, *Physical Chemistry Chemical Physics* **9**, 1587-1598 (2007).
48. M. Profeta, M. Benoit, F. Mauri, C. J. Pickard, *Journal of the American Chemical Society* **126**, 12628-12635 (Oct 6, 2004).

# Chapter 3. $^{31}$P SSNMR investigations on $\alpha$-$(MoO_2)_2P_2O_7$

## 3.1. Preliminary studies

### 3.1.1. Diffraction studies on the high and low temperature structures

The structure of $(MoO_2)_2P_2O_7$ at room temperature was reported for the first time by Kierkegaard in 1962[(1)] from single crystal experiments. It was described as a network of corner sharing $MoO_6$ octahedra and $PO_4$ tetrahedra. An alternation of two different types of $MoO_6$ ($Mo(1)O_6$ and $Mo(2)O_6$) octahedra form chains in the xz plane. Mo(1) is linked to its two adjacent $Mo(2)O_6$ via a trans linkage while Mo(2) connects to $Mo(1)O_6$ via a cis linkage (see Figure 3-1). There are two unique $PO_4$ groups present $P(1)O_4$ and $P(2)O_4$ linked to form $P_2O_7$ units in an eclipsed conformation with a P-O-P angle of 140.94°. $Mo(1)O_6$ and $P(1)O_4$ appear to be slightly more distorted than $Mo(2)O_6$ and $P(2)O_4$ respectively (see Table 3-1). Selected bond distances and bond angles within the polyhedra are reported in Table 3-1.

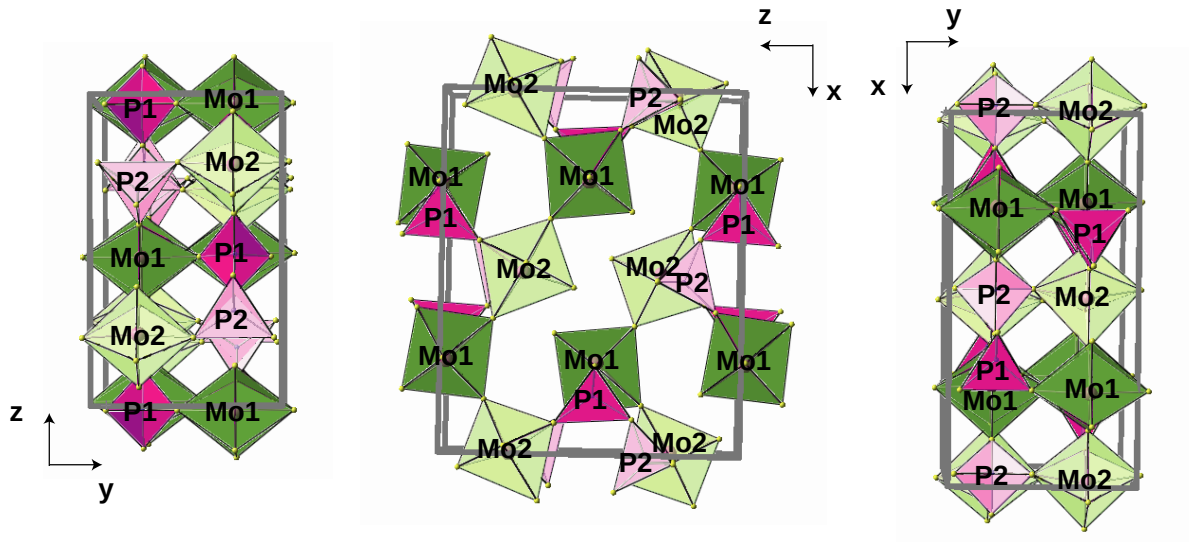


**Figure 3-1 Polyhedral representation of the Kierkegaard structure of $(MoO_2)_2P_2O_7$. $Mo(1)O_6$ and $Mo(2)O_6$ octahedra are represented in dark and light green respectively. P(1)O4 and $P(2)O_4$ tetrahedra are represented in dark and light pink respectively.**

However, at very long X-ray exposure times, Kierkegaard observed very weak intensity peaks and stated therefore that this relative arrangement of the polyhedra was only describing a subcell. The actual room temperature structure was thought to involve slight displacements of the lightest atoms (O and P) leading to structure with a unit cell larger than the one described. In our work, in collaboration with Sarah Lister, we aimed to reinvestigate the structure of this pyrophosphate and complete the work achieved by Kierkegaard.

**Table 3-1 Bond distances and angles within the $MoO_6$ octahedra and $PO_4$ tetrahedra in the structure given by Kierkegaard[1]. M is the central polyhedral atom, A is the first adjacent atom to M forming the M-A bond, B is the second adjacent atom forming the A-M-B bond angle.**

| M | A | M-A (Å) | B | A-M-B (°) | B | A-M-B (°) |
|---|---|---|---|---|---|---|
| Mo1 | O2 (P2) | 1.86681 | O4 | 87.91 | O2 | 159.85 |
| | | | O6 | 79.94 | | |
| | O2 (P2) | 1.86681 | O7 | 99.92 | | |
| | | | O9 | 88.96 | | |
| | O4 (P1) | 1.88882 | O6 | 81.14 | 09 | 161.90 |
| | O6 (Mo2) | 2.06478 | O9 | 80.77 | 07 | 173.21 |
| | O7(Mo2) | 1.93700 | O9 | 80.77 | | |
| | O9 (free) | 1.82847 | | | | |
| Mo2 | O1 (P1) | 1.96686 | O3 | 87.48 | O1 | 174.73 |
| | | | O6 | 92.24 | | |
| | O1 (P1) | 1.96686 | O7 | 88.71 | | |
| | | | O8 | 90.94 | | |
| | O3 (P2) | 2.09301 | O7 | 77.42 | O6 | 164.89 |
| | O6 (Mo1) | 1.87352 | O7 | 87.47 | | |
| | O7 (Mo1) | 2.17293 | | | O8 | 171.61 |
| | O8 (free) | 1.83325 | O3 | 94.18 | | |
| P1 | O1 (Mo1) | 1.58731 | O5 | 106.73 | | |
| | O1 (Mo1) | 1.58731 | O1 | 98.69 | | |
| | O4 (Mo1) | 1.63588 | O1 | 114.94 | | |
| | O5 (P2) | 1.59816 | O4 | 113.44 | | |
| P2 | O2 (Mo2) | 1.61427 | O5 | 101.53 | | |
| | O2 (Mo2) | 1.61427 | O2 | 111.08 | | |
| | O3 (P2) | 1.53959 | O2 | 114.57 | | |
| | O5 (Mo1) | 1.58674 | O3 | 112.02 | | |

A sample of $\alpha$-$(MoO_2)_2P_2O_7$ (SEL243) was synthesised and analysed by Sarah Lister following the synthetic route described by Schulz in 1955[2]. As described in Chapter 2, pyrophosphates are likely to adopt a simple high temperature structure, the symmetry of which decreases with temperature. The structure described by Kierkegaard is therefore likely to exist at high temperatures while at lower temperatures a more complex phase could appear. Lister's studies started by running high quality variable temperature powder X-ray experiment and some of the resulting data are shown in Figure 3-2.

The X-ray pattern of such a compound is largely dominated by the molybdenum atom scattering, therefore any change in the phosphorus or oxygen environment is likely to be relatively difficult to pin down in the X-ray diffractogram. However, the high quality of the data in Figure 3-2 revealed very

subtle differences between the patterns at room temperature and at high temperature. The intensity changes of strong reflections are minimal suggesting that the positions of molybdenum atoms change little in this process.

As the temperature decreases from 150 ºC to room temperature (Figure 3-2), very weak extra diffraction peaks arise. This suggests the occurrence of a phase transition involving displacement of phosphorus and oxygen atoms and therefore the existence of a superstructure at low temperature.

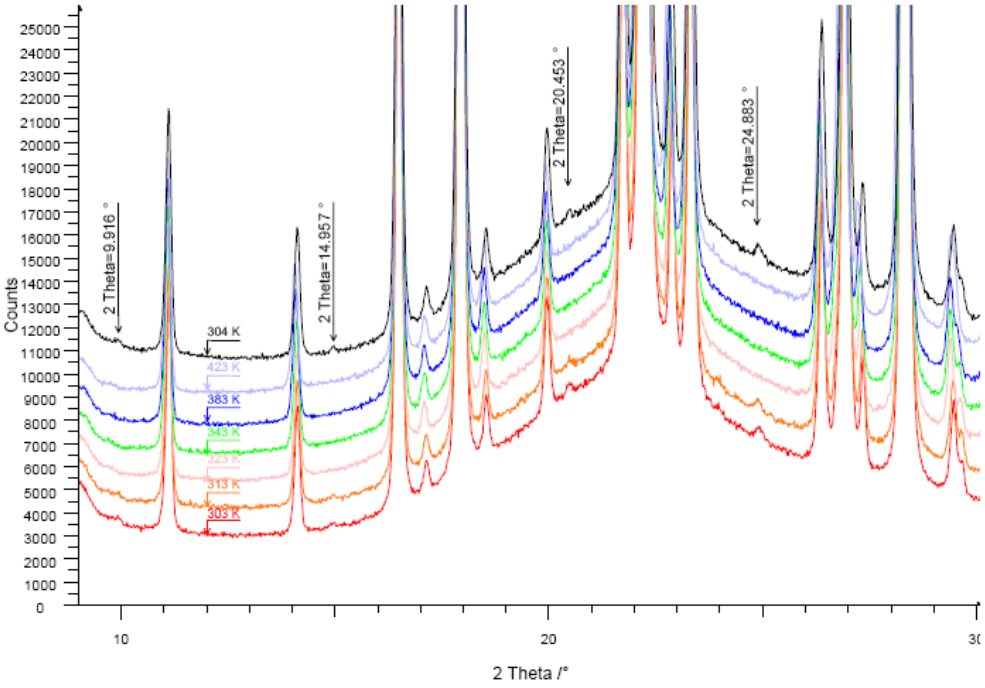


**Figure 3-2 Variable temperature powder X-ray data performed on a $(MoO_2)_2P_2O_7$ sample (SEL243) on heating to 423 K then cooling back to 300 K[(3)]. The vertical arrows indicate the positions of the diffraction peaks characteristic of the low temperature superstructure.**

A more visual clue of the occurrence of a phase transition is obtained from the variation of the different unit cell parameters as a function of temperature (Figure 3-3). These parameters were obtained by refinement of high resolution X-ray powder diffraction data. The data (especially the c parameter and the volume) show evidence of two phase transitions between about -40 °C and 180 °C (230 K and 450 K). One phase exists below 315 K, then a sudden jump in the c parameter and the volume occurs which then evolve smoothly up to about 90 °C (360 K) where the second transition occurs. These two discontinuities presumably correspond to first and second order phase transitions.

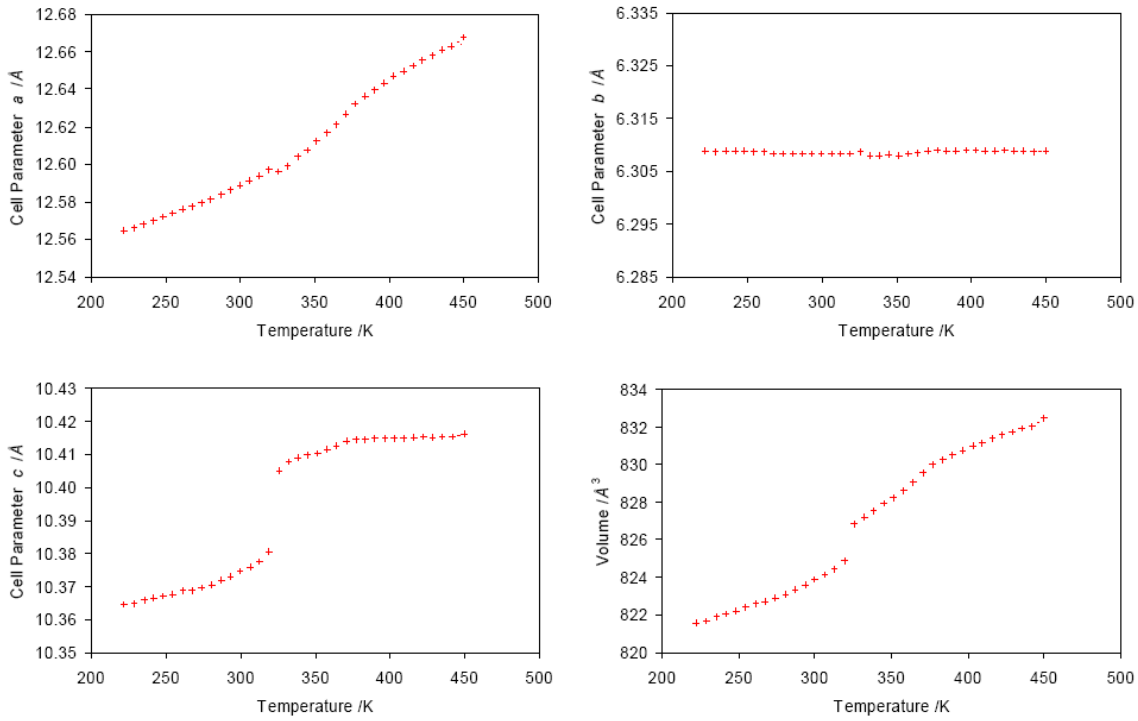


**Figure 3-3 Unit cell variation upon warming obtained from refinement on synchrotron data extracted from Sarah Lister's thesis[3] only small hysteresis were observed on the corresponding cooling plots**

$^{31}P$ is an ideally suited nucleus for NMR studies and the variations of the phosphorus environment in such range of temperatures could be probed. If the *Pnma* structure described by Kierkegaard corresponds to the subcell, then the group-subgroup symmetry relationships would allow five possible space groups for the lower symmetry structure ($P2_1/c$, $Pc$, $P2_1$, $P\bar{1}$ and $P1$).

A negative result on second harmonic generation (SHG) tests performed by Prof. Shiv Halasyamani (University of Houston) implied a centrosymmetric lattice type. This observation decreases the number of possible space groups for the superstructure to two: $P2_1/c$ and $P\bar{1}$. Other complementary studies on powder neutron data to produce compatible structures by simulated annealing methods could not unambiguously determine which structure is likely to be the most probable. The two hypothetical structures have eight and sixteen phosphorus (and molybdenum) atoms in their asymmetric units respectively. $^{31}P$ MAS NMR experiments should therefore potentially be a very powerful tool to complete the diffraction studies and differentiate between the different structural possibilities. In both possible structures, half of the phosphorus atoms are generated from each unique phosphorus (P1 and P2) existing in the high temperature phase and will be referred to as P1n, P2n (where n varies from 1 to 4 and from 1 to 8 in the $P2_1/c$ and $P\bar{1}$ structure respectively). We will also discuss how structural knowledge and NMR techniques can be combined to try to assign the NMR signals. 1D then 2D NMR experiments are presented and discussed.

### 3.1.2. 1D MAS NMR experiments

We know from previous NMR experiments on pyrophosphates that these compounds are likely to have very long relaxation times. Determination of the relaxation time was performed by preliminary "$T_1$ saturation" experiments. The $^{31}P$ MAS NMR spectrum of sample SEL322 was performed on a 500 MHz Varian spectrometer using a frequency of 202.28 MHz. The sample was packed in a 4 mm zirconia rotor and spun at 15 kHz. 100 saturation pulses separated by a 10 μs period were used. After the presaturation block, magnetisation was recovered over $\tau$ periods of 8 s, 16 s, 32 s, 64 s, 128 s, 256 s, 512 s, 1024 s and 2048 s. The intensities of the signal evolve as a function of the relaxation time and the $\tau$ value following the equation:

$$S(\tau) = A_0 * (1 - \exp(-\tau / T_1))$$

The data were fitted to this equation and the $T_1$ values are reported in Table 3-2.

**Table 3-2 Values of $T_1$ relaxation time for $(MoO_2)_2P_2O_7$ sample (SEL 322). The labelling of the lines corresponds to the one shown in Figure 3-4.**

| | Line a | Line b | Line c | Line d | Line e |
|---|---|---|---|---|---|
| $T_1$ / s | 329 | 320 | 316 | 251 | 181 |
| lower σ | -0.86 | 1.07 | 0.82 | -1.09 | -1.28 |
| upper σ | 0.86 | -1.07 | -0.82 | 1.09 | 1.28 |

For the subsequent variable temperature 1D experiments, pulse delays of 1024 s were used. Since the $T_1$ values are rather large, all the two dimensional experiments mentioned later were recorded using such a presaturation period in order to reduce the experimental time.

Variable temperature NMR experiments on $\alpha$-$(MoO_2)_2P_2O_7$ were carried out on a 500 MHz InfinityPlus Varian spectrometer (11.7 T magnet) giving a frequency of 202.28 MHz for $^{31}P$. $^{31}P$ chemical shifts were referenced to the signal from $H_3{}^{31}PO_4$ (80% aqueous solution) at 0 ppm. The deconvolution of the centerbands of the 0 °C and 150 °C patterns are shown in Figure 3-4 and the different resonances will be discussed later using the labelling shown in this picture. Deconvolution methods were also used to quantify the relative intensities of the $^{31}P$ signals in the low temperature structure. The integration of the central bands and spinning sidebands at 0°C gave a 2.9:1.5:1.2:1.3:3.3 ratio for lines a, b, c, d, e respectively. We will argue later that these are consistent with a 2:1:1:1:3 ratio with experimental uncertainty.

Figure 3-5 shows variable temperature $^{31}P$ NMR spectra recorded with a spinning speed of 5 kHz for SEL322 packed in a 4 mm outer diameter magic-angle spinning rotor. Note that frictional heating means that sample temperatures are an estimated 5-10 °C above the reported temperatures. In the following sections, we will mainly discuss the low and the high temperature spectra.

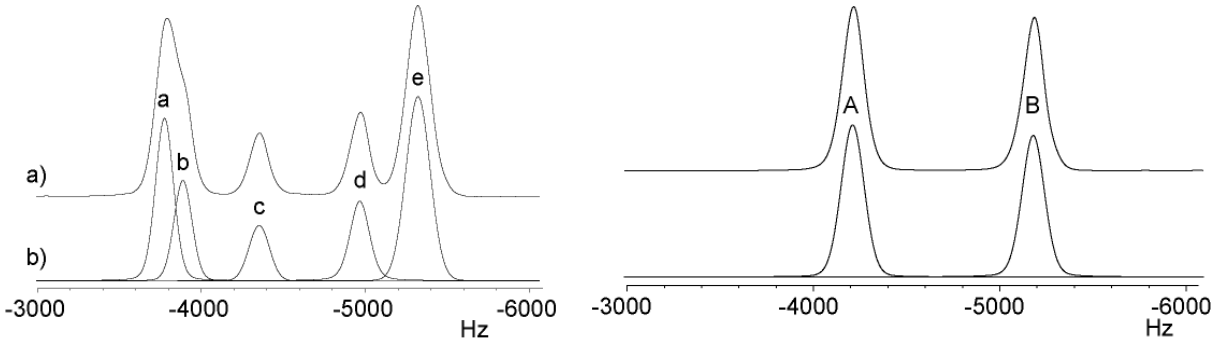


**Figure 3-4 Deconvolution of the 1D $^{31}P$ NMR spectra of $(MoO_2)_2P_2O_7$ at 0 ºC and 150 ºC**

In contrast with the X-ray experiments, simple one dimensional NMR experiments on this compound (Figure 3-5) clearly reveal the existence of a high to low symmetry transformation. The structure described by Kierkegaard in 1962 was in space group *Pnma* with two inequivalent phosphorus positions in the asymmetric unit. The NMR pattern observed at 150 ºC presents two $^{31}P$ resonances, at -23.7 ppm and -28.5 ppm and is consistent with this proposed structure being present at high temperature. At 0 ºC, the NMR pattern is more complex and can be divided into four main regions: one intense and broad signal with a shoulder at -21.2 ppm (peaks a and b), two peaks with smaller intensity at -23.9 (c) and -27.0 (d) ppm respectively and a fourth signal at -28.8 ppm (e) with similar intensity to the one at -21.2 ppm.

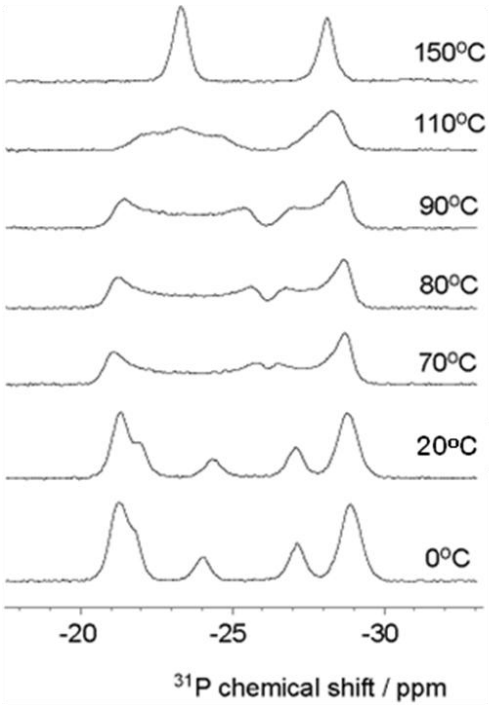


**Figure 3-5 1D spectra of $(MoO_2)_2P_2O_7$ recorded at a spinning speed of 5 kHz. The temperature shown on the spectra are the ones displayed on the temperature controller. The actual temperatures experienced by the sample are about 5°C above the reported temperatures at this spinning speed. Four acquisitions were recorded for each spectra and a pulse delay of 1024 s used to allow the system to relax fully**

Figure 3-5 also shows that between these temperature regimes we observe a broadening of the $^{31}P$ peaks. This observation suggests a large distribution of $^{31}P$ chemical shift values. In this intermediate

temperature range (from 50 °C to 130 °C) the system must therefore have a large range of different chemical environments. The observation of Bragg peaks in this temperature range rules out the possibility of this phase being amorphous.

The low temperature superstructure is challenging to observe from X-ray data due to the weak intensities of the extra peaks but the high sensitivity of SSNMR to very subtle local distortions is clearly revealed in Figure 3-5. Our NMR data confirm the existence of a low temperature phase derived from the *Pnma* structure. The intensity ratios (within experimental error) would be consistent with the presence of four ($P2_1/c$) or eight ($P\bar{1}$) $P_2O_7$ groups. The 3:1:1:3 ratio is consistent with three chemically similar groups giving rise to signals a,b and e and one different giving rise to c and d. We will show this is consistent with diffraction data.

## 3.2. CASTEP calculations

The high temperature unit cell of $(MoO_2)_2P_2O_7$ contains 60 atoms and we can perform CASTEP calculations of the NMR parameters for both the structures published and newer model obtained by Lister[3]. Calculations on the proposed low temperature $P2_1/c$ structure were, however, more challenging as this structure contains 240 atoms per unit cell. However, one of our calculation attempts on a earlier proposed structure (P21_c_02_xray) was successful.

For calculations on both high and low temperature structures, the calculated isotropic shieldings obtained from CASTEP calculations were “referenced” to experimental shift values. The absolute chemical shift values are obtained by reversing the sign of the shielding values. The mean of the calculated high temperature chemical shifts of the new structure was adjusted to match the mean of the high temperature experimental values. This adjustment corresponds to a shift of 294 ppm towards higher chemical shift values and was also used for referencing the low temperature calculated spectra. All the $^{31}P$ spectra were simulated with in-house simulation software[4].

### 3.2.1. High temperature structures

The refined bond lengths and bond angles from the high temperature structure reported by Lister[3] are listed in Table 3-3.

**Table 3-3 Bond lengths and bond angles of the high temperature structure refined by Lister[3] from synchrotron and neutron data. M is the central polyhedral atom, A is the first adjacent atom to M forming the M-A bond, B is the second adjacent atom forming the A-M-B bond angle.**

| M | A | M-A (Å) | B | A-M-B (°) | B | A-M-B (°) |
|---|---|---|---|---|---|---|
| Mo1 | O2 (P2) | 1.9716(38) | O4 | 82.41(11) | O2 | 155.59(24) |
| | | | O6 | 79.07(12) | | |
| | O2 (P2) | 1.9716(38) | O7 | 99.78(12) | | |
| | | | O9 | 95.08(11) | | |
| | O4 (P1) | 2.1482(61) | O6 | 77.59(22) | 09 | 166.08(26) |
| | O6 (Mo2) | 2.2717(55) | O9 | 88.49(24) | 07 | 169.75(25) |
| | O7(Mo2) | 1.6930(59) | O9 | 101.77(29) | | |
| | O9 (free) | 1.6565(56) | | | | |
| Mo2 | O1 (P1) | 1.9603(38) | O3 | 83.90(12) | O1 | 161.96(26) |
| | | | O6 | 93.45(12) | | |
| | O1 (P1) | 1.9603(38) | O7 | 82.06(12) | | |
| | | | O8 | 97.42(12) | | |
| | O3 (P2) | 2.0689(68) | O7 | 75.50(22) | O6 | 159.89(26) |
| | O6 (Mo1) | 1.7043(55) | O7 | 84.39(23) | | |
| | O7 (Mo1) | 2.4827(59) | | | O8 | 173.59(28) |
| | O8 (free) | 1.6737(66) | O3 | 98.09(30) | | |
| P1 | O1 (Mo1) | 1.5022(42) | O5 | 104.81(26) | | |
| | O1 (Mo1) | 1.5022(42) | O1 | 108.20(38) | | |
| | O4 (Mo1) | 1.4524(69) | O1 | 113.63(24) | | |
| | O5 (P2) | 1.5466(77) | O4 | 111.03(40) | | |
| P2 | O2 (Mo2) | 1.5004(41) | O5 | 104.33(25) | | |
| | O2 (Mo2) | 1.5004(41) | O2 | 109.57(37) | | |
| | O3 (P2) | 1.5061(72) | O2 | 115.40(23) | | |
| | O5 (Mo1) | 1.5892(75) | O3 | 106.52(41) | | |

Comparing the data given in Table 3-1 and Table 3-3, we can notice significant differences between the two structures. Mo-O and P-O distances were respectively under and over estimated by Kierkegaard while looking exclusively at X-ray data. Moreover, looking at the bond distances and bond angles in Tables 3-1 and 3-3, the $PO_4$ and $Mo_6$ polyhedra units appear to be slightly less distorted in the new structural model. Most importantly for our following studies, the P1-O5-P2 angle is significantly different from one structure to the other, Kierkegaard reporting an angle of 140.9 ° while Lister's refinement gave a value of 150.2 °.

The simulated NMR spectra for the two high temperature structures (Kierkegaard and Lister) are shown in Figure 3-6. For both structures, our calculations seem to overestimate the chemical shift spacing between the two $^{31}P$ sites and a difference in absolute chemical shift is also apparent but these aspects were not investigated in our studies. Looking at our calculations we assigned the two

$^{31}P$ resonances to the two phosphorus described in the *Pnma* structure as shown in Figure 3-6. Interestingly we can also notice that the chemical shifts order of P1 and P2 are reversed between the Kierkegaard and Lister models. As mentioned above, one of the main differences that exist between those two is the P-O-P bond angle value, which could be responsible for such a reversal.

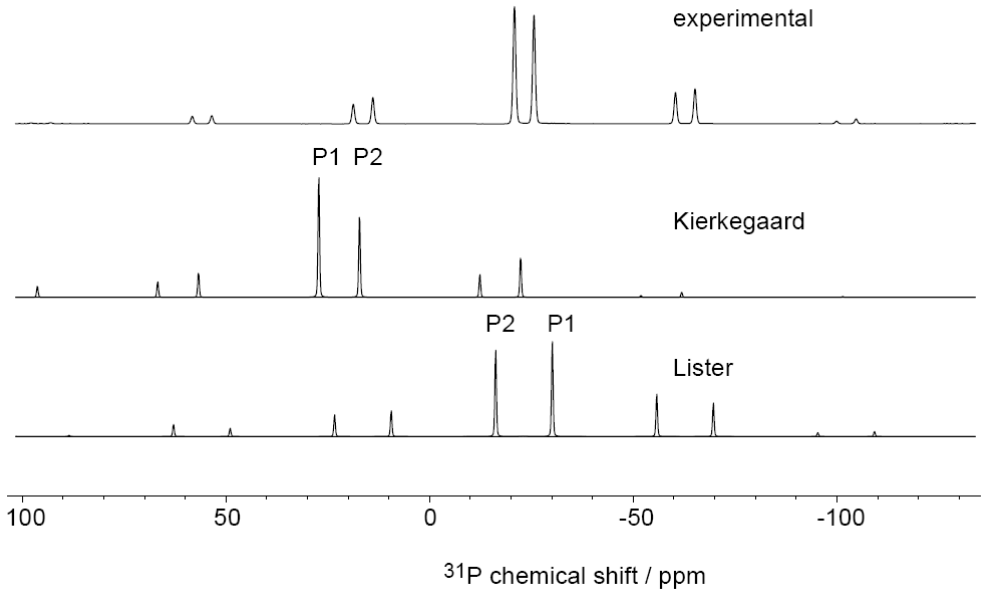


**Figure 3-6 Experimental (top) and calculated (bottom) spectra of the high temperature structure of $(MoO_2)_2P_2O_7$. The calculated spectra was obtained using the atomic coordinates reported by Kierkegaard in 1962[(1)] and Lister[(3)].**

### 3.2.2. Room temperature structure

As mentioned above (Section 3.2), DFT calculations were only performed on the $P2_1/c$ model. The simulated $^{31}P$ spectrum for the one of Lister's earlier model of $P2_1/c$ low temperature phase (from P21_c_02_xray) is presented in Figure 3-7. The calculated $^{31}P$ chemical shifts from the calculations do not exactly reproduce our experimental data. As for the high temperature phase, the chemical shift range is slightly overestimated. However, after referencing in the same way as for the high temperature case (a shift of 294 ppm), the average chemical shift values falls in the same range as the experimental values. Even if these calculations cannot fully be trusted considering the significant differences in the overall NMR pattern, it is worth noting that, as for the high temperature phase, the P2's are mainly found on the left hand side of the spectrum and the P1's are found on the right hand side. This observation is consistent with relatively subtle changes in structure at the phase transition. However, P13 and P24 only don't obey this chemical shift ordering suggesting that even these subtle changes occurring can cause an individual chemical shift "cross" from the left to the right hand region of the spectra.

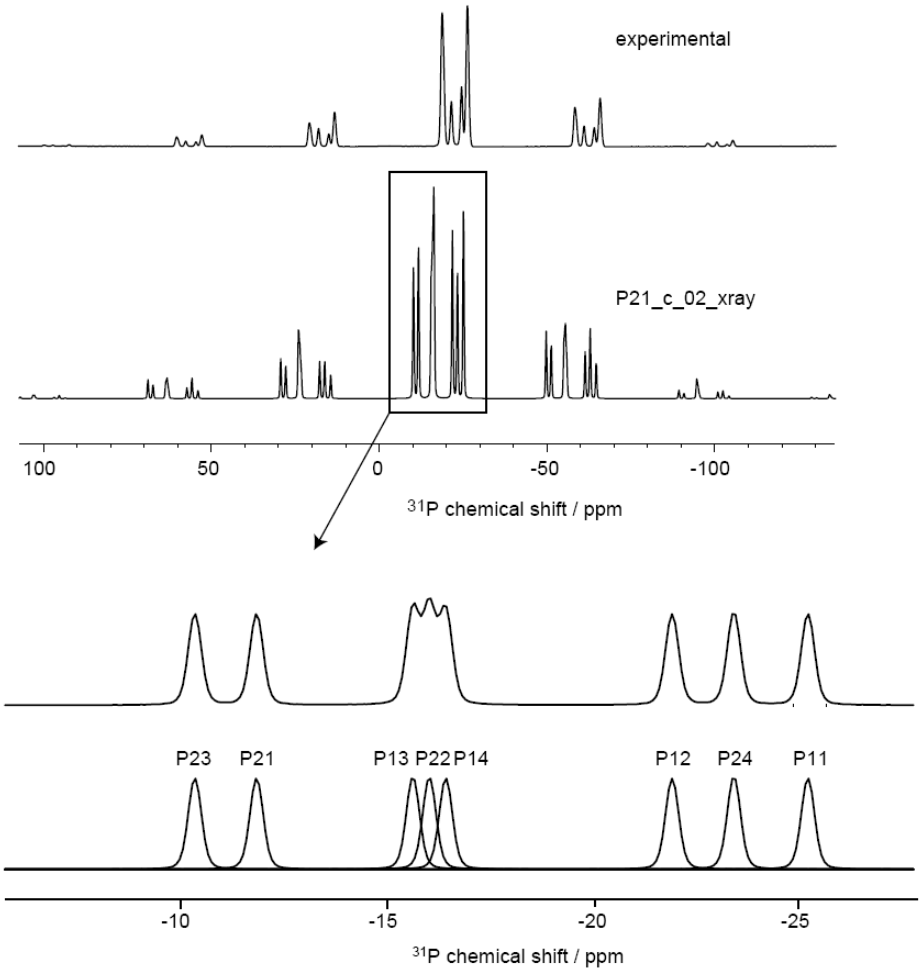


**Figure 3-7 Experimental MAS NMR pattern recorded at 0°C at 8 kHz on $(MoO_2)_2P_2O_7$ sample (SEL251) (top) and simulated spectra obtained from CASTEP calculations on $P2_1/c$ structure (P21_c_02_xray code) provided by Lister (bottom).**

In order to relate this calculated spectrum to the observations made on the high temperature structures, the P-O-P bond angles values for this $P2_1/c$ structure are reported in Table 3-4.

**Table 3-4 Bond angles values reported in the P21_c_02_xray structure**

| P-O-P angle | Bond angle values |
|---|---|
| P14-O51-P21 | 141.4° |
| P11-O52-P22 | 144.0° |
| P12-O53-P23 | 140.9° |
| P13-O54-P24 | 158.7° |

It is interesting to note here that one of the four angles is much larger than the three others. This large P-O-P angle (158.7°) is formed by the phosphorus atoms labelled P13 and P24. This larger angle therefore corresponds to the $P_2O_7$ groups whose P1/P2 signals appear in a reversed order in the calculated spectrum presented in Figure 3-7. The relative positions of two $^{31}P$ resonances belonging to the same $P_2O_7$ unit can be seen to depend, at least partially, on the value of the P-O-P angles. Our observations suggest that above a certain P-O-P bond angle value ($\theta_{inv}$), the P1 type resonances will be found at lower ppm values than the P2 type resonances. Below $\theta_{inv}$, however, this P1/P2 ordering will be reversed. In the high temperature structure, the unique P-O-P bond angle is reported at 150.2 °. If a dependence of the position as a function of the bond angle exists, then 25 % of the P1's

and P2's of the high temperature structure will move towards higher and lower chemical shift values respectively when varying from 150.2 ° to 158.7 °. The 75 % remaining $^{31}P$ sites will show the opposite behaviour. This dependence of chemical shift on P-O-P angle could also explain the $^{31}P$ NMR behaviour observed in the intermediate phase spectra shown in Figure 3-5 between 70 °C and 110 °C.

### 3.2.3. Dependence of $^{31}P$ chemical shifts on P-O-P angle

The above observations suggest that variations in P-O-P angles of the order of magnitude that occur at the low to high symmetry phase transition can have a dramatic effect on the $^{31}P$ chemical shifts. This may be the origin of the range of resonances observed for the intermediate phase between 70 °C and 110 °C in Figure 3-5. To investigate whether changes in P-O-P angles alone can cause this effect, we have used distance least squares (DLS) methods to simulate a series of structures in which the geometries (based on high temperature structure obtained by Sarah Lister) of the surrounding polyhedra were constrained to ideal geometries while the value of the P-O-P bond angle was varied (input files are listed in appendix). In these model structures, the P-O-P angles were set to 130°, 140°, 150°, 170° and their NMR parameters were calculated. Simulated powder patterns show that the DLS structures are closely related for all the different bond angles and the calculated NMR patterns are shown in Figure 3-8.

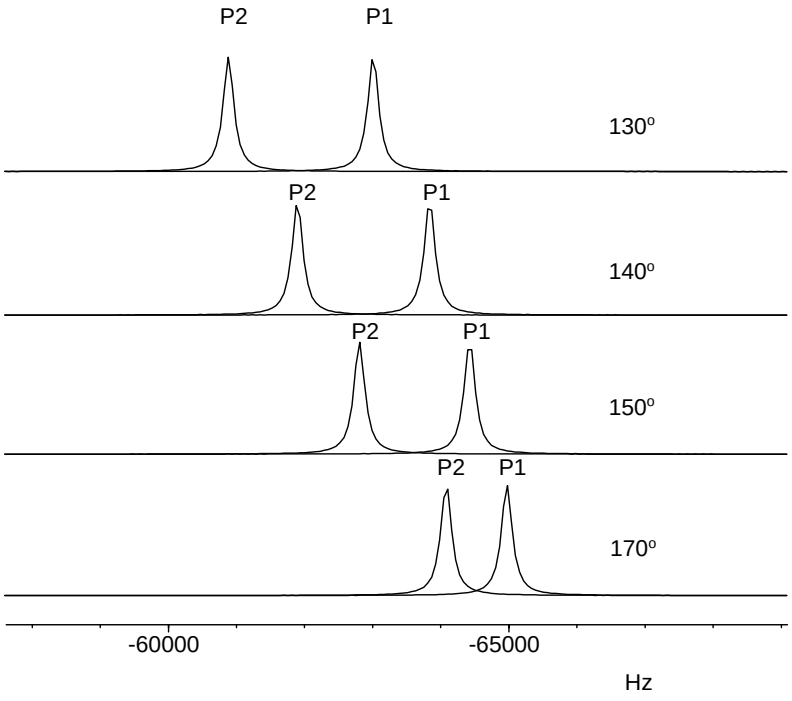


**Figure 3-8 Calculated spectra of the derived DLS model structures with varying the P-O-P bond angles.**

Figure 3-8 shows that in this simple model the P1/P2 chemical shifts orders is not reversed but does tend towards such a reversal. Indeed, we note that increasing this angle leads a decrease in the chemical shift separation. Such angle variations are expected to also involve significant distortions of the surrounding ($MoO_6$) polyhedra not fully taken into account in our model. These additional local

changes might therefore amplify this effect and induce the crossing at smaller bond angles. Further calculations would be required to confirm this.

## 3.3. J-coupling investigations

The Karplus equation is well known and well explained in liquid state NMR to connect the value of the dihedral angles to the $^3J$ coupling constants. A similar relationship which would involve the variation of the $^2J$ coupling as a function of the P-O-P bond angle values could be expected. J-coupling can be extracted from NMR data using the spin echo sequence as described in Chapter 1. Measuring the J-couplings of the different $^{31}P$ sites by spin-echo could then bring complementary information for understanding the distribution of the different $^{31}P$ resonances. Using CASTEP calculations to compute J-couplings and compare them to the experimental results is at its very early stage[(5)] and no such calculation has been done on our systems. However, J-coupling calculations on simple gas phase analogues using Gaussian is possible.

### 3.3.1. Computational studies using Gaussian calculations

Calculations were performed by Mark Fox at Durham University on $P_2O_7^{4-}$ groups in which the P-O-P bond angles were varied for both eclipsed (Figure 3-9a) and staggered (Figure 3-9b) configurations. The staggered configuration is the preferred orientation that the isolated group would adopt. The eclipsed configuration was modelled in order to reproduce the configuration present in the $(MoO_2)_2P_2O_7$ high and low temperature structures.

The model geometries of the $P_2O_7^{4-}$ anions were constructed by fixing the terminal P-O bonds to 1.500 Å and the bridging P-O bonds to 1.583 Å. The O-P-O angles involving the terminal $PO_3$ groups were fixed at 112° whereas the O-P-O(-P) angles were fixed at 107°. One oxygen atom from each $PO_3$ group was coplanar with the P-O-P bridge and away from the bridging O atom. Model geometries with P-O-P angles at 5° intervals between 100° and 180° were used to compute the *J*(PP) coupling constants at the B3LYP/6-31G*[(6-9)] level of theory with the Gaussian 03 package[(10)].

a) b)

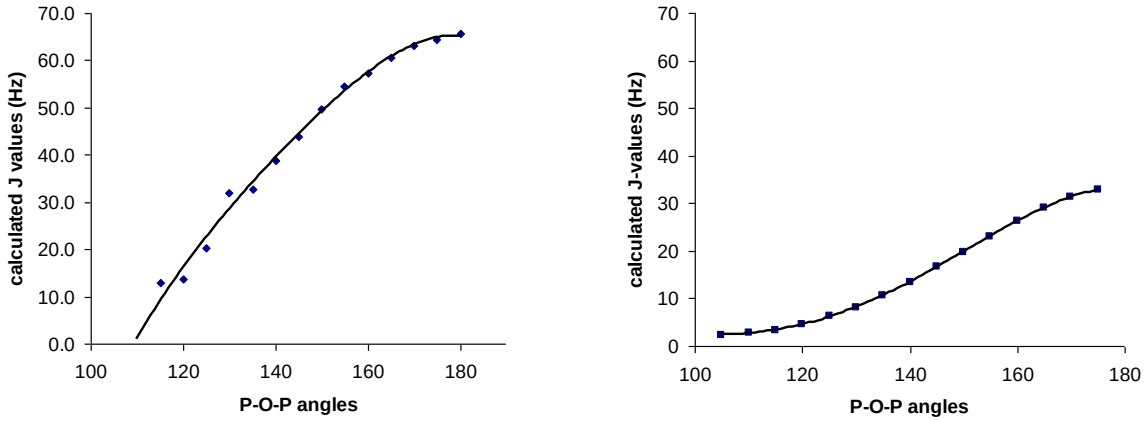


**Figure 3-9 Evolution of the J-coupling constant as a function of the P-O-P bond angle in a a) eclipsed and b) staggered configuration of the $P_2O_7^{4-}$ unit calculated using Gaussian 03 by Mark Fox.**

Although those calculations were performed on small isolated groups and can not reveal the reality of what occurs in our system, an increase of the J-coupling values with the P-O-P bond angles values clearly occurs. Such results encouraged us to probe the different bond angles values present in our $(MoO_2)_2P_2O_7$ structures via J-coupling experiments.

### 3.3.2. Spin-echo experiments

The ab-initio calculations mentioned above show a relationship between the P-O-P bond angle and the $^{31}P$-$^{31}P$ J-coupling values. The J-coupling can therefore be used to give information on the values of P-O-P angles in each material. A straightforward way of measuring J-coupling is to use a simple spin-echo experiment. This has been performed on sample SEL251 at 150ºC and the evolution of the intensity of each spectral line is plotted as a function of the $\tau$ period (Figure 3-10). As mentioned in Chapter 1, the spin-echo signal intensities as a function of the $\tau$ delay can be fitted using the following equation:

$$I(2\tau) = I(0) \times \cos(2\pi J\tau) \times \exp\left(\frac{-2\tau}{T_2'}\right)$$

Where $2\tau$ is the spin-echo time, $T_2'$ the spin-spin (transversal) relaxation time and $J$ the scalar coupling constant between $^{31}P$ sites.

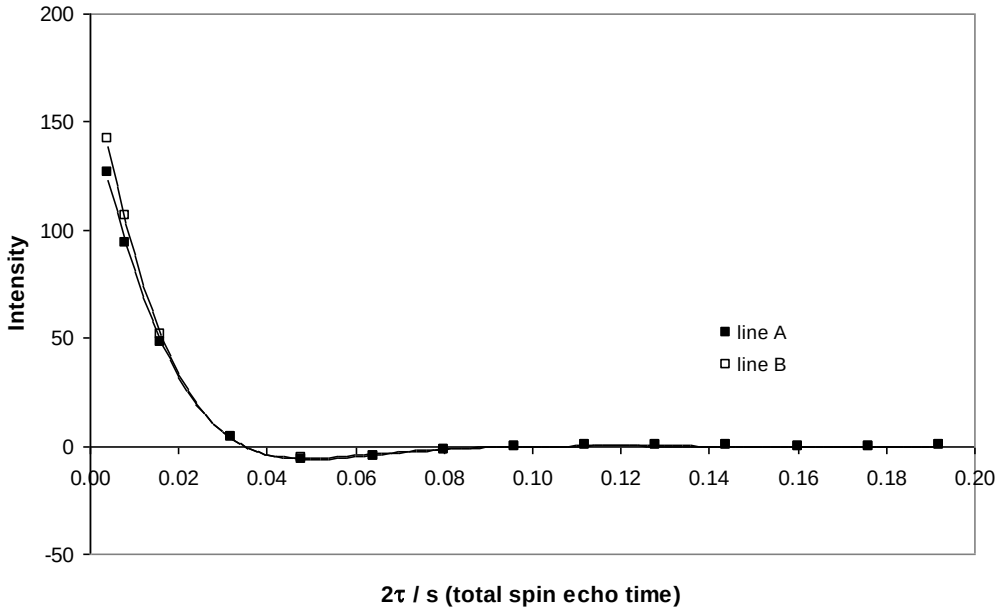


**Figure 3-10 Evolution of the spin-echo signal of the different $^{31}P$ signals in $(MoO_2)_2P_2O_7$ (SEL251). The sample was spun at 8 kHz in a 5 mm probe at 150°C. The full and blank squares represent the data points for the P1 and P2 sites respectively. The lines represent the fit to the spin echo signal decay.**

The fit parameters for these data are shown in Table 3-5. The identical J-coupling values extracted are consistent with the fact that the two phosphorus atoms belong to a common $P_2O_7$ unit (i.e $J_{P1P2}=J_{P2P1}$).

**Table 3-5 $^{31}P$-$^{31}P$ J-coupling, $T_2$' and linewidth values resulting from the fitting of the Figure 3-10 evolution curves. The homogeneous linewidth is determined from the $T_2$' value. The linewidths obtained experimentally with a single pulse experiment are also presented.**

| | Line A | Line B |
|---|---|---|
| J (Hz) | 14.60 | 14.60 |
| $T_2$'(ms) | 33 | 36 |
| Linewidth (Hz) | 9.65 | 8.84 |
| Experimental linewidth (Hz) | 140 | 140 |

As the J-coupling between two phosphorus sites within a $P_2O_7$ unit is likely to be influenced by the P-O-P bond angle (see section 3.3.1), it is interesting to keep in mind that the P1-O-P2 bond angle in Sarah Lister's high temperature structure is 150.2º. Similar J-coupling measurements on $(MoO_2)_2P_2O_7$ at low temperature will be performed and compared to the predicted bond angles distribution in proposed model structures.

The $T_2$' values have relatively similar magnitude suggesting that the chemical environments of the two sites are very similar. More interestingly, the linewidth measured experimentally (due to both homogeneous and inhomogeneous contributions) is significantly larger than the homogeneous linewidth measured by the spin-echo experiment. This inhomogeneity suggests a distribution of

slightly different chemical environments for the $^{31}P$ sites (slightly different bond angles or bond distances around the sites) .

The spin-echo experiment was also performed at 20ºC using the same acquisition parameters as for the high temperature structure and J-coupling values extracted for the five distinct NMR resonances. The resulting oscillations are shown in Figure 3-11.

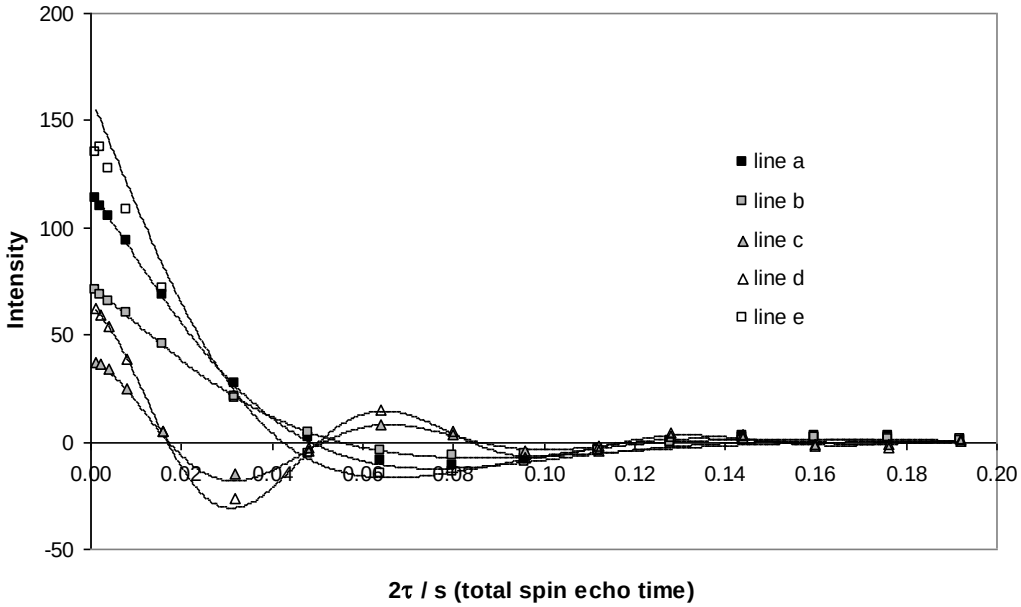


**Figure 3-11 Evolution of the spin-echo signal of the different $^{31}P$ signals in $(MoO_2)_2P_2O_7$ (SEL251). The sample was span at 8 kHz on a 5 mm probe at 20°C. The lines are fitted curves to the spin-echo signal.**

By looking at these plots, it is already obvious that lines c and d on one hand and lines a, b and e (see Figure 3-4 for labels) on the other hand show similar behaviours. This observation would already imply that sites c and d belong to the same $P_2O_7$ pyrophosphate group. The results of the curve fitting are shown in Table 3-6.

**Table 3-6 J-coupling values between the $^{31}P$ sites belonging to the same pyrophosphate unit determine by fitting the data obtained by spin-echo experiment. The linewidths obtained experimentally with a single pulse experiment are also presented.**

| | Line a | Line b | Line c | Line d | Line e |
|---|---|---|---|---|---|
| $T_2$' (ms) | 38 | 42 | 43 | 45 | 33 |
| J (Hz) | 10.3 | 9.1 | 29.2 | 29.8 | 11.8 |
| Linewidth (Hz) | 8.3 | 7.6 | 7.4 | 7.1 | 9.6 |
| Experimental Linewidth (Hz) | 130 | 130 | 136 | 136 | 172 |

In accordance with the plots in Figure 3-11, the fitted values show that lines a,b and e present similar small J-coupling values (around 10 Hz) when lines c and d are fitted to larger J-values of approximately 29 Hz. This confirms that the sites corresponding to lines c and d are therefore likely to

belong to the same $P_2O_7$ group and the lines a, b and e to correspond to phosphorus in other $P_2O_7$ groups.

Comparable effects than the ones observed in the high temperature phase are observed on the linewidths.

In the high temperature phase, the unique P-O-P bond angle was reported to be 150.2° which corresponds to a measured 14.6 Hz J-coupling value. The GAUSSIAN calculations presented in section 3.3.1 predict an increase of the J-values as this angle increases. From the intensity ratio (~3:1:1:3) obtained from the 1D NMR data and values in Table 3-6, we can then expect that 3/4 of the $P_2O_7$ units present have P-O-P angles smaller than 150° and 1/4 larger. Two possible model structures for the room temperature phase were obtained by Lister and P-O-P bond angles are reported in Table 3-7.

**Table 3-7 P-O-P bond angles values from the two proposed $P2_1/c$ and $P\bar{1}$ structures of $(MoO_2)_2P_2O_7$ (P21c_July08_07 and Pbar1_July08_07).**

| $P2_1/c$ | | $P\bar{1}$ | |
|---|---|---|---|
| P-O-P angle | Bond angle value | P-O-P angle | Bond angle value |
| P14-O51-P21 | 144.98° | P15-O51-P21 | 140.08° |
| P11-O52-P22 | 159.77° | P16-O52-P22 | 139.94° |
| P12-O53-P23 | 136.95° | P17-O53-P23 | 134.40° |
| P13-O54-P24 | 140.16° | P18-O54-P24 | 168.96° |
| | | P12-O55-P25 | 145.20° |
| | | P11-O56-P26 | 149.75° |
| | | P14-O57-P27 | 137.62° |
| | | P13-O58-P28 | 143.25° |

The distribution of bond angles in $P2_1/c$ structure is perfectly consistent with the 3:1 ratio mentioned above. The $P\bar{1}$ structure, however, presents a wider range of P-O-P bond angles where such a distribution is no longer obvious. The bond angles for this structure present one extremely large value for the P-O-P bond angles. The other seven other values are much smaller and cover a range of bond angles from 134° and 150°. Considering our studies presented in section 3.2.3, the $^{31}P$ NMR pattern of this structure could be expected to present a large range and number of chemical shift values and not the clear 3 :1 ratio observed from by NMR. Most importantly, the fitting of the spin-echo signals obtained from lines a, b and e lead to very similar J-coupling values suggesting a relatively narrow range of P-O-P angles. From these considerations, the $P2_1/c$ structure appears to be a much better candidate for the structure of $(MoO_2)_2P_2O_7$ at room temperature. The $P\bar{1}$ structure although consistent with powder diffraction data does not match our NMR observations.

Ruling out the possibility of a $P\bar{1}$ structure we can further compare our experimental observations to the $P2_1/c$ structure. The $^{31}P$ sites forming the large and unique P11-O52-P22 angle can therefore be attributed to lines c and d showing the largest J-coupling value. The calculations presented in section 3.2.2 suggest that the $^{31}P$ large bond angle, P1 site will arise at larger chemical shift values than the P2 site. With this assumption, line c can be attributed to P11 and line d to P22.

The three other J-coupling values found to be around 10 Hz for the low temperature phase, would be correlated to three smaller angles between 136.9° and 144.9°. For such bond angles values, the P2 type sites (P21, P23 and P24) are expected to appear at higher chemical shift values than the P1 type sites (P14, P12, P13 respectively) and therefore would correspond to three overlapped resonances in the signal at 21.5 ppm (e). Similarly the three P1 type sites would correspond to overlapped resonances around 29 ppm (a).

## 3.4. 2D studies

In order to confirm our previous conclusions and further assign the resonances of the low temperature structure, 2D NMR experiments were employed.

### 3.4.1. Dipolar coupling driven experiments

Up to now, we have been mainly interested in correlating our NMR observations to the P-O-P bond angles values. We can however think that useful information could also be extracted directly from the distances between the different $^{31}P$ sites of the structure. Probing interatomic distances can be achieved in NMR by using the dipolar coupling interaction. The phosphorus atoms belonging to an individual $P_2O_7$ groups are separated by distances typically between 2.9 and 3.2 Å and should show the strongest dipolar coupling values. A representation of the network of $P_2O_7$ groups and some of the inter-$P_2O_7$ P-P distances in $(MoO_2)_2P_2O_7$ is shown in Figure 3-12.

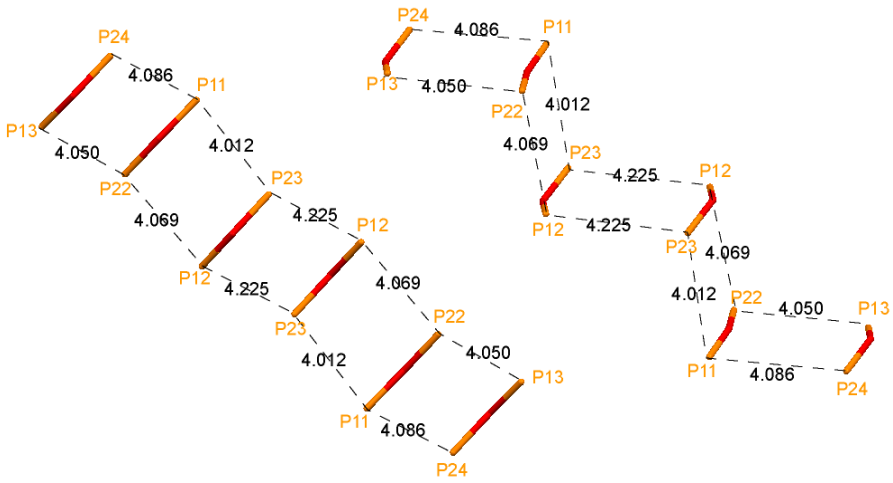


**Figure 3-12 Spatial arrangement of P1-O5-P2 related fragments in the room temperature structure of $(MoO_2)_2P_2O_7$ extracted from *P2₁/c* structure provided by Sarah Lister (P21/c_July_08_07).**

By looking at Figure 3-12, the inter-$P_2O_7$ P-P couplings arising between P1n and a P2n site are expected to be the second strongest. Given atomic positions (and therefore the inter-atomic distances), the dipolar interactions between a pair of atoms can be determined using the expression $\delta_r = -\frac{\mu_0}{2\pi}\frac{\hbar\gamma_I\gamma_S}{r^3}$ (c.f Chapter 1) where $r$ is the distance between spin $I$ and spin $S$. In a crystal, the coupling between two spins has to be considered for all different distances between the

spins concerned. The evaluation of the dipolar interaction that exists between such spins at longer range is given by:

$$d_{rss} = \sqrt{\delta_{r_1}^2 + \delta_{r_2}^2 + ... + \delta_{r_i}^2}$$

Where $\delta_{r1}$, $\delta_{r2}$… $\delta_{ri}$ are the dipolar couplings when spins $I$ and $S$ at distances of $r_1$, $r_2$,... $r_i$.

An evaluation of the 36 different dipolar interaction strengths can be made using simulation software. In order to take into account long range P-P interactions for phosphorus sites close to the edge of a unit cell, a supercell has to be generated. In this work, we generated a 5x5x5 unit cell based on the low temperature structure. The calculated dipolar couplings for this supercell are reported in Table 3-8.

**Table 3-8 P-P dipolar coupling (in Hz) existing between the eight $^{31}$P sites in the low temperature *P2$_1$/c* model structure provided by Sarah Lister (P21c_July08_07). The highlighted boxes indicate the dipolar coupling values calculated for pairs of $^{31}$P sites belonging to an individual $P_2O_7$ group.**

| | P11 | P12 | P13 | P14 | P21 | P22 | P23 | P24 |
|---|---|---|---|---|---|---|---|---|
| P11 | 65.6 | 187.6 | 190.4 | 145.8 | 189.9 | **673.7** | **317.3** | **304.7** |
| P12 | 187.5 | 184.1 | 146.0 | 64.3 | 71.3 | **347.7** | **824.9** | 110.6 |
| P13 | 190.5 | 145.9 | 65.5 | 183.5 | **296.3** | **313.0** | 183.6 | **771.5** |
| P14 | 145.8 | 64.3 | 183.5 | 184.1 | **776.6** | 108.2 | 71.9 | **335.6** |
| P21 | 189.9 | 71.3 | **296.5** | **776.6** | 159.4 | 121.7 | 77.6 | 202.7 |
| P22 | **674.1** | **347.7** | **312.9** | 108.2 | 121.7 | 80.1 | 203.1 | 172.6 |
| P23 | **317.1** | **824.9** | 183.5 | 71.9 | 77.6 | 203.1 | 169.8 | 126.0 |
| P24 | **304.6** | 110.6 | **771.5** | **335.5** | 202.7 | 172.6 | 126.0 | 77.5 |

The values reported in this table are naturally consistent with what is expected from the structural picture in Figure 3-12. Considering the significant differences in dipolar coupling values seen, a two dimensional dipolar experiment could help $^{31}$P chemical shift behaviour studies and help assignment of the different $^{31}$P resonances.

SQ-DQ experiments using the POST-C7 sequence to reintroduce and observe dipolar coupling (see Chapter 1) were therefore performed at room temperature on $(MoO_2)_2P_2O_7$ allowing the dipolar couplings to evolve over different time durations ($\tau_{exc}$). The 2D spectra recorded with $\tau_{exc}$ of 0.143 ms and 0.358 ms are presented in Figure 3-13.

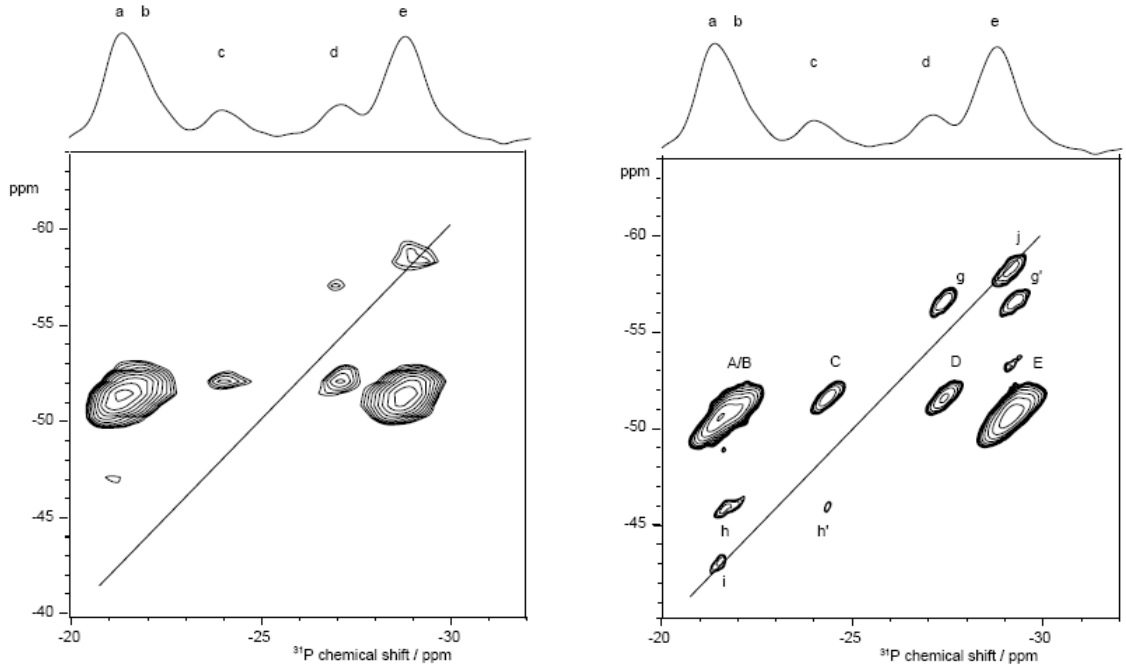


**Figure 3-13 2D POST-C7 experiment with a mixing time of 0.143 ms and 0.358 ms.**

As discussed in Chapter 1, a pair of peaks arising at the same horizontal level across the diagonal reveals dipolar coupling correlation between two sites. At short mixing times (0.143 ms), four strong correlation signals are observed due to strong phosphorus dipolar coupling (A/B, C, D and E). The correlation between resonances a/b and resonance e are shown by the A/B and E peaks lying across the diagonal. In a similar way, resonance c is correlated with resonance d leading to the apparition of peaks C and D. Considering the values presented in Table 3-8, these pairs of resonances correspond to $^{31}P$ belonging to a common $P_2O_7$ group. These observations are consistent with our 1D J-coupling experiments and conclusions.

We can also try to predict the behaviour of the signals arising from dipolar coupling in the case of a P1/P2 chemical shift order reversal with the bond angle as mentioned above. To start our argument, we use the conclusions from Section 3.3.2 and assign resonances c and d to the P11 and P22 sites from the Lister $P2_1/c$ structure. Figure 3-13 shows that at 0.358 ms, two new peaks arise on the SQ/DQ diagonal (i and j) and two new pairs of correlation peaks arise across the diagonal (pairs h/h' and g/g'). The two diagonal peaks (I and j) at chemical shift corresponding to a/b and e can be explained by the contribution of three dipolar coupling at those frequencies rather than a single P-P dipolar contribution. i.e the sum of all dipolar couplings between the three $^{31}P$ sites in each of a/b and e to all other related phosphorus leads to a significant signal.

The off diagonal peaks h/h' and g/g' can help assign a/b and e individual $^{31}P$ sites. The $d_{rss}$ values reported in Table 3-8 suggest that the first inter-$P_2O_7$ correlation peaks for P11 (resonance c) should arise with a P2 type (P23 or P24) phosphorus. Similarly, P22 (resonance d) is expected to show (slightly stronger) correlation with P12 and P13. The observation of the pair of peaks labelled h/h'

therefore means that if resonance c corresponds to a P1n site, then the three resonances a are due to P2n type (P23/P24) sites. Similarly, the pair of peaks labelled g/g', mean that P22 (resonance d) has strong dipolar coupling to peak e and these must be P1n (P12/P13) type sites. Moreover, no correlation peak is observed between resonances c and e (even at longer $\tau_{exc}$ values) suggesting that all the P1n (except P11) resonances contribute to e; such a peak would be observed at k. Similarly the lack of a peak at l means that all the P2n (except P22) resonances contribute to the a/b signal.

These observations strongly supports our conclusions made earlier on the effect of the P-O-P bond angle on the $^{31}P$ resonances.

### 3.4.2. INADEQUATE experiments

As described in Chapter 1, the 2D INADEQUATE experiment is used in solids in order to reveal homonuclear connectivities via J-coupling. In pyrophosphate systems, it has been proven to be very useful as it allows direct extraction of information about pairs of phosphorus belonging to a common $P_2O_7$ unit.

Although the INADEQUATE experiment does not seem of much interest in the high temperature structure due to its high symmetry, it was performed to allow us to benchmark experimental protocols before studying the low temperature structure and to confirm the conclusions from 1D studies.

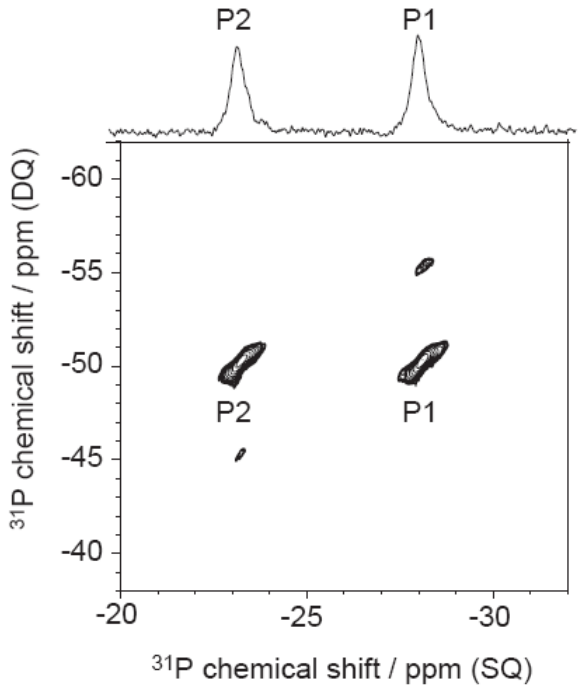


**Figure 3-14 2D INADEQUATE experiment of $(MoO_2)_2P_2O_7$ (SEL251) recorded by setting the temperature controller at 150 ºC and spinning the sample at 15 kHz. The assignment of the different resonances has been made using the CASTEP calculation results presented in section 5.2.1.**

The spectrum in Figure 3-14 shows two peaks across the SQ-DQ diagonal confirming that the two $^{31}P$ sites are interacting via J-coupling. Figure 3-14 also shows a potential assignment for the P1 and P2

sites based on the results of the DFT calculations presented in section 3.2.1 on Lister's high temperature structure.

To investigate the low temperature structure, the 2D INADEQUATE experiment was run on SEL251 sample at 0 °C using the same conditions as for the high temperature structure and is presented in Figure 3-15. This two dimensional correlation spectrum reveal the connectivities within the different $P_2O_7$ units.

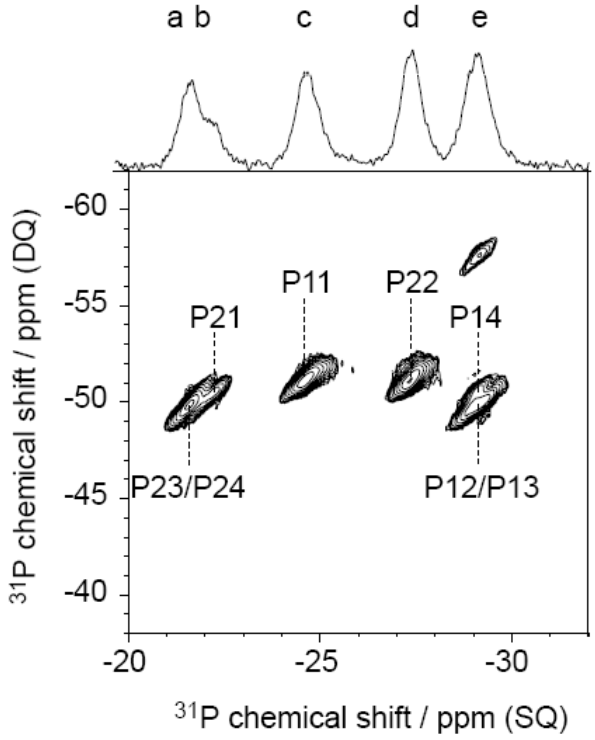


**Figure 3-15 2D INADEQUATE experiment of $(MoO_2)_2P_2O_7$ (SEL251) recorded with setting the temperature controller at 0 ºC and spinning the sample at 15 kHz.**

Two sets of correlation peaks appear across the diagonal. One involves correlation between resonances a/b and e and the other between resonances c and d. This observation implies that for a P1 type chemical shift greater than -26 ppm, the resonance of its connected P2 type site would be found at values below -26 ppm. The same statement is naturally also true for a P2 type sites and their connected P1's. This new observations combined with the results presented in previous sections can be used to assign our different NMR resonances to the phosphorus sites described in the proposed structure.

In section 5.3.2 we already justified the assignment of resonances c and d to P11 and P22 respectively based on the behaviour of these resonances under J-coupling and calculations presented in section 5.2.2. The three remaining pairs of P1's and P2's are not resolved enough to enable further unambiguous assignment. However, based on calculations from 3.2.2 and the dipolar coupling experiments, the relative P1/P2 order can be assumed.

The slight resolution between resonances a and b can be used to attempt further assignment. Looking back at Figure 3-5, we can notice that resonance b tends to merge into resonance a as the temperature is lowered from 40°C to 0°C. For "small" P-O-P bond angles (i.e. below $\theta_{inv}$ described in section 3.2.2), we expect the difference in frequencies between a P1 and a P2 resonance to decrease as the angle value increases (section 3.2.3). Therefore, out of the three remaining unassigned $P_2O_7$ groups, the one containing the $^{31}P$ site at resonance b should present the larger P-O-P bond angle value. Based on these assumptions and the bond angle values given in Table 3-7, resonance b can tentatively be assigned to P21 and its connected P1 type atom to P14.

The proposed unique assignment for the four out of eight $^{31}P$ sites of the $P2_1/c$ room temperature structure of $(MoO_2)_2P_2O_7$ is shown in Figure 3-15.

In both 2D INADEQUATE experiments (high and low temperature), weak intensity peaks due to remaining dipolar coupling appear on the diagonal. More details on the origin of such peaks are discussed in Chapter 1 but are not of interest for our current studies. The intensities of these peaks were found to decrease and disappear as the sample was spun at higher (10 kHz and 15 kHz) spinning speeds.

## 3.5. Conclusions

The structural changes occurring in $(MoO_2)_2P_2O_7$ between room temperature and 150°C were investigated. Studies by Sarah Lister clearly showed the existence of two phase transitions over this range of temperature involving crystalline structures. From these studies, an improved model of the high temperature phase structure was reported and two possible low temperature structures were proposed. Although one of the low temperature model was preferred from diffraction studies, some ambiguities remained.

By looking at 1D NMR data, the appearance of a superstructure at low temperature is obvious. The high temperature structure shows two distinct $^{31}P$ resonances while the low temperature structure $^{31}P$ spectrum can be divided into five sets of resonances with relative intensities of ratio 2:1:1:1:3 distributed around the two high temperature resonances revealing the decrease of symmetry. This high to low symmetry transition passes through a highly disordered structure where the distribution of $^{31}P$ chemical shift is broad.

CASTEP calculations were performed on high and low temperature reported structures allowing the assignment of the P1 and P2 resonances in the high temperature structure. Looking at the calculations and the reported structures, the order of the P1/P2 chemical shifts seems to be related to the value of the P-O-P bond angle.

Complementary DFT calculations were performed on model structures where only the P-O-P bond angles were varied. Although, the clear order reversal of the P1 and P2 resonances is not reproduced in our simple model, the data do show a decrease of the chemical shift difference between the P2 and P1 resonances when the P-O-P angle is increased.

In order to better understand the $^{31}P$ distribution, investigations using J-couplings were performed. Ab-initio calculations were performed to relate the J-coupling values to the P-O-P bond angles and show an increase of the coupling with the bond angle.
In the low temperature phase, two of the eight resonances present a J-coupling value significantly larger than the one found in the high temperature phase and have been assigned to the pair of phosphorus forming the $P_2O_7$ unit with the largest bond angle. The three remaining resonances present comparable J-coupling values which are smaller than that existing in the high temperature phase. The comparison of these J-coupling values to the bond angle distributions in both $P2_1/n$ and $P\bar{1}$ structural models supports the $P2_1/c$ space group as the one existing at low temperature.

The dipolar experiments on the low temperature phase confirm the P1/P2 order reversal as a function of the P-O-P angle.

The INADEQUATE experiments show the expected correlation peaks and confirm the assumptions that were made on the assignment of the distribution of the $P_2O_7$ groups by spin-echo experiments.

The combination of the different experimental (powder diffraction, $^{31}P$ NMR) and theoretical (GAUSSIAN and DFT calculations) studies presented here not only allow us to successfully determine the structure of $(MoO_2)_2P_2O_7$ at low temperature but an assignment of the different $^{31}P$ resonances was proposed. New features regarding the potential influence of the P-O-P bond angles on both chemical shifts and J-coupling values in pyrophosphates were also presented.

## 3.6. References


1. P. Kierkegaard, *Arkiv for Kemi* **19**, 1-& (1962).
2. I. Schulz, *Zeitschrift Fur Anorganische Und Allgemeine Chemie* **281**, 99-112 (1955).
3. S. Lister, *PhD thesis, Durham University* (2009).
4. P. Hodgkinson, *http://www.durham.ac.uk/paul.hodgkinson/pNMRsim*.
5. S. A. Joyce, J. R. Yates, C. J. Pickard, S. P. Brown, *Journal of the American Chemical Society* **130**, 12663-12670 (2008).
6. A. D. Becke, *Journal of Chemical Physics* **98**, 1372-1377 (1993).
7. C. T. Lee, W. T. Yang, R. G. Parr, *Physical Review B* **37**, 785-789 (1988).
8. G. A. Petersson, M. A. Allaham, *Journal of Chemical Physics* **94**, 6081-6090 (1991).
9. G. A. Petersson, A. Bennett, T. G. Tensfeldt, M. A. Allaham, W. A. Shirley, J. Mantzaris, *Journal of Chemical Physics* **89**, 2193-2218 (1988).

10. G. W. T. M. J. Frisch, H. B. Schlegel, G. E. Scuseria, M. A. Robb, J. R. Cheeseman, J. A. Montgomery, Jr., T. Vreven, K. N. Kudin, J. C. Burant, J. M. Millam, S. S. Iyengar, J. Tomasi, V. Barone, B. Mennucci, M. Cossi, G. Scalmani, N. Rega, G.A. Petersson, H. Nakatsuji, M. Hada, M. Ehara, K. Toyota, R. Fukuda, J. Hasegawa, M. Ishida, T. Nakajima, Y. Honda, O. Kitao, H. Nakai, M. Klene, X. Li, J. E. Knox, H. P. Hratchian, J. B. Cross, C. Adamo, J. Jaramillo, R. Gomperts, R. E. Stratmann, O. Yazyev, A. J. Austin, R. Cammi, C. Pomelli, J. W. Ochterski, P.Y. Ayala, K. Morokuma, G. A. Voth, P. Salvador, J. J. Dannenberg, V. G. Zakrzewski, S. Dapprich, A. D. Daniels, M.C. Strain, O. Farkas, D. K. Malick, A. D. Rabuck, K. Raghavachari, J. B. Foresman, J. V. Ortiz, Q. Cui, A. G. Baboul, S. Clifford, J. Cioslowski, B. B. Stefanov, G. Liu, A. Liashenko, P. Piskorz, I. Komaromi, R. L. Martin, D. J. Fox, T. Keith, M. A. Al-Laham, C. Y. Peng, A. Nanayakkara, M. Challacombe, P. M. W. Gill, B. Johnson, W. Chen, M. W. Wong, C. Gonzalez, and J. A. Pople, Gaussian, Inc., Wallingford CT, (2004).

# Chapter 4. Studies on zirconium tungstate, $ZrW_2O_8$

## 4.1. Atmospheric pressure phase: α and β-$ZrW_2O_8$

### 4.1.1. Structures

The synthesis of cubic α-$ZrW_2O_8$ by reaction of $WO_3$ and $ZrO_2$ was first reported by Graham et *al*. in 1959[1]. However, its crystal structure and the existence of negative thermal expansion from 0.3 K to its decomposition temperature at 1050 K was only described in 1996[1, 2]. X-ray and neutron diffraction experiments have shown that over this temperature range, the material adopts two related cubic structures[2]. In both cases, $ZrW_2O_8$ can be described as a network of corner-sharing $WO_4$ tetrahedra and $ZrO_6$ octahedra with two crystallographically distinct $WO_4$ tetrahedra lying on the three fold axis of the cubic unit cell.

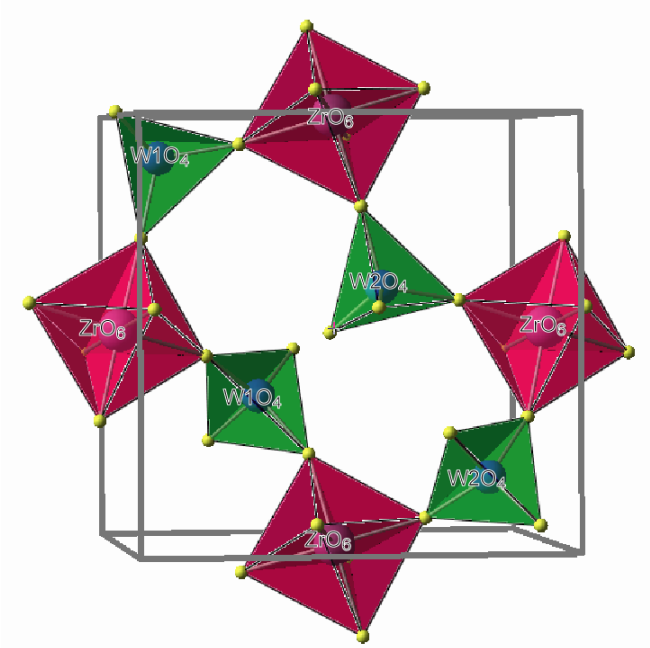


**4-1 Schematic representation of the room temperature cubic $ZrW_2O_8$ structure.**

At 450 K and below, characterisation methods show a cubic unit cell (a=9.1575 Å at 293 K) in which the two tetrahedra are ordered. This has been named the α-phase. In this structure, each $WO_4$ tetrahedron shares only three of its four oxygens with octahedra and the two adjacent tetrahedra point in the same direction along a W-O bond (Figure 4-1). This arrangement gives rise to a noncentrosymmetric space group $P2_13$. One of the two oxygens that lies on the 3-fold axis of the cube (O3) has a weak interaction with the W of the other tetrahedron (with a "bridging" length of ≈2.38 Å whereas the typical W-O bond length within a tetrahedron is around 1.8 Å). The second oxygen lying on this axis (O4) is strictly one-coordinate. It is then very mobile and induces an instability shown by a temperature dependant second order phase transition occurring at 448 K to create the so called β-phase[2].

At this temperature, some reflections in the powder pattern of the α-phase characteristic of the acentric structure ($P2_13$) disappear. The nature of this increase of symmetry was first investigated by Evans et *al.*[2, 3] suggesting that the centrosymmetry of the β-form is due to the rearrangement (flipping) of the $WO_4$ tetrahedra along the diagonal of the cube. The β-phase appears to be a disordered version of the α-phase where $WO_4$ tetrahedra pairs are randomly pointing in opposite directions leading to an average centrosymmetric structure[2]. The mechanism leading to the inversion of the $WO_4$ units (Figure 4-2) was revealed by Hampson et *al*. using X-ray diffraction data and exchange solid state NMR methods[4, 5].

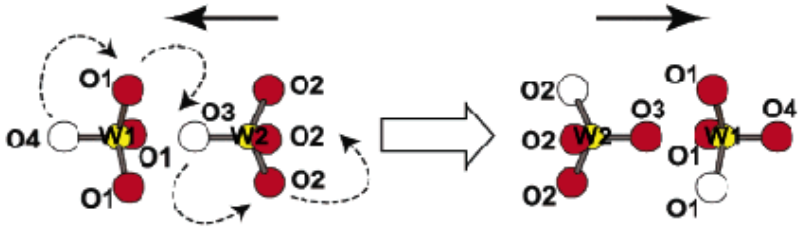


**Figure 4-2 Oxygen mobility mechanism responsible for the α to β-phase transition in cubic $ZrW_2O_8$.[5]**

The approximate upper limit of kinetic stability for the cubic $ZrW_2O_8$ phase has been determined to be 1050 K where the phase decomposes back in the two binary oxides ($WO_3$ and $ZrO_2$).

### 4.1.2. Negative Thermal Expansion mechanisms

One of the most interesting properties of the cubic form of $ZrW_2O_8$ is that it shows an isotropic negative thermal expansion (NTE) from 0.3 K up to its 1050 K decomposition temperature with a magnitude of expansion comparable to the positive expansion observed in many ceramics ($\alpha_{ZrW2O8}$ = -8.8 x $10^{-6}$ $K^{-1}$) (Figure 4-3).

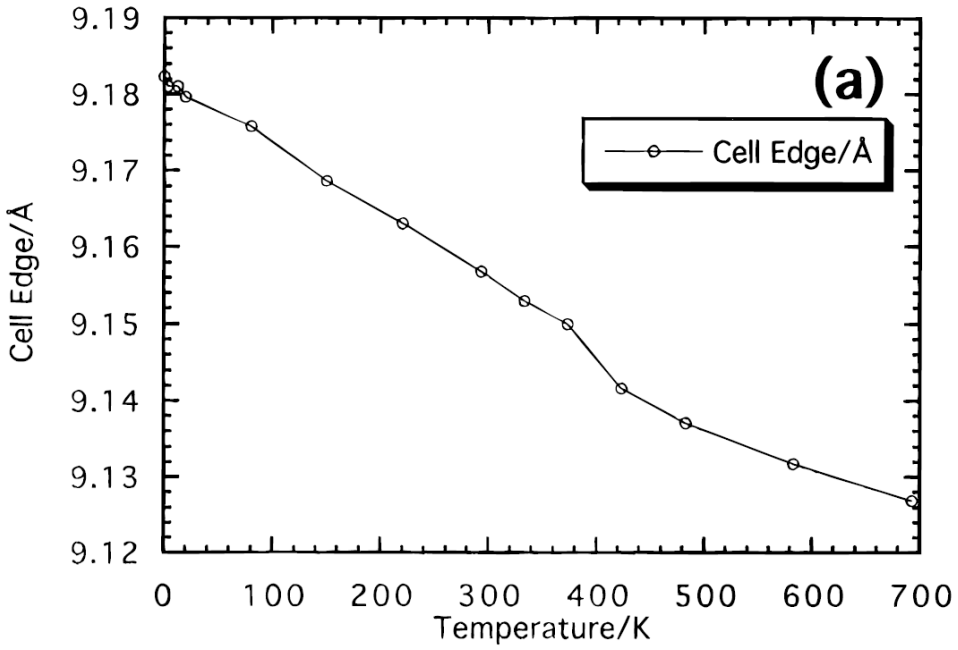


**Figure 4-3 Evolution of the cell parameter of the cubic $ZrW_2O_8$ as a function of temperature.**

Different experiments have been carried out in order to better understand this highly unusual NTE phenomenon. Neutron diffraction studies have shown that between 0.3 and 700 K, the M-O (Zr-O and W-O) distances do not change significantly and that the bonding variations are therefore unlikely to be the cause of the negative thermal expansion in the cubic phase[(2)]. Moreover, no significant distortions in the $ZrO_6$ octahedral positions occur in this range of temperature. The contraction on heating was then proposed to be due to the variation of the W-O-Zr angles with temperature. The rotation of the rigid octahedra in cubic-$ZrW_2O_8$ by increasing the temperature has first been explained by Pryde et *al.*[(6)] by the population of low energy vibrational modes and confirmed by other low temperature heat capacity and neutron scattering investigations by Ramirez, Kowach et *al*.[(7, 8)]. These particular modes where the polyhedra remain rigid are called rigid unit modes and quasi rigid unit modes (RUM's and QRUM's described in the NTE section of the work). A simple geometric model of how rigid polyhedra respond to a change in cell parameters was described by Evans et *al*.[(2)] and is shown in Figure 4-4. We can see from this picture that as the cell parameter reduces, $ZrO_6$ octahedra and $WO_4$ tetrahedra undergo coupled rotations, potentially leading to a contraction of the whole structure[(2)].

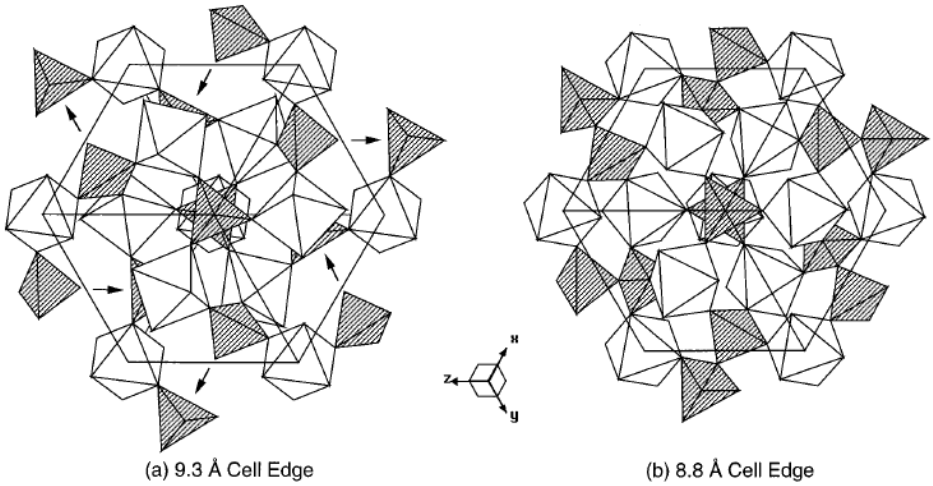


**Figure 4-4 Representation structures modeled by Evans et *al*. showing the polyhedral tilts when the varying cell edge. The figure was extracted from reference[(2)].**

However, this simplest model where the $WO_4$ tetrahedra and $ZrO_6$ octahedra are undistorted was always assumed as unrealistic. Measurements using total neutron scattering are sensitive to local structure and its deviations from the average structure. This technique combined with Monte Carlo modeling[(9)] and earlier published studies by EXAFS (Extended X-ray Absorption Fine Structure) were used to refine the RUM model[(9)]. The distributions of bond angles and bond distances at different temperatures were used to understand the movements of the different polyhedra and their components. This analysis confirms some similarities with the RUM model. The M-O (M = W, Zr) bonds are confirmed to be relatively stiff over that temperature range, suggesting that the structural changes leading to NTE are mainly due to polyhedral movements. As the temperature varies, the $ZrO_6$ units mainly rotate while the $WO_4$ tetrahedra movements can mainly be described by translations. However, unlike in the RUM model, the two $WO_4$ tetrahedra are distorted in very different ways at

300 K. Indeed, due to the proximity of the O3 atom, $W(1)O_4$ appears highly distorted (O1-W1-O1 and O4-W1-O1 of 115.9º and 101.8º respectively, O1…O1=3.078 Å and O1…O4=2.744 Å) while W(2)O4 is largely undistorted (O2-W2-O2 and O3-W2-O2 of 109.5º and 109.4º respectively, O2…O2=2.914 Å and O2…O3=2.873 Å).

As the temperature increases it was noted that the $<W1…W2>_{pair}$ distance extracted from total neutron scattering increases while the average "Rietveld" $<W1>…<W2>_{pair}$ distance stays almost constant. This observation implies that increase in the $WO_4$ units movements perpendicular to the 111 direction of the cube are likely to be accompany the $WO_4$ rotations.

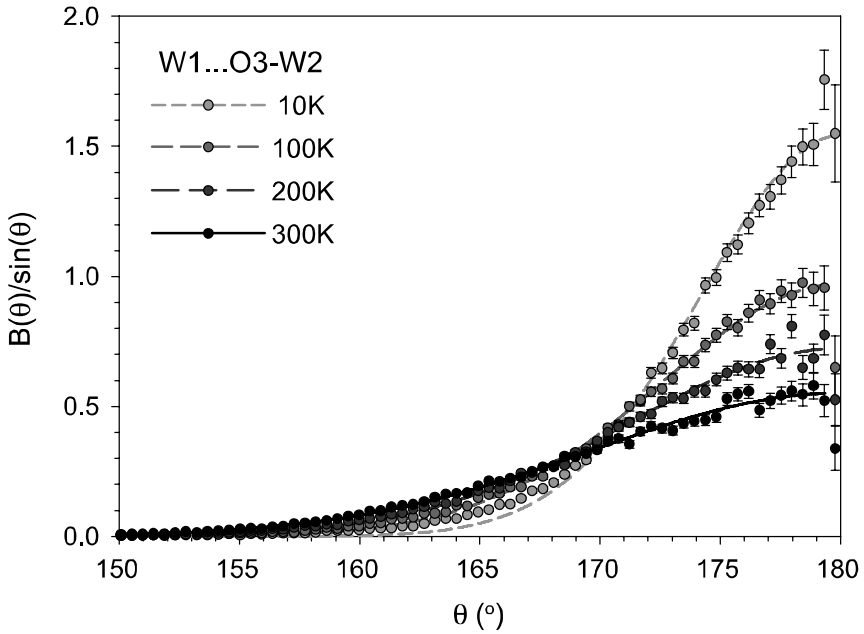


**Figure 4-5 W1-O3-W2 bond angle distribution at different temperatures extracted from total neutron scattering studies by Tucker et *al.*[(9)].**

Therefore as the temperature increases, the W1…O3-W2 bond angle distribution remains centered at 180° but broadens at a rate of 0.015 ° / K (Figure 4-5). This implies as well a rotation of the $ZrO_6$ octahedra leading to a diminution of the W…Zr, Zr…Zr and $W1…W2_{network}$ bond lengths. These bond length diminutions compensate and overtake the positive thermal expansion expected by the broadening of the W1…O3-W2 bond angle. The increase of the $<W1…W2>_{pair}$ distance also leads to a regularisation of the $W(1)O_4$ tetrahedra that could also contribute to the negative thermal expansion.

## 4.2. Pressure induced orthorhombic γ-phase

### 4.2.1. Structure

While investigating the flexibility of the α-phase, Evans and al.[(10, 11)] found that the cubic structure becomes unstable at relatively low pressures (transformation starts at 2 kbar and is fully completed at 3.2 kbar) and transforms to an orthorhombic $P2_12_12_1$ phase which is retained after pressure release. Diffraction analysis show that this high pressure form has a reduction in volume of ≈ 5 % compared to the α-phase. This structure is closely related to the original atmospheric pressure α-phase. Indeed, its

orthorhombic unit cell has two of the cell parameters very close to the $\alpha$-phase and the third is tripled compared to it (a(ortho) = 9.067 Å, c(ortho) = 8.921 Å and b(ortho) = 27.035 Å at 300 K). The structure of this orthorhombic phase can no longer be strictly described as a network of corner sharing $WO_4$ and $ZrO_6$ polyhedra as in the $\alpha$-phase. However, several analogies can be made with the cubic structure in order to better understand its structure.

One description[(10)] is that the $ZrO_6$ units are essentially identical to those in the $\alpha$-structure. However, as shown in Figure 4-6, as the pressure is applied the distance between the $WO_4$ tetrahedra is changed, leading notably to a modification of the coordination of the tungsten atoms of the original tetrahedra. Six unique $WO_n$ polyhedra forming three pairs of $WO_n$ distorted polyhedra (W(1)-W(2), W(3)-W(4), W(5)-W(6)) are present in the $\gamma$-phase instead of the two existing in the cubic structure. Their polyhedral representation is shown in Figure 4-6. For W1-W2 and W5-W6 pairs, the distances between the paired W is decreased compared to that in the cubic phase. The W3-W4 pair, however, shows a different behaviour. The distance does not significantly differ (from 4.13 to 4.10 Å), but the orientation of the pair is reversed (see Figures 6a) and 6c)).

This inversion of one of the three $W_2O_8$ units gives rise to variations in the coordination of the different W atoms in the structure. W1, W2, W4 and W6 coordination becomes 4+1, W5 becomes 5+1 (the W5-O5 bond being now considered as true bond) and W3 remaining the only strictly tetrahedrally coordinated tungsten. This rearrangement also gives rise to significant changes in bonding of all the oxygens of the structure. All the W-O-Zr bonding oxygens remain strictly two coordinate as in the $\alpha$-phase. However, the coordination of the terminal oxygens (O101, O102, O103, O104, O105 and O106) is modified, in that all achieve two coordination (W-O-W). These structural changes generate three inequivalent Zr atoms and six inequivalent W atoms for this lowered symmetry phase when only one and two respectively exist in the cubic $\alpha$-phase. The reduction of two of the three W-W distances within each pair of tetrahedra and the variation of the coordination number of the W atoms[(10)] explain the reduction of volume that occurs during the $\alpha$- to $\gamma$-phase transition.

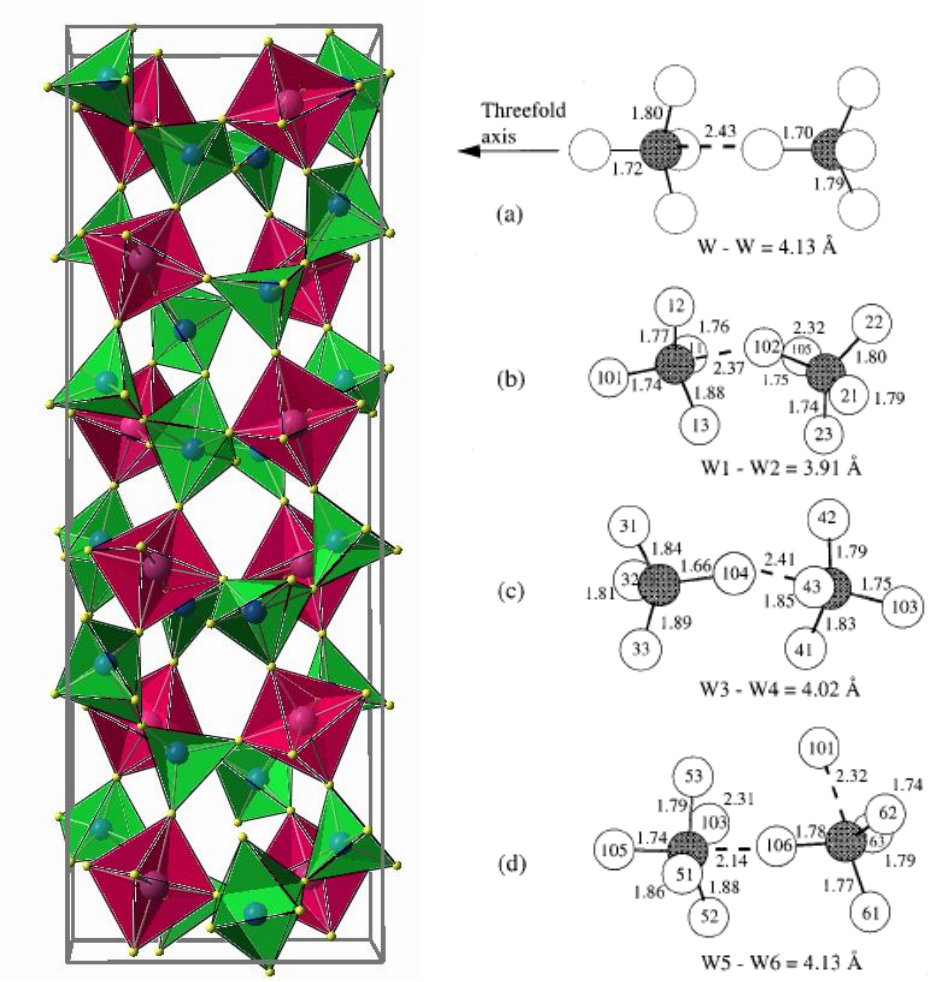


**Figure 4-6 Left. Polyhedral representation of the pressure induced γ-$ZrW_2O_8$ phase. Right. a) representation of the linear orientation of the $WO_4$ tetrahedra in α-$ZrW_2O_8$ ; b), c) and d). representation of the three different pairs of $WO_n$ polyhedra and bond lenghts in the γ-$ZrW_2O_8$ (Oxygen atoms are white and tungsten atoms are shaded).**

The modification of the relative arrangement of the $WO_n$ entities in each pair while applying pressure also has consequences on the thermal expansion properties of the material. At low temperature (up to about 225 K) its thermal expansion is also negative. Above 225 K up to its transformation back to the cubic form (390 K), its thermal expansion is positive. Unlike the α-phase, this thermal expansion is not isotropic[12, 13]. The smaller amplitude of the NTE shown by the γ-phase compared to the α-phase is due to the fact that all the oxygen sites in the structure are linked to two metal atoms unlike in the α-phase.

## 4.3. Pressure induced amorphous phase

### 4.3.1. Structure

An amorphous phase of $ZrW_2O_8$ was first been reported by Perottoni and Jordana in 1998[14] and confirmed by both X-ray diffraction and Raman spectroscopies. The gradual pressure amorphisation occurs between 1.5 and 3.5 GPa and the resulting phase has been shown to be the only one that exists at room temperature between about 2.4 and 8 GPa. The structure retains its amorphous form after the pressure is released from low temperature to up to 873 K. The amorphous phase is around

26 % denser than the $\alpha$-phase[15]. Recrystallisation to the original cubic $\alpha$-$ZrW_2O_8$ structure is achieved at an annealing temperature of 923 K[16]. Several hypotheses on the structure of amorphous $ZrW_2O_8$ have been postulated.

Pressure induced amorphisation (PIA) has been observed in several compounds to be due to high pressure decomposition of the material into a mixture of oxides. For this type of amorphisation to occur, the total volume of the daughter phases has to be smaller than the parent one. If $ZrW_2O_8$ were to decompose via the equation:

$$Zr(WO_4)_2 \rightarrow ZrO_2 + 2WO_3$$

the relatively open structure of $\gamma$-$ZrW_2O_8$ relative to $ZrO_2$ and $WO_3$ would lead to a contraction[16, 17]. Indeed this would be expected to give a reduction in volume of 26.7 % which is, within experimental error, the same as the one observed experimentally across the amorphisation.

Another possible model to describe this amorphous phase suggested an increase of the coordination of the W and/or Zr atoms within the structure. Ex-situ high pressure investigations by X-ray absorption techniques XANES and EXAFS were performed by Varga et *al.*[18]. Comparing the data from the amorphous phase and several other known compounds gave information on the coordinations of the W atoms (XANES) and the polyhedral distortions. These studies suggest that the W atoms are no longer in a tetrahedral environment but in a 5 coordinate or heavily distorted octahedral environment. It seems to reveal that the lengthening of W-O bonds and the regularisation of the coordination environment (distorted octahedra) continue when increasing the pressure until the sample becomes amorphous. However, these studies did not look at the Zr environments.

Total neutron scattering studies were performed by Keen et *al.*[15] on the amorphous form and data were refined against two constrained models using 2816 atoms generated by Monte Carlo methods. In the first model, the W environments stay similar to those existing in $\gamma$-$ZrW_2O_8$ with 4 and 5 coordinated tungstate atoms but in which the Zr atoms are 7 coordinated. In the second model, the Zr atoms are kept 6 coordinate but the W atoms are five coordinate.

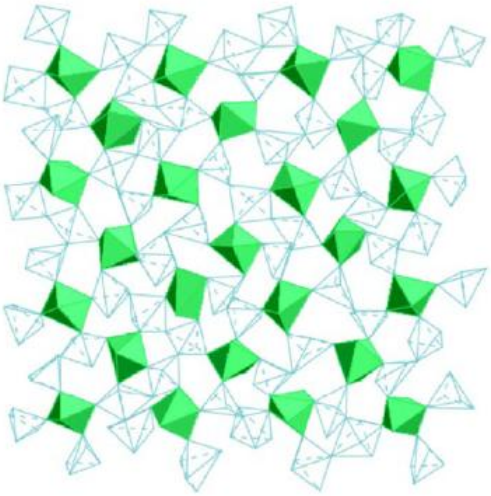

**Figure 4-7 Polyhedral representation of the amorphous $ZrW_2O_8$ phase obtained by refinement of Monte Carlo model against neutron and X-ray data. The picture is extracted from reference[15]. $ZrO_6$ and $WO_5$ polyhedra are presented in filled and unfilled green respectively.**

The neutron data were in very good agreement with the second proposed model and a section of the 2816 atoms resulting structure is presented in Figure 4-7. This model is also well in agreement with the observations reported by Varga et *al*. in their XAS studies[18].

The two extreme models for the amorphous phase are structurally very different and we might therefore think that solid state NMR could easily distinguish between them. If the amorphous material is a mixture of $WO_3$ and $ZrO_2$, then its $^{17}O$ NMR pattern should show only peaks in the region corresponding to these oxides. However, if the amorphous phase is an arrangement of Zr and W polyhedra as suggested by total neutron scattering experiments, the $^{17}O$ should show a continuous distribution of chemical shifts corresponding to the large number of different oxygen sites present and the slight structural differences between them.

In this work, $^{17}O$ enriched samples have been synthesised for each of the three $ZrW_2O_8$ phases mentioned above and investigated by $^{17}O$ MAS NMR. In our $\alpha$-phase studies, the combination of experimental results and DFT calculations can be used to confirm some of the possible NTE mechanism. DFT calculations can be performed on the $\gamma$-phase and compared to the experiment to confirm the description of the structure proposed from diffraction data. The $^{17}O$ experiments on the amorphous phase will be used to distinguish between the two PIA models described above.

## 4.4. Synthesis of $^{17}O$ enriched $ZrW_2O_8$ phases

The preparation of unenriched $ZrW_2O_8$ has been described by Graham[(1)]. Two possible synthesis routes have been reported for $^{17}O$ labelling of $ZrW_2O_8$. The first route involves enrichment of $WO_3$ and $ZrO_2$ oxide reactants. However, the synthesis of those two enriched oxide requires complicated synthetic routes and the resulting $ZrW_2O_8$ sample exhibits impurities, as described by Allen[(19)]. Another synthetic route described by Hampson[(20)] is easier and gives better yield and therefore will be employed here.

### 4.4.1. Preparation of $ZrO_2$

3.000 g of $ZrOCl_2.xH_2O$ (Alfa Aesar, white powder, puratonic 99.9985%) was ground for about 5 minutes in an agate pestle and mortar and transferred to a large platinum crucible and heated at a rate of 5 K / min to 900 °C. The sample was kept at this temperature for 6 hours and cooled down to room temperature. 1.085 g of a white powder (AS003) were recovered and the corresponding X-ray diffractogram (d9_03286) is reported in Figure 4-8.

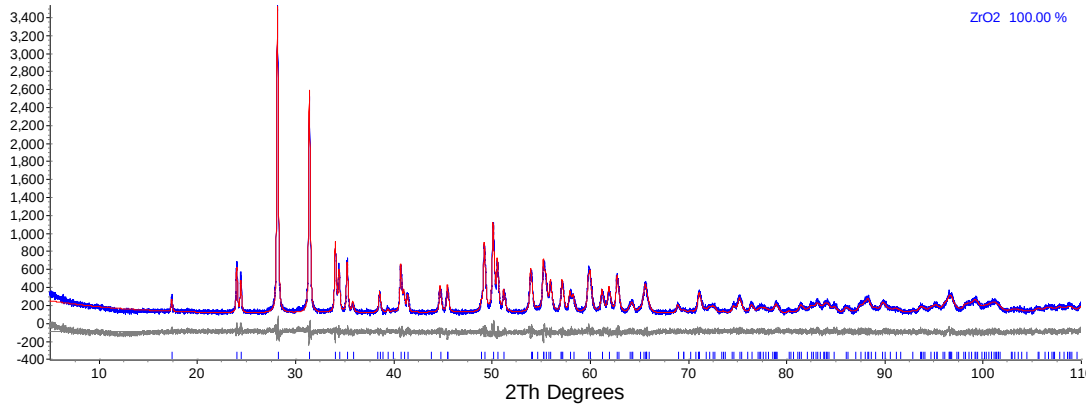


**Figure 4-8 Rietveld refinement plots of the X-ray diffraction data from the room temperature monoclinic $ZrO_2$ (d9_03286) Rwp=8.95 %.**

A total of 22 parameters were refined to fit the diffraction data and confirms the phase purity. The refined parameters included 8 global parameters (6 background parameters, 1 sample height displacement parameter, 1 axial divergence parameter) and 14 parameters to model the $ZrO_2$ phase (4 cell parameters, 3 atom positions, 3 isotropic displacement parameters and 4 parameters to define the peak shapes). The input files for this refinement and the following ones are given in the appendices and the results of the fitting are tabulated in Table 1. The good agreement shows a phase pure material. The synthesis of $\alpha$-$ZrW_2O_8$ using this starting material is described below.

### 4.4.2. Preparation of unenriched $ZrW_2O_8$

1.000 g of $ZrO_2$ (AS003) and 3.7631 g of $WO_3$ (Alfa Aesar, green powder, puratonic 99.8%) were ground in an agate pestle and mortar, transferred to a large Pt crucible and heated for 20 hours at 1175 °C. The sample was taken out of the furnace while at 1175 °C and immediate quenched in liquid

nitrogen. 4.6 g of a white powder were recovered (AS006) and the X-ray data (d9_01838) are shown in Figure 4-9.

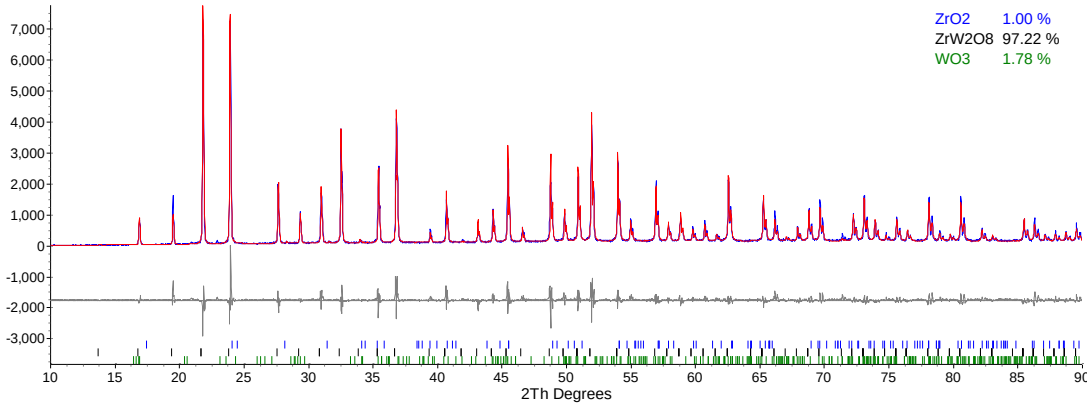


**Figure 4-9 Rietveld refinement plots of the X-ray diffraction data for room temperature $ZrW_2O_8$ (d9_01838). Rwp = 12.305%**

A total of 29 parameters were refined to fit these data. Since the proportion of $WO_3$ and $ZrO_2$ present in the sample were negligible, only the parameters describing the $ZrW_2O_8$ structure have been refined. The refined parameters included eight global parameters (6 background parameters, 1 sample height displacement parameter, 1 axial divergence parameter) and 19 parameters to model the $\alpha$-$ZrW_2O_8$ phase (1 cell parameters, 11 atom positions, 3 isotropic displacement parameters and 4 parameters to define the peak shapes). The sample is close to phase pure.

### 4.4.3. Preparation of $^{17}O$ enriched $ZrW_2O_8$

In order to perform $^{17}O$ NMR MAS experiment in a reasonable amount of time, $^{17}O$ enrichment is necessary. A synthesis where the $ZrW_2O_8$ is hydrated to a $ZrW_2O_8.xH_2O$ form using enriched water[(20)] was performed.

1.60 g of $ZrW_2O_8$ was ground using an agate mortar and pestle and transferred to an open-ended Pyrex glass ampoule. 1.62 g of 25.2 % $^{17}O$ isotopically enriched water (~33 molar excess) were added using a gas-tight syringe. The ampoule was then frozen immediately by immersion in liquid nitrogen and then evacuated and sealed.

The ampoule was placed in a 23 ml Anton Parr steel autoclave with PTFE liner. Tap water was poured around the ampoule. The steel autoclave was assembled and placed in an oven and heated from room temperature to 200°C at a rate of 10°C.min$^{-1}$ then from 200°C to 240°C at 2 °C.min$^{-1}$. The temperature was held at 240 °C for 40 hours before the sample was cooled down to room temperature. The ampoule was then taken out of autoclave and open by scoring and thermal shocking. The surface water was removed with a pipette and the open ampoule was placed in a Schlenk tube which was then evacuated and left under dynamic vacuum for 2 hours. A grey powder was obtained (AS009) and characterised by X-ray diffraction methods (d9_01958). The X-ray pattern was recorded on an aluminium plate giving five Bragg diffraction peaks at 2 theta values of 38.4°, 44.7°, 65°, 78.2° and 82.2° and is shown in Figure 4-10. The cubic Al phase was fitted by Pawley

refinement optimising the cell parameter and peak intensities. A total of 32 parameters were then refined. The refined parameters included 10 global parameters (8 background parameters, 1 sample height displacement parameter, 1 axial divergence parameter) and 12 parameters to model the $ZrW_2O_8$. $xH_2O$ phase (1 cell parameters, 5 atom positions, 2 displacement parameters (1 isotropic and 1 anisotropic) and 4 parameters to define the peak shapes). This intermediate phase was confirmed by X-ray diffraction to be $ZrW_2O_8$. $xH_2O$.

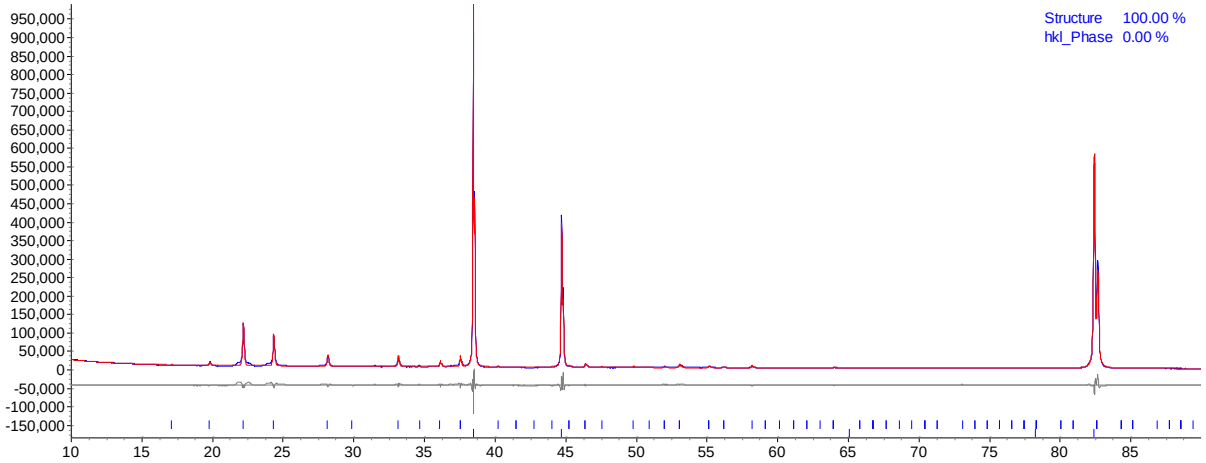


**Figure 4-10 Rietveld refinement plots of the X-ray diffraction data from the room temperature enriched $ZrW_2O_8$. $xH_2O$ (d9_01958). Rwp = 9.56 %**

In order to dehydrate this intermediate phase and obtained the desired enriched $ZrW_2O_8$, AS008A was transferred to an alumina boat and placed in a tube furnace. The tube furnace was immediately evacuated and heated to 225 °C at a rate of 10 °C.min$^{-1}$ then to 240 °C for two hours at a rate of 1.5 °C.min$^{-1}$. X-ray data of the resulting white powder (AS009B) were recorded (d5_01959) and are presented in Figure 4-11.

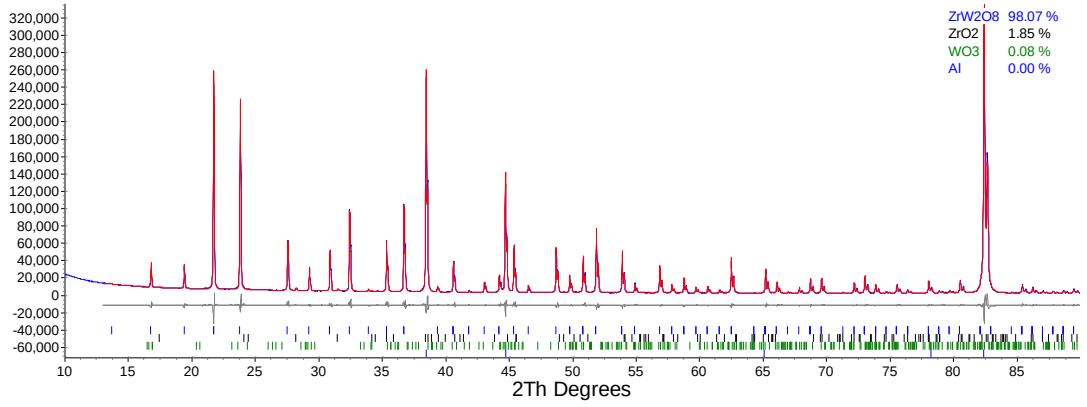


**Figure 4-11 Rietveld refinement plots of the X-ray diffraction data from the room temperature enriched α–$ZrW_2O_8$ (d9_01959). Rwp = 5.576 %**

The X-ray pattern was also recorded on an aluminium plate. The cubic Al phase was fitted by Pawley refinement optimising the cell parameter and peak intensities. A total of 32 parameters were then refined. The refined parameters included 8 global parameters (6 background parameters, 1 sample height displacement parameter, 1 axial divergence parameter) and 19 parameters to model the α-$ZrW_2O_8$ phase (1 cell parameters, 11 atom positions, 3 isotropic displacement parameters and 4

parameters to define the peak shapes + 4 parameters for spherical harmonics to describe a hkl dependence of the peak shape).

### 4.4.4. Synthesis of the γ-$ZrW_2O_8$ phase

The enriched AS009B sample was divided in 3 equal portions. One third was converted to α-phase and a third to the amorphous phase. To prepare the γ-phase, the sample was compressed under 2 tonnes of pressure using a 2.5 mm pellet press. This was repeated four times resulting in a white powder (AS013). The corresponding X-ray data are shown in Figure 4-12. The Rietveld fit of AS013 to γ-$ZrW_2O_8$ shows a very good fit to the data with a Rwp factor of 3.53 %. The refinement suggests only a very small residual portion of the α-phase (< 5 %).

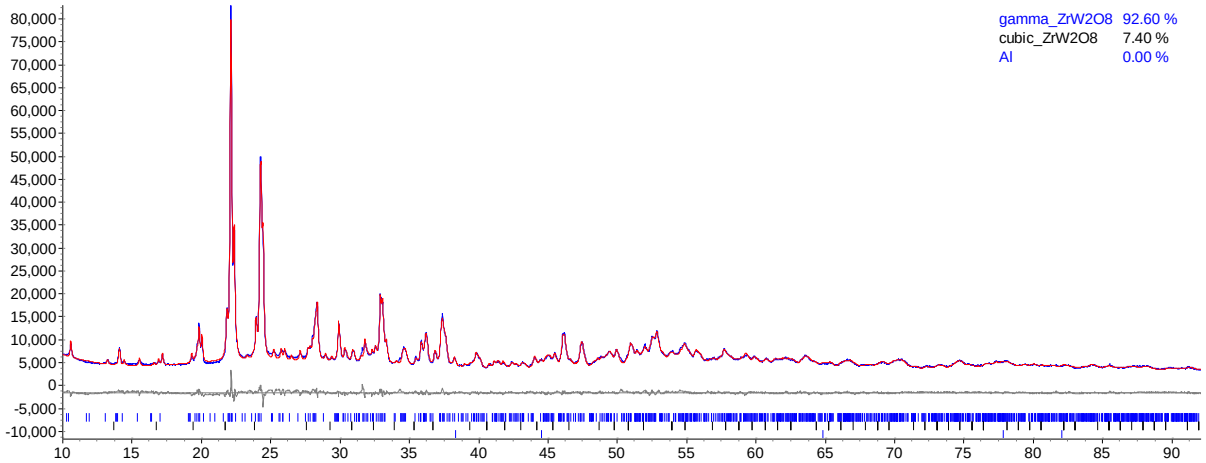


**Figure 4-12 Rietveld refinement plots of the X-ray diffraction data from the room temperature γ-$ZrW_2O_8$ (d9_01998). Rwp = 3.5%**

A total of 135 parameters were refined. The main phase is no longer the α-phase and good agreement is found with the γ-phase structure. The proportion of $WO_3$ and $ZrO_2$ present in the sample being negligible, only the parameters modelling the $ZrW_2O_8$ structure have been refined. The refined parameters included 8 global parameters (10 background parameters, 1 sample height displacement parameter, 1 axial divergence parameter) and 37 parameters to model the γ–$ZrW_2O_8$ phase (3 cell parameters, 27 atom positions (metal coordinates only), 3 isotropic displacement parameters and 4 parameters to define the peak shapes) and 12 parameters to model the α–$ZrW_2O_8$ phase (1 cell parameter, 11 atom positions).

### 4.4.5. Synthesis of amorphous ZrW2O8

The third part of AS009B was sent to Appleton Laboratory at Daresbury and pressurised under 110 T to convert the sample into its amorphous form (AS012, d9_01992). The resulting sample (AS013) X-ray spectrum is shown in Figure 4-13.

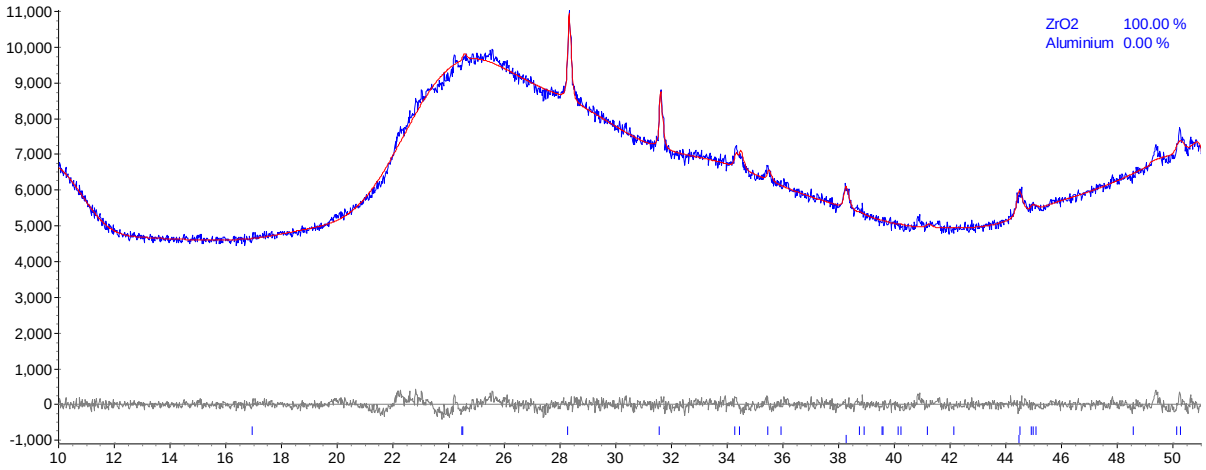


**Figure 4-13 Rietveld refinement plots of the X-ray diffraction data from the room temperature of AS0012 (amorphous phase of $ZrW_2O_8$ (d9_01992)). Rwp = 1.63 %**

The X-ray pattern shows significant background signal above which only very weak intensity diffraction peaks arise. The total diffracted intensity is comparable to the background seen in other diffraction patterns, consistent with a largely amorphous phase. The majority of the weak peaks can be explained by a minor amount of $ZrO_2$ being the only crystalline phase. The intensity of these reflections is consistent with the ~2 weight percent impurity present in the original cubic phase (Figure 4-11).

X-ray were again fitted for completeness. The cubic Al phase was fitted by Pawley refinement optimising the cell parameter. A total of 46 parameters and intensities were then refined. The refined parameters included 32 global parameters (30 background parameters, 1 sample height displacement parameter, 1 axial divergence parameter) and 14 parameters to model the $ZrO_2$ phase (4 cell parameters, 3 atom positions, 3 isotropic displacement parameters and 4 parameters to define the peak shapes).

**Table 4-1 Criteria of fit obtained for the different phases described above.**

| | $R_{wp}$ (%) | $R_{exp}$(%) | gof | $R_{Bragg}$(%) |
|---|---|---|---|---|
| $ZrO_2$ (d9_03286) | 8.96 | 6.98 | 1.65 | 1.77 |
| unenriched $\alpha$-$ZrW_2O_8$ (d9_01838) | 14.53 | 5.92 | 2.45 | 4.89 |
| $ZrW_2O_8.xH_2O$ | 9.57 | 0.87 | 10.97 | 2.87 |
| enriched $\alpha$-$ZrW_2O_8$ (d9_01959) | 6.99 | 1.26 | 5.5 | 2.22 |
| $\gamma$-$ZrW_2O_8$ (d9_01998) | 3.53 | 2.82 | 1.573 | 2.65 |
| amorphous $ZrW_2O_8$ (d9_01992) | 1.63 | 1.24 | 1.32 | 0.40 |

## 4.5. Experimental and calculated 1D $^{17}O$ spectra

The three phases of enriched $ZrW_2{}^{17}O_8$ described above have been successfully synthesised. Figure 4-14 (a), (b) and (c) show the $^{17}O$ MAS NMR spectra of the three phases. The α-phase spectrum was already reported in previous studies by Matt Hampson[21] and a tentative assignment of the four oxygen sites was proposed. The $^{17}O$ MAS spectra of the γ- and amorphous phases are recorded for the first time.

The four resonances revealed by the α-phase spectra are assigned to the four crystallographically unique oxygen sites present as indicated in Figure 4-14 (a). The assignment shown here is based on DFT calculations results presented in Figure 4-15 and corroborate the assumptions made by Hampson[21] using simple chemical shielding arguments and comparison with solution studies. The ~1:6 ratio revealed by the experiment between the intensity of O3 or O4 signals and the combined O1/O2 on site 12c) signal is also consistent with this assignment (O3/O4 are on Wyckoff site 4a and O1/O2 and O2. Looking at the spectra of the three phases in Figure 4-14 one can notice a decrease of chemical shift range while going from the α to the amorphous phase. This observation suggests a decrease in the chemical shift environments distribution and is discussed below.

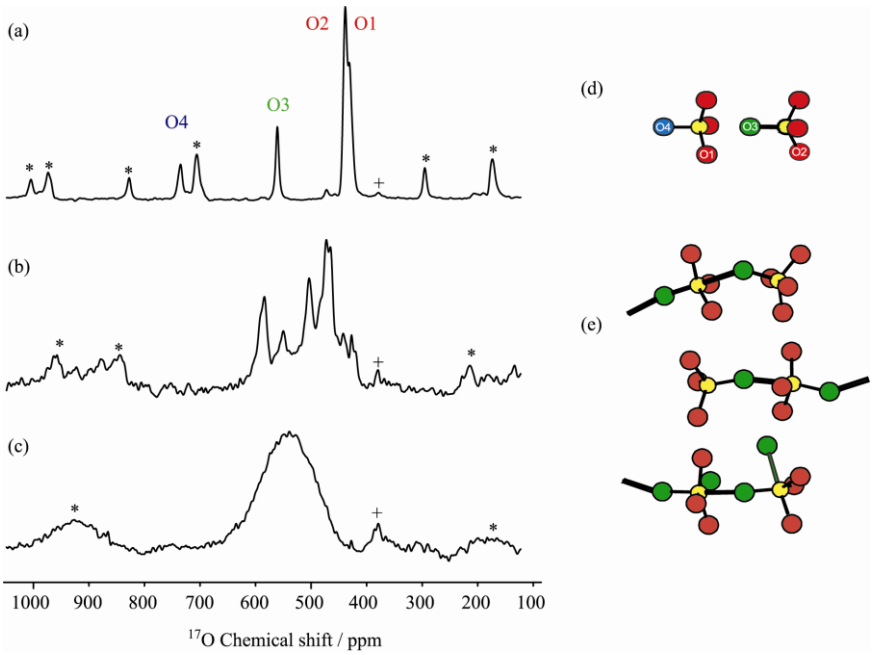


**Figure 4-14 $^{17}O$ MAS NMR spectra for three phases of $ZrW_2O_8$: (a) the cubic, α-phase (288 scans with a recycle delay of 60 s), (b) the γ-phase (164 scans with a recycle delay of 34 minutes), and (c) the amorphous phase (288 scans with a recycle of 128 s). The magic-angle spinning rate was 25 kHz for (b) and (c), and 18 kHz for (a). Asterisks indicate spinning sidebands, while the + indicates the natural-abundance $^{17}O$ signal from the zirconia rotor[22]. On the right are schematic illustrations of the local tungsten environments in (d) α-$ZrW_2O_8$ and (e) γ-$ZrW_2O_8$.**

In the α-phase (Figure 4-14 a), O1 and O2 are both part of Zr–O–W two-coordinate oxygen linkages and therefore have similar chemical environments. Their NMR signals appear as two barely resolved

resonances at ~434 ppm. O3 and O4 are the apical oxygens of the $WO_4$ units with unusual coordinations. O3 lies in an unsymmetrical W1.....O3–W2 site, with a much shorter distance to W2 than W1 (1.7 vs 2.4 Å) and gives a resonance at 561 ppm whereas the resonance at 734 ppm corresponds to the strictly one-coordinate O4 (see Figure 4-14(d)). It is worth noting that no such oxygen is observed in the spectra of other phases suggesting that no O4 type of oxygen (around 730 ppm) remains after the pressure induced transitions.

The $^{17}O$ NMR spectrum of the $\gamma$ form, Figure 4-14 (b), is entirely consistent with structural studies[(10)]. In the reported model, all oxygens are two coordinated due to the transformation of W1.....O3–W2 linkages into stronger W1–O3 bonds and cross-linking of tetrahedral groups such that all O4 oxygens link to other W sites under pressure (Figure 4-14 (d)). Thus no one-coordinate O4 type remains and all the oxygens belonging to a W-O-W linkage adopt chemical environments similar to that of O3 in the low pressure structure. This is shown in the NMR spectrum from the increasing number of peaks observed from ~590 to ~420 ppm and an absence of peaks in the area of 730 ppm. The overlap does not, however, allow the assignment of individual peaks to a given oxygen (6 crystallographically distinct oxygens in W–O–W environments and 18 in Zr–O–W environments) but, from the information provided by both the $\alpha$-and $\gamma$ spectra, W-O-W oxygens are likely to correspond to higher chemical shifts values than W-O-Zr. DFT calculations performed on the $\gamma$-phase (discussed later) are consistent with this assumption.

Figure 4-14 (c) shows the NMR spectrum of the amorphous material. As in the $\gamma$-phase, no "O4" type environments are observed and a single broad resonance centered at 539 ppm is seen. The similarities with the $\gamma$-phase spectrum suggest that both materials have a similar range of chemical environment. This NMR spectrum unambiguously rules out the possibility that the amorphous material is a 2-phase mixture of amorphous $ZrO_2$ and $WO_3$ as had been suggested [(16, 17)]. The reduced range of chemical shifts observed also suggests that the differences in oxygen chemical environments in the disordered material are smaller than in the crystallographically-ordered $\gamma$ form. The information from $^{17}O$ NMR is also consistent with the structure proposed recently via reverse Monte Carlo modelling of high-quality total neutron scattering data on the amorphous material[(15)] and discussed in the previous section (4.1). The model arising from this work retains a pseudo-ordered array of Zr atoms very similar to the $\gamma$-structure but contains significant disorder in the $WO_n$ polyhedral array. It would be interesting to simulate the NMR data of the RMC model. Unfortunately it contains 2816 atoms and CASTEP calculations of NMR parameters would be impossible using our current computing capabilities.

The DFT calculated spectra for the two crystalline phases ($\alpha$ and $\gamma$) for which crystal structures are provided are presented in the following sections.

### 4.5.1. DFT simulations of $\alpha$-$ZrW_2O_8$

The $^{17}O$ MAS NMR spectrum was recorded at a spinning speed of 18 kHz in a 2.5 mm rotor. The $^{17}O$ signal was referenced to $H_2{}^{17}O$ signal. The CASTEP computer code was used to calculate the $^{17}O$

NMR parameters (isotropic shieldings and quadrupole parameters). The optimisation procedures of the different parameters used in the present calculations are described in Chapter 2. The output of our calculations provides isotropic shieldings which have to be "referenced" to experimental shift values by reversing the sign and adjusting the mean of the calculated values to match the mean of the experimental values. The simulated spectrum was generated using pNMRsim[(23)] for a spinning speed of 18 kHz.

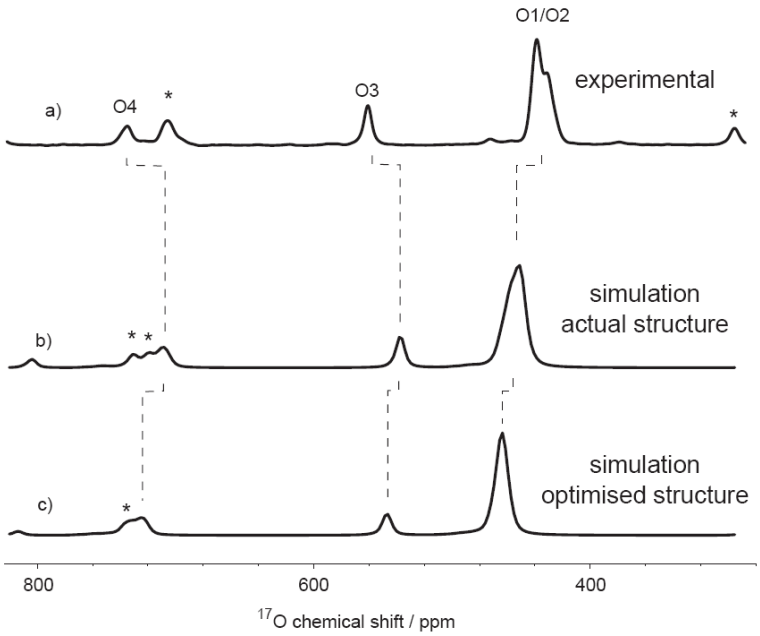


**Figure 4-15 Comparison of (a) experimental MAS NMR spectrum of α-$ZrW_2O_8$ and (b) and (c) simulated NMR spectra based on $^{17}O$ NMR parameters (shifts and quadrupole couplings) derived from DFT calculations on a neutron structure of α-$ZrW_2O_8$[(24)] and its geometry optimised structure respectively. The mean of the DFT calculated shieldings has been adjusted to the mean of the experimental values corresponding to a shift of 263 ppm, and dashed lines connect the predicted and experimental shifts**

Although the qualitative agreement between calculated and experimental shifts shown in Figure 4-15 is good, a few discrepancies remain between the two spectra. The effect of different structural variations (unit cell parameters, atomic coordinates) on the $^{17}O$ NMR spectra were investigated. Although these will be described in more detail in section 5.6, it is worth noting now that the $^{17}O$ chemical shifts were found to be extremely sensitive to changes in individual internal coordinates. In contrast, varying the (unique) cell dimension parameter for this cubic structure induces significantly smaller effects on the spacings of $\delta_{iso}$ values. However, an overall shift of the $\delta_{iso}$ values is observed. Due to the referencing procedure used this shift is not significant.

### 4.5.2. DFT simulations of γ-$ZrW_2O_8$

The experimental spectrum was recorded on a 500 MHz Varian spectrometer at a spinning speed of 18 kHz on a sample packed in a 2.5 mm zirconia rotor. The bottom spectra was simulated for an identical spinning speed. Both spectra have been processed by applying a 300 Hz gaussian line width. Calculations were performed using coordinates reported by Jorgensen et *al.*[(25)]. The parameters used for the computation are the same as the ones used for the α-phase as optimisation of the parameters

on such large system would be incredibly time consuming. The calculations took about 21 days (1862748 s) using 30 processors to be completed. Geometry optimisation on this structure could not be completed with a sensible time scale.

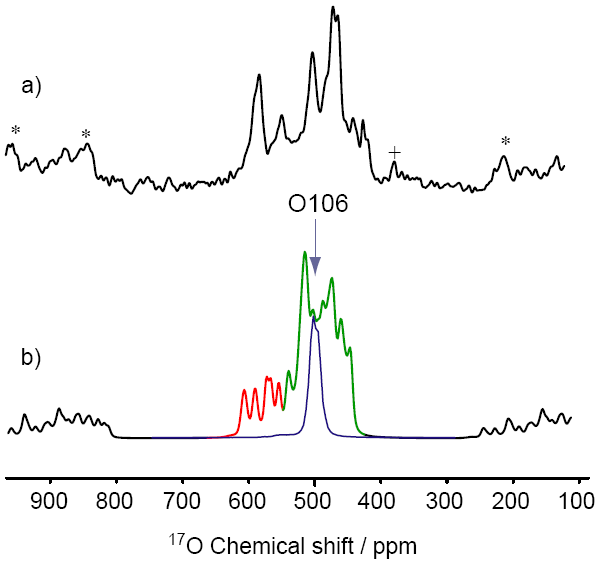


**Figure 4-16 Comparison of (a) experimental MAS NMR spectrum of γ-$ZrW_2O_8$ and (b) simulated NMR spectrum based on $^{17}O$ NMR parameters (shifts and quadrupolar couplings) derived from DFT calculation on a neutron structure of γ-$ZrW_2O_8$[25]. The calculated pattern has been shifted by +263 ppm as for the α-phase calculations. The resonances in red and green show the calculated W-O-W and W-O-Zr oxygens respectively. O106 (see Figure 4-6) is shown in blue.**

Though the agreement between the experimental and calculated patterns is not perfect, we can appreciate that the main features as well as the spectral width are reasonably consistent.

The NMR spectra can be divided in two distinct regions. The lower chemical shift values correspond in general to the 18 oxygen sites attached to Zr atoms while chemical shift values above 540 ppm correspond to five of the W-O-W oxygens (O101, O102, O103, O104 and O105 described earlier in this chapter). Looking at our calculation results, only the O106 chemical shift does not appear in the same range and is shifted to lower values (480 ppm). This O106 is the only W-O-W oxygen of the γ-phase that is noticeably different to the others. While all the other W-O-W oxygens can be seen as 1+1 bonded (with differences from 0.58 Å to 0.76 Å between the two W-O distances around a given oxygen), O106 is the only one to be strictly bonded to its two surrounding tungsten. It has O-W distances of 2.14 Å and 1.78 Å respectively, whereas the next most symmetrical O-W-O linkage is 2.37 Å and 1.75 Å This smaller bond length asymmetry (0.36 Å) falls into the range of Zr-O-W oxygens (with an asymmetry ranging from 0.007 Å to 0.4223 Å).

## 4.6. Variable temperature $^{17}O$ NMR studies of $\alpha$-$ZrW_2O_8$

As mentioned earlier, possible mechanisms leading to negative thermal expansion in $ZrW_2O_8$ have been widely discussed. The latest model was proposed by Tucker et *al*.[12] and involves predominantly the simultaneous rotations of $ZrO_6$ and translation of $WO_4$ poyhedra. These movements lead to different network deformations such as bond lengths and bond angles variations that cannot be fully represented in a pure RUM model as described in section 5.1. Due to the high sensitivity of NMR to local changes, variable temperature NMR experiments may therefore be a powerful independent probe of such structural modifications.

Variable temperature experiments have been recorded at a spinning speed of 5 kHz in a 2.5 mm zirconia rotor. Our NMR equipment is designed for low temperature experiments down to 123 K (-150°C) however in practice, the lowest temperature that could be reached and maintained long enough for experiments to be run is 153 K (-120°C). Twelve MAS NMR data sets have been collected between 16°C and -120°C and some of them are shown in Figure 4-17. The experimental data show that the O3 chemical shift moves significantly towards smaller values while the effect of temperature on O1/O2 and O4 sites is smaller. These observations suggest that temperature change has a largest effect on the O3 chemical environment. In order to correlate these NMR data to structural changes, a quantitative analysis of the chemical shifts evolution with temperature is needed. As the variations in chemical shifts are very subtle, it is essential to process the NMR data in a consistent and sensible way. The peak broadening and asymmetry due to quadrupolar coupling of each site is rather small therefore the analysis was performed in a similar way as what would be done for a spin 1/2 nucleus. The chemical shift values extracted by taking the maximum intensity (rather than the centre of gravity) of the peaks are reported in Table 4-2.

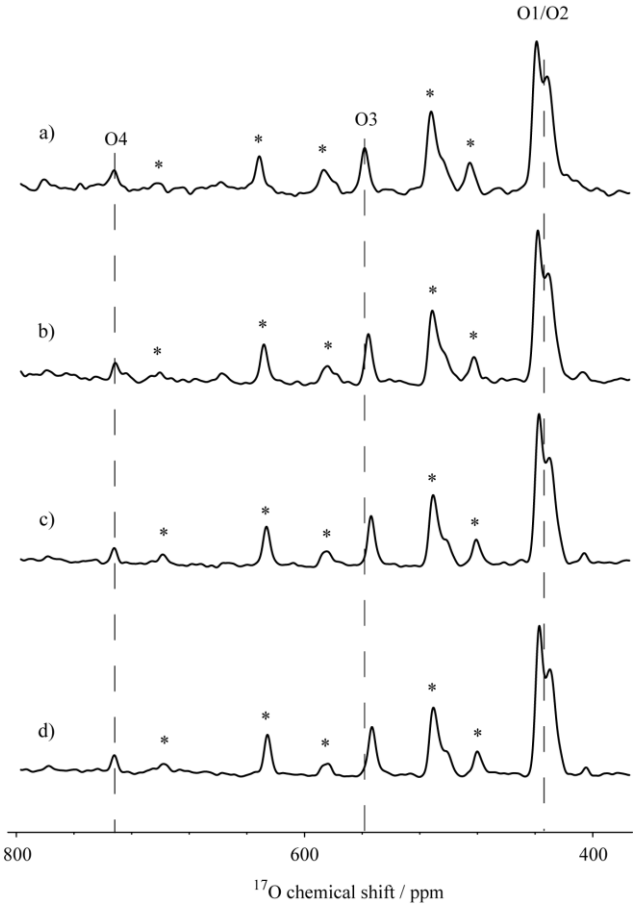


**Figure 4-17 Variable temperature experiments on α-$ZrW_2O_8$ recorded at 5 kHz in a 4 mm rotor on a 500 MHz Varian Chemagnetics a) RT, b) -50°C, c) -100°C, d) -120°C.**

Since all the peak positions change slightly with temperature, it seems sensible to reference the spectra internally. Since the O4 signal appears to be the least affected by the temperature changes, we chose to look at the variations of O1, O2 and O3 chemical shifts relative to the O4 position at a given temperature noted: δO1-δO4, δO2-δO4, δO3-δO4 respectively. From the structure, it is unsurprising that the strictly one-coordinate oxygen changes least with temperature. Such relative shift variations will also be used later when dealing with unreferenced CASTEP calculated chemical shielding values. Referencing in this way also reduces the potential errors associated with slightly different processing of the data (mainly due to phasing). If we then consider that a given δO*n*-δO4 variation is zero at 16 °C, the overall variation (in ppm) of $^{17}$O chemical shift relative to O4 from 16 ºC to -120 °C is reported in Table 4-3 and plotted in Figure 4-18.

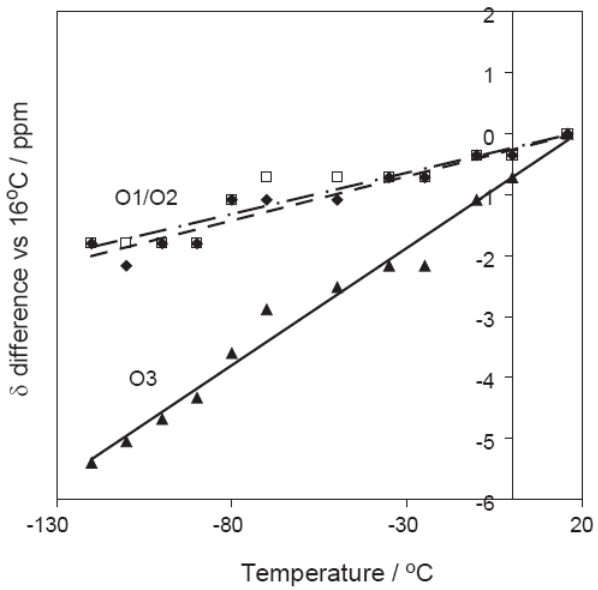


**Figure 4-18 Variation of the differences in the $^{17}O$ chemical shifts relative to O4 chemical shift as a function of temperature. The ($\delta_{iso}$On-$\delta_{iso}$O4) values at 16°C are set to zero. The shift differences between O4 and O1, O2 and O3 are presented as diamonds, squares and triangles respectively.**

By fitting our experimental data to a linear trend, we obtained equations (1), (2) and (3) for the variations of O1, O2, and O3 respectively. The variation on the O3 shift is three times larger than those of O1 and O2 which confirms that the O3 environment is the most affected by the temperature variation.

$$\Delta(\delta O1-\delta O4) = (0.0145 \text{ ppm/°C})\ T - 0.2641 \text{ ppm} \quad (1)$$

$$\Delta(\delta O2-\delta O4) = (0.0136 \text{ ppm/°C})\ T - 0.2294 \text{ ppm} \quad (2)$$

$$\Delta(\delta O3-\delta O4) = (0.0385 \text{ ppm/°C})\ T - 0.7232 \text{ ppm} \quad (3)$$

The evolution of the $^{17}O$ chemical shifts can therefore be quantified and it is interesting to look at which structural changes are likely to generate such an effect.

**Table 4-2 Chemical shift values of $^{17}O$ sites in $ZrW_2O_8$ (referenced to $H_2{}^{17}O$) as a function of temperature.**

| T(°C) | δO1(ppm) | δO2(ppm) | δO3(ppm) | δO4(ppm) |
|---|---|---|---|---|
| 16 | 432.4 | 440.0 | 561.1 | 737.0 |
| 0 | 432.1 | 439.6 | 560.4 | 737.0 |
| -10 | 432.1 | 439.6 | 560.0 | 737.0 |
| -25 | 432.1 | 439.6 | 559.3 | 737.3 |
| -35 | 431.7 | 439.3 | 558.9 | 737.0 |
| -50 | 431.0 | 438.9 | 558.2 | 736.6 |
| -70 | 431.0 | 438.9 | 557.8 | 736.6 |
| -80 | 431.0 | 438.6 | 557.1 | 736.6 |
| -90 | 431.0 | 438.6 | 557.1 | 737.3 |
| -100 | 430.6 | 438.2 | 556.4 | 737.0 |
| -110 | 430.3 | 438.2 | 556.0 | 737.0 |
| -120 | 431.0 | 438.6 | 556.0 | 737.3 |

Structural variations of $\alpha$-$ZrW_2O_8$ as a function of temperature were described by Tucker et *al*.[12]. As discussed earlier, this model agrees to some extent with the pure RUM model proposed in 1996 by Evans et *al*.[2]. However, the RUM model was obtained using diffraction techniques and Rietveld refinement and therefore gives information on the average structure of $ZrW_2O_8$. Total neutron scattering is, like NMR, sensitive to the local structure. One of the noticeable differences between the two models is the variation of the W1-O3 bond distance with temperature. In the RUM model as the temperature increases W1 and O3 get closer while the mechanism postulated using total neutron scattering gives an expansion as shown in Figure 4-19. In fact, total scattering predicts W1-O3 increases by 0.08 Å between 0 K and 300 K. In both models, the O3 environment is most changed which is consistent with the NMR data.

**Table 4-3 Variations of the experimental $^{17}O$ chemical shifts in $\alpha$-$ZrW_2O_8$ as a function of temperature.**

| T(°C) | $\delta$O1-$\delta$O4 | $\delta$O2-$\delta$O4 | $\delta$O3-$\delta$O4 | $\Delta(\delta$O1-$\delta$O4) | $\Delta(\delta$O2-$\delta$O4) | $\Delta(\delta$O3-$\delta$O4) |
|---|---|---|---|---|---|---|
| 16 | -304.5 | -297.0 | -175.9 | 0 | 0 | 0 |
| 0 | -304.9 | -297.3 | -176.6 | -0.36 | -0.36 | -0.72 |
| -10 | -304.9 | -297.3 | -177.0 | -0.36 | -0.36 | -1.08 |
| -25 | -305.3 | -297.7 | -178.0 | -0.72 | -0.72 | -2.16 |
| -35 | -305.3 | -297.7 | -178.0 | -0.72 | -0.72 | -2.16 |
| -50 | -305.6 | -297.7 | -178.4 | -1.08 | -0.72 | -2.52 |
| -70 | -305.6 | -297.7 | -178.8 | -1.08 | -0.72 | -2.88 |
| -80 | -305.6 | -298.1 | -179.5 | -1.08 | -1.08 | -3.61 |
| -90 | -306.3 | -298.8 | -180.2 | -1.80 | -1.80 | -4.33 |
| -100 | -306.3 | -298.8 | -180.6 | -1.80 | -1.80 | -4.69 |
| -110 | -306.7 | -298.8 | -180.9 | -2.16 | -1.80 | -5.05 |
| -120 | -306.3 | -298.8 | -181.3 | -1.80 | -1.80 | -5.41 |

Experimental NMR data therefore support either structural study in that O3 is predicted to changes significantly. By supporting NMR experiments with a simple DFT calculation it may be possible to quantify the NMR observations to support one or the other conclusion.

### 4.6.1. Modeling structures using the Distance Least Square (DLS) method

In the mechanism proposed by Tucker et *al*. [12] for the negative thermal expansion phenomenon in $ZrW_2O_8$, the W1-O3 distance increases significantly with temperature. The model assumes that the $ZrO_6$ octahedron and $W(2)O_4$ tetrahedron are close to regular while $W(1)O_4$ has a more distorted symmetry due to the proximity of the O3 atom. We attempted to generate model structures that simulate, as well as possible, the proposed local change in structure around O3. To do so, we used the distance least squares (DLS) method described in Chapter 1. A typical file for the DLS modelling is given in the appendix. During this procedure, the $ZrO_6$ octahedron and $W(2)O_4$ tetrahedron are restrained to remain approximately regular while $W(1)O_4$ is restrained to its distorted conformation. The W1-O3 distance was then systematically varied and the rest of the structure refines to optimise local geometries.

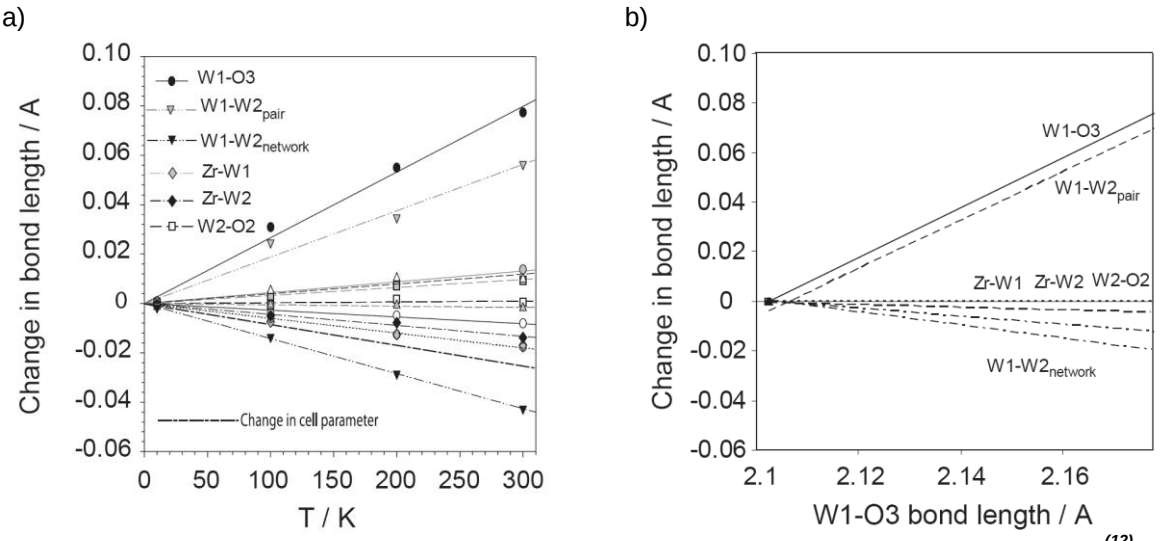


**Figure 4-19 Variations in bond distances a) as a function of temperature adapted from reference [12] and b) as a function of the corresponding W1-O3 bond length obtained in our DLS models.**

Extracting the variation of bond length proposed by Tucker et *al*. from Figure 4-18a) we obtain a variation by 2.66 x $10^{-4}$ Å / $K^{-1}$ for the W1-O3 bond length with temperature. The distance will therefore vary by 0.079 Á over a 300 K temperature range which might lead to several problems. First of all, the DLS minima are likely to be very similar while applying such small variations and the resulting structures could therefore be undistinguishable. Secondly, the errors on the $^{17}O$ NMR DFT calculations are likely to be large compared to the actual chemical shift variations and no reliable results are likely to be extracted. It seems then sensible to extend the temperature range and to generate structures with «artificial» W1-O3 bond distances ranging over a wider range of values (set from 2.1 Å to 2.5 Å every 0.1 Å). After DLS refinement, models show W1-O3 distances variations of 0.40084 Å (from 2.10233 Å to 2.50317 Å) which corresponds to a variation in temperature of approximately 1500 K. CASTEP calculations to determine the NMR parameters of the six generated structures were performed and the resulting artificial temperature/bond lengths and differences in chemical shift values are listed in Table 4-4.

**Table 4-4 Variation of the CASTEP calculated $^{17}O$ chemical shifts as a function of artificial temperature**

| T / °C | W1-O3(Å) | δO1-δO4 | δO2-δO4 | δO3-δO4 | Δ(δO1-δO4) | Δ(δO2-δO4) | Δ(δO3-δO4) |
|---|---|---|---|---|---|---|---|
| 386 | 2.50 | -268.75 | -269.37 | -169.90 | -0.62 | -2.09 | 12.92 |
| 16 | 2.41 | -268.13 | -267.28 | -182.80 | 0.00 | 0.00 | 0.00 |
| -12.23 | 2.40 | -268.56 | -268.17 | -184.70 | -0.43 | -0.89 | -1.95 |
| -396.9 | 2.30 | -266.49 | -264.01 | -195.80 | 1.64 | 3.26 | -13.00 |
| -782.8 | 2.20 | -267.34 | -260.36 | -210.00 | 0.79 | 6.92 | -27.19 |
| -1156 | 2.10 | -266.38 | -251.99 | -218.40 | 1.75 | 15.29 | -35.57 |

Figure 4-20 a) plots data from Table 4-4 over the temperature range recorded experimentally and confirms that the isotropic chemical shifts can be strongly influenced by small variations in atomic positions. It is obvious that the O3 isotropic chemical shift is strongly influenced by the W1-O3 bond distance variation and a similar trend as that observed experimentally (Figure 4-17) is seen. However, O1 and O2 chemical shifts are influenced in the opposite way to the experimental data. It seems therefore that this model where only one local parameter (W1-O3 bond distance) is modified is not sufficient to completely describe the overall NMR behaviour. We can therefore think, considering the large isotropic thermal contraction of $ZrW_2O_8$, that over such a wide range of temperature the unit cell parameters variations may also have an influence on chemical shift.

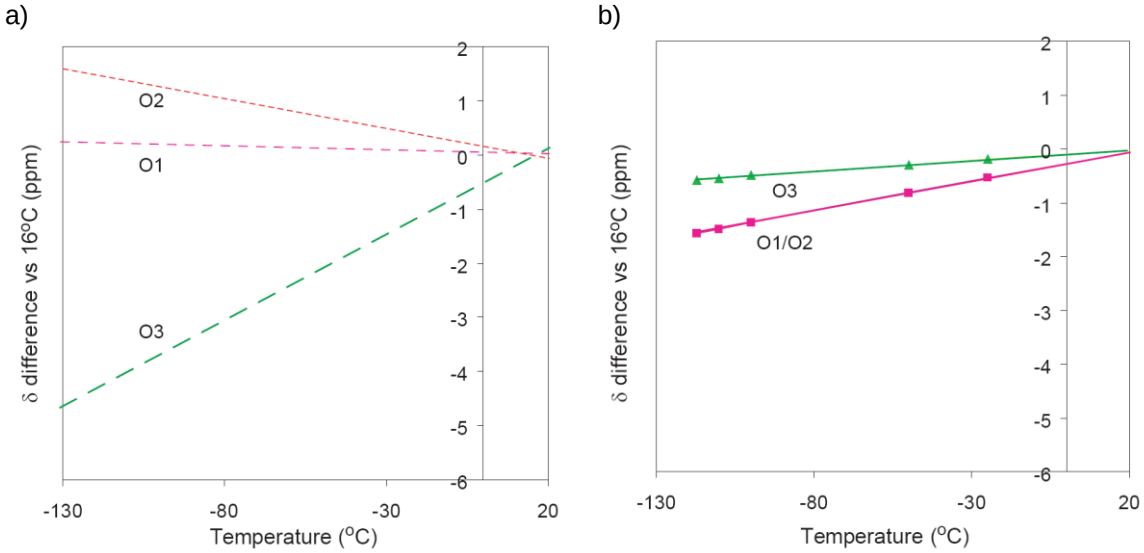


**Figure 4-20 Variation of the $^{17}O$ chemical shift values obtained by DFT calculations on our DLS models on α-$ZrW_2O8$ while varying a) the W1-O3 distance, b) the cubic unit cell parameter.**

The evolution of the NMR isotropic chemical shifts when the cell parameters are changed by amounts corresponding to the thermal contraction are presented in Table 4-5. This contraction of the unit cell shifts the overall spectra towards higher chemical shift values as the temperature increases. Figure 4-20b) plots of data from Table 4-5 and shows that the cell parameters variation has a much smaller influence on the splitting between the different $^{17}O$ shifts (especially on O3) than the variation of W1-O3 bond distance. However, the influence of the cell contraction will compensate the effects of the W1-O3 variations.

**Table 4-5 Chemical shift values obtained by CASTEP calculations while varying the cubic unit cell parameter.**

| T(°C) | δO1 | δO2 | δO3 | δO4 | Δ(δO1-δO4) | Δ(δO2-δO4) | Δ(δO3-δO4) |
|---|---|---|---|---|---|---|---|
| 100 | 200.92 | 197.23 | 276.522 | 452.89 | 0.7625 | 0.7837 | 0.2871 |
| 26 | 202.05 | 198.34 | 278.128 | 454.78 | 0 | 0 | 0 |
| -25 | 202.91 | 199.19 | 279.323 | 456.17 | -0.5345 | -0.542 | -0.1958 |
| -50 | 203.28 | 199.56 | 279.864 | 456.82 | -0.8042 | -0.816 | -0.2988 |
| -100 | 204.15 | 200.42 | 281.089 | 458.23 | -1.3538 | -1.377 | -0.49 |
| -110 | 204.29 | 200.56 | 281.288 | 458.5 | -1.4767 | -1.496 | -0.5534 |
| -117 | 204.4 | 200.67 | 281.46 | 458.69 | -1.5571 | -1.583 | -0.5764 |

**Table 4-6 Linear variations of the calculated and experimental $^{17}O$ chemical shift differences as a function of temperature in $ZrW_2O_8$**

| | Δ(δO1-δO4) | Δ(δO2-δO4) | Δ(δO3-δO4) |
|---|---|---|---|
| W1-O3 variations | (-0.0015 ppm/°C)T-0.0215 ppm | (-0.011 ppm/°C)T-0.1774 ppm | (0.0317 ppm/°C)T-0.5085 ppm |
| Unit cell | (0.0093 ppm/°C)T-0.2690 ppm | (0.0095 ppm/°C)T-0.2731 ppm | (0.0035 ppm/°C)T-0.0986 ppm |
| Sum | (0.0078 ppm/°C)T-0.2905 ppm | (0.0015 ppm/°C)T-0.2294 ppm | (0.0352 ppm/°C)T-0.6071 ppm |
| Experimental | (0.0145 ppm/°C)T-0.2641 ppm | (0.0136 ppm/°C)T-0.2294 ppm | (0.0385 ppm/°C)T-0.7232 ppm |

The linear regressions of both effects and their sum are reported in Table 4-6. Looking at this table and Figure 4-20 a) and b), it seems that the combination both effects leads to acceptable agreement to the experimental data. It is then interesting to visually compare the evolutions of chemical shifts observed experimentally to the ones obtained with our calculations. This comparison is presented in Figure 4-21.

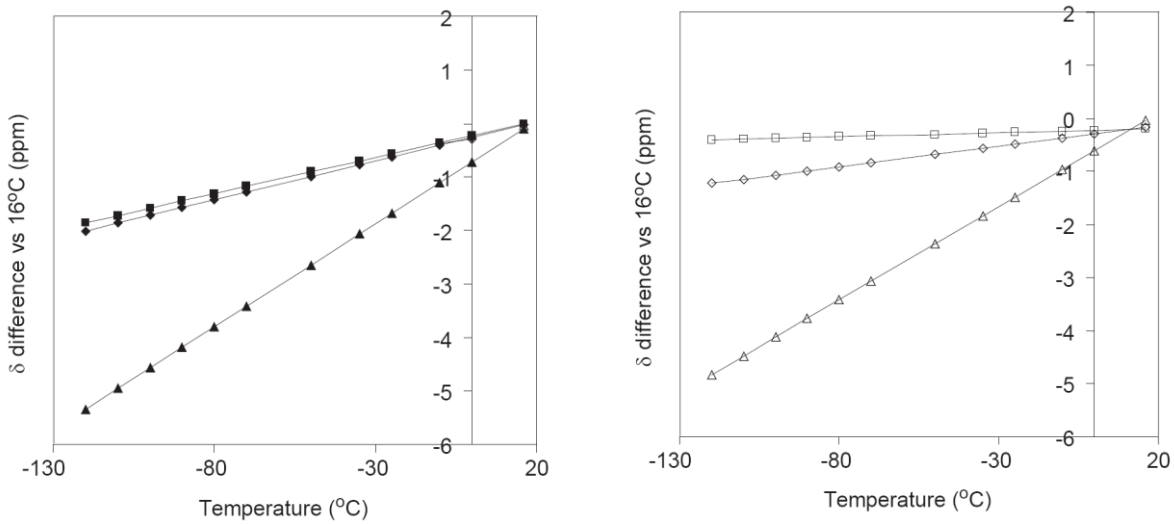


**Figure 4-21 Comparison between the variations of experimental (full) and calculated (empty) $^{17}O$ chemical shift differences in $ZrW_2O_8$ as a function of temperature.**

Although the evolutions predicted by our calculations do not completely reproduce the experimental data, a good agreement is observed. Given the simplicity of the model, one wouldn't expect a better level of agreement. Our calculations do, however, strongly support the model proposed by Tucker et *al.* on for the negative thermal expansion mechanism in ambient pressure $ZrW_2O_8$ phase.

## 4.7. Conclusions

$^{17}O$ MAS NMR spectra and DFT calculated NMR spectra of three phases of $ZrW_2O_8$ have been presented. In the simple cubic $\alpha$-phase, the calculations were first used to to confirm the assignment of the different resonances and thus to relate the oxygen environments to $^{17}O$ chemical shifts values. The studies on the $\alpha$-phase allowed us to comment as well on the $^{17}O$ MAS spectra of the two other high pressure $ZrW_2O_8$ phases, namely the $\gamma$ and the amorphous phase. The diminution of the chemical shift range shown by a narrowing of the overall NMR signal is consistent with structures reported in the literature.

In order to give new insights in the study of the negative thermal expansion (NTE) mechanism in $\alpha$-$ZrW_2O_8$, $^{17}O$ MAS NMR variable temperature experiments were performed. The data showed an obvious shift of the O3 position as a function of temperature suggesting significant modifications in its chemical environment. Structures have been modeled using distance least squares method by exploiting assumptions made in reported total neutron scattering studies. CASTEP DFT calculations were performed on those models in order to be compared with our experimental data. The NMR behaviour predicted on these models is consistent with our variable temperature MAS experiments. Such observations therefore support the NTE mechanism proposed by Tucker et *al.*[(26)].

## 4.8. References


1. J. Graham, A. D. Wadsley, J. H. Weymouth, L. S. Williams, *Journal of the American Ceramic Society* **42**, 570-570 (1959).
2. J. S. O. Evans, T. A. Mary, T. Vogt, M. A. Subramanian, A. W. Sleight, *Chemistry of Materials* **8**, 2809-2823 (Dec, 1996).
3. S. Allen, J. S. O. Evans, *Journal of Materials Chemistry* **14**, 151-156 (2004).
4. M. R. Hampson, P. Hodgkinson, J. S. O. Evans, R. K. Harris, I. J. King, S. Allen, F. Fayon, *Chemical Communications*, 392-393 (Feb 21, 2004).
5. M. R. Hampson, J. S. O. Evans, P. Hodgkinson, *Journal of the American Chemical Society* **127**, 15175-15181 (Nov 2, 2005).
6. A. K. A. Pryde, K. D. Hammonds, M. T. Dove, V. Heine, J. D. Gale, M. C. Warren, *Journal of Physics-Condensed Matter* **8**, 10973-10982 (Dec 9, 1996).
7. J. P. Amoureux, F. Bauer, H. Ernst, C. Fernandez, D. Freude, D. Michel, U. T. Pingel, *Chemical Physics Letters* **285**, 10-14 (Mar 13, 1998).
8. G. Ernst, C. Broholm, G. R. Kowach, A. P. Ramirez, *Nature* **396**, 147-149 (Nov 12, 1998).
9. M. G. Tucker, D. A. Keen, J. S. O. Evans, M. T. Dove, *Journal of Physics-Condensed Matter* **19** (Aug 22, 2007).
10. J. S. O. Evans, Z. Hu, J. D. Jorgensen, D. N. Argyriou, S. Short, A. W. Sleight, *Science* **275**, 61-65 (Jan 3, 1997).
11. J. S. O. Evans, J. D. Jorgensen, S. Short, W. I. F. David, R. M. Ibberson, A. W. Sleight, *Physical Review B* **60**, 14643-14648 (Dec 1, 1999).

12. M. G. Tucker, D. A. Keen, J. S. O. Evans, M. T. Dove, *J. Phys.: Condens. Matter* **19** (2007).
13. C. A. Figueiredo, J. Catafesta, J. E. Zorzi, L. Salvador, I. J. R. Baumvol, M. R. Gallas, J. A. H. da Jornada, C. A. Perottoni, *Physical Review B* **76** (2007).
14. C. A. Perottoni, J. A. H. da Jornada, *Science* **280**, 886-889 (May 8, 1998).
15. D. A. Keen, A. L. Goodwin, M. G. Tucker, M. T. Dove, J. S. O. Evans, W. A. Crichton, M. Brunelli, *Physical Review Letters* **98** (Jun 1, 2007).
16. A. K. Arora, V. S. Sastry, P. C. Sahu, T. A. Mary, *Journal of Physics-Condensed Matter* **16**, 1025-1031 (Feb 25, 2004).
17. T. R. Ravindran, A. K. Arora, T. A. Mary, *Journal of Physics-Condensed Matter* **13**, 11573-11588 (Dec 17, 2001).
18. T. Varga, A. P. Wilkinson, A. C. Jupe, C. Lind, W. A. Bassett, C. S. Zha, *Physical Review B* **72** (Jul, 2005).
19. S. Allen, *PhD thesis, Durham University* (2003).
20. M. R. Hampson, S. Allen, I. J. King, C. J. Crossland, P. Hodgkinson, R. K. Harris, F. Fayon, J. S. O. Evans, *Solid State Sciences* **7**, 819-826 (Jul, 2005).
21. M. R. Hampson, (2006).
22. T. J. Bastow, S. N. Stuart, *Chem. Phys.* **143**, 459-467 (Jun 1, 1990).
23. P. Hodgkinson, *http://www.durham.ac.uk/paul.hodgkinson/pNMRsim*.
24. J. S. O. Evans, W. I. F. David, A. W. Sleight, *Acta Crystallographica Section B-Structural Science* **55**, 333-340 (Jun 1, 1999).
25. J. D. Jorgensen, Z. Hu, S. Teslic, D. N. Argyriou, S. Short, J. S. O. Evans, A. W. Sleight, *Physical Review B* **59**, 215-225 (Jan 1, 1999).
26. M. G. Tucker, A. L. Goodwin, M. T. Dove, D. A. Keen, S. A. Wells, J. S. O. Evans, *Physical Review Letter* **95**, 255501 (16 Decmber 2005, 2005).

# Chapter 5. Tungsten trioxide

## 5.1. $WO_3$ reported structures

The structure of tungsten trioxide can be described as a network of corner sharing $WO_6$ octahedra. In its ideal highest symmetry form, the W and O atoms would be arranged in a $ReO_3$-type cubic structure (atomic positions W (0, 0, 0) and O (1/2, 0, 0), space group $Pm\bar{3}m$). Despite this simple ideal structure, many changes occur in the octahedral network on decreasing temperature from its melting point at 1700°C. Distortions and tilts of the octahedra as well as W atom displacements lead to a surprising number of phase transitions and interesting physical properties (Figure 5-1).

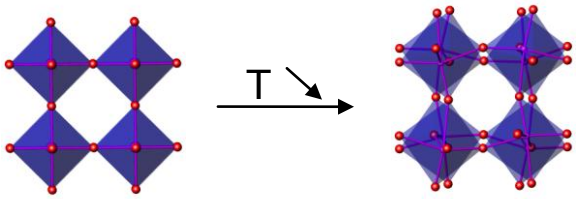


**Figure 5-1 Polyhedral representation of the ideal $WO_3$ structure and an example of a distorted structure ($P\bar{1}$) obtained when the temperature decreases.**

Seven different phases of $WO_3$ have been described in the literature and occur through the sequence of transitions shown in Figure 5-2. The $P2_1/c$ to *Pbcn* and $P\bar{1}$ to *P*c phase transitions were reported to be first order while all the other phases are related by second order transformations. The structural relationships between the various phases are discussed below and also summarised in Table 5-1 for clarity.

**Table 5-1 Summary of the different $WO_3$ reported in the literature and the structural changes between them**

| Temp(°C) | S. Group | Octahedral tilting and W displacements | Supercell | Tilts |
|---|---|---|---|---|
| | $Pm\bar{3}m$ | | 1x1x1 | $a^0a^0c^0$ |
| | ↓ | No tilt, W displacement | | |
| Above 900 | *P4/nmm* | | √2x√2x1 | $a^0a^0c^0$ |
| | ↓ | Tilt, no W displacement | | |
| 790 to 900 | *P4/ncc* | | √2x√2x2 | $a^0a^0c^-$ |
| | ↓ | Tilt, no W displacement | | |
| 760 to 790 | $P2_1/c$ | | √2x√2x2 | $a^-a^-c^-$ |
| | ↓ | Tilt, W displacement | | |
| 400 to 760 | *Pcnb* | | 2 x 2 x 2 | $a^0b^+c^-$ |
| | ↓ | Tilt, *no* W displacement | | |
| 17 to 400 | $P2_1/n$ | | 2 x 2 x 2 | $a^-b^+c^-$ |
| | ↓ | Tilt, W displacement | | |
| -40 to 17 | $P\bar{1}$ | | 2 x 2 x 2 | $a^-b^-c^-$ |
| | ↓ | No tilt, W displacement | | |
| below -40 | *P*c | | √2x√2x2 | $a^-b^-c^-$ |

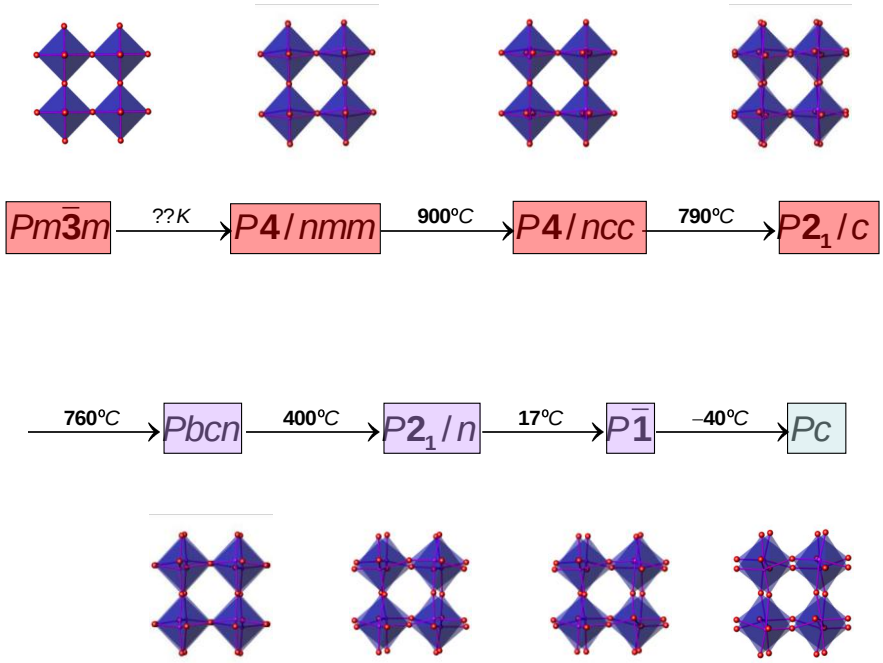


**Figure 5-2 Schematic representation of the phase transitions occurring in $WO_3$. Phases related by a second order phase transitions are represented by similar colours. The phases found between 760 °C and 1000 °C, between -70 °C and 760 °C and below -70 °C are represented in red, purple and blue boxes respectively.**

Studies of $WO_3$ at high temperature were started in 1953 by Kehl[(1)] who described for the first time the existence of a tetragonal *P*4/*nmm* phase at high temperature. This phase is the highest temperature/symmetry form reported so far and exists above 900 °C[(2),(3)]. This tetragonal structure was described to differ from the ideal $ReO_3$ structure only by displacement of the W atoms alternatively parallel and anti-parallel to the z-axis, with no tilting of the octahedra associated with the transition. When the temperature is lowered to 827 °C, a second tetragonal phase whose structure was determine by neutron diffraction[(4)] appears. This structure (often referred as the $\alpha$-phase) belongs to the *P*4/*ncc* space group and is generated from the *P*4/*nmm* phase by a tilt of the $WO_6$ octahedra around the c-axis. As this octahedral tilt only slightly displaces the oxygen atoms without modifying the tungsten positions, X-ray studies by Kehl could not differentiate between these two tetragonal phases.

In 2002, Howard et *al.*[(3)] reported for the first time the presence of a monoclinic $P2_1/c$ phase between 790°C and 720°C that had previously been overlooked due its very small temperature range of existence. This *P*4/*ncc* to $P2_1/c$ transition only involves a tilting of the octahedra. As the temperature is further decreased down to 350 °C[(3, 4)], the $P2_1/c$ phase evolves into a orthorhombic *Pbcn* phase. The $P2_1/c$ to *Pbcn* transition shows sudden discontinuities in cell parameters suggesting a first order phase transition. This first order change is consistent with the group-subgroup relationship between those two space groups shown in Figure 5-2[(3)].

These latest investigations on high and room temperature phases of $WO_3$ described by Howard et *al.*[3] provided a picture of the phase transitions occurring in $WO_3$ between 1000 °C and room temperature. Figure 5-3 shows the stability range of each phase and the evolution of the cell parameters as a function of temperature taken from their paper. The temperatures at which structures had been determined earlier by Vogt et *al.*[4] are shown by orange dotted lines.

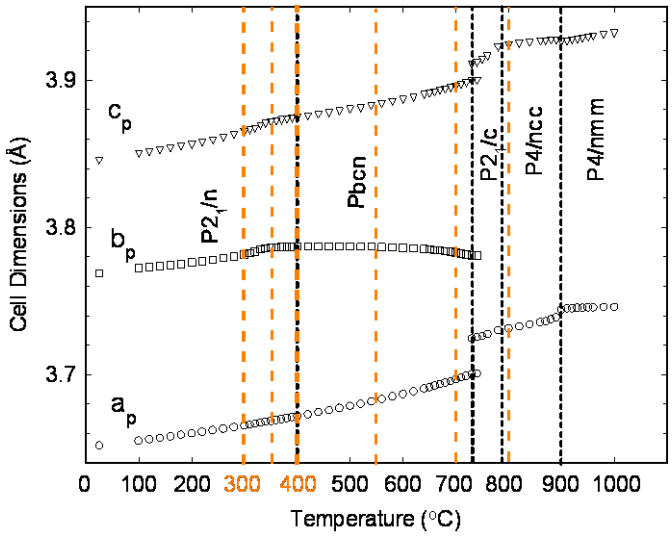


**Figure 5-3 Evolution of the cell parameters of $WO_3$ between room temperature and 1000°C extracted from reference 3. The black dotted lines show the phase transition temperatures and the orange lines show the temperatures at which the structures have been reported in reference 4.**

Figure 5-3 also shows that a second order phase transition occurs at 400 °C where the structure evolves from a *Pbcn* to a monoclinic $P2_1/n$ symmetry that remains until room temperature. The details of the $WO_3$ structure at room temperature by X-ray investigations are, however, controversial.

In 1931, Braekken was the first to present a structure for the room temperature form of $WO_3$ from single crystal data and described it as triclinic. However, some twenty years later, Andersson[5] argued that the W positions described by Braekken could be as well described using a $P2_1/a$ monoclinic structure. In 1959, polarising microscope cooling experiments on single crystal by Tanisaki[6] described a continuous phase transition propagating across the crystal on cooling from 17 °C leading to a triclinic structure. In later powder neutron diffraction studies, Woodward discussed further the monoclinic to triclinic transition[7]. The monoclinic phase was described to be stable above 25 °C and to convert into the triclinic form when the sample is cooled below room temperature. As a cooled sample remains into this form when heated back to room temperature, Woodward concluded that the real thermodynamically stable form at room temperature is more likely to be the triclinic form than the monoclinic one. At room temperature, $WO_3$ can therefore be found in two stable forms depending on its thermal history.

When looking at the structural differences between these two room temperature phases, Woodward *et al.*[7] noted that both show similar tilts of the octahedra along the x and z axis. However, these tilts are

out of phase for the triclinic phase and in-phase for the monoclinic phase when looking along the y axis and the phases can therefore be described to belong to $a^+b^-c^-$ and to $a^-b^-c^-$ tilt systems in the Glazer notation[(8)a]. However, these tilts and the unit cell parameters obtained experimentally were only consistent with $P2_1/m$ and $F\bar{1}$ respectively from Glazer's paper. These two space groups are different from the ones obtained by refinement. The differences in symmetry are due to the occurrence of an additional displacement of the W atoms within the octahedra in addition to the tilting. In both systems, the W displacement is towards one edge of the octahedra leading to two short, two long and two intermediate W-O bond lengths.

The second first order phase transition of the series involves the final transformation of the structure into a low temperature *Pc* (monoclinic) phase. This phase was first observed in early studies by Tanisaki to occur around -40 °C. A similar phase transition occurring at -50 °C was described by Matthias[(9)] who commented that small variations in the crystal composition can induce wide variations in the phase transition temperature. This second low temperature phase was refined for the first time by Woodward[(10)] and confirmed to be ferroelectric by high resolution neutron powder diffraction data. The structural changes occurring over the $P\bar{1}$ to *Pc* (reported as $\delta$ and $\varepsilon$ phases respectively) phase transition were found to be slightly different from the other ones occurring in $WO_3$. All the higher temperature transitions correspond to a lowering of symmetry and involve the tilting of octahedra (accompanied or not by off centre movements of W atoms). In the final transition, the symmetry can either be regarded as increasing as the material goes from triclinic to monoclinic or as a lowering of symmetry as it corresponds to an evolution from a centric to an acentric structure. Moreover, unlike all the previous transitions, the tilts of the $\delta$ and $\varepsilon$ phases (regardless of their magnitudes) are the same ($a^-b^-c^-$). The two phases therefore differ only by the off-centering of the W atoms in the xy plane.

Thermal history is also known to be very important for the $P\bar{1}$ and *Pc* transition. For example in the work of Woodward, diffraction patterns at 200 K revealed the presence of at least two phases but attempts refining the data only with a mixture of $P\bar{1}$ and *Pc* phases were not successful. This might be because at this temperature, some of the $P2_1/n$ phase was still present which would be consistent with the observations by Tanisaki about the nature of the $P2_1/n$ to $P\bar{1}$ phase transition. At 15 K, refinement of the neutron and synchrotron X-ray powder patterns suggested predominantly a *Pc* single phase however the presence of a small amount of another phase was observed. The lattice constants of this unknown phase seemed to evolve smoothly towards those of the $P\bar{1}$ phase as the temperature increased but attempts at solving this structure have not been reported.

The investigation of the different phases as the temperature varies has been a matter of a significant number of investigations and controversies. We describe here how combination of powder diffraction,

[a] In perovskite structures, the rotation of an octahedron around a given axis is noted a, b or c. Rotation with identical magnitudes are denoted by the same letter. If the octahedra in adjacent layers tilt in the same direction the rotation is represented with a + superscript, a tilt in the opposite directions is represented with a – superscript (+ in phase, – out of phase).

$^{17}$O NMR and DFT calculations can potentially elucidate some of these controversies and bring new structural insights into its studies.

## 5.2. Simulations of the $^{17}$O MAS spectra of $WO_3$ phases

In the following work, we will be showing how NMR in combination with DFT calculations can potentially provide new information on controversial structures such as $WO_3$. The low sensitivity ($7.20 \times 10^{-4}$ for $^{31}$P and $1.59 \times 10^{-2}$ for $^{13}$C) and the large quadrupole interactions of the tungsten nucleus make it not well suited for NMR studies. The sensitivity of $^{17}$O is significantly larger ($2.91 \times 10^{-2}$ for $^{17}$O). However, its low natural abundance (0.037%) usually requires enrichment of the samples.

As discussed above, $WO_3$ undergoes a series of phase transitions on cooling from high temperature. It is interesting to look at the expected NMR behaviour of all the structures reported in the literature. We therefore calculated the NMR parameters for $^{17}$O in the seven different $WO_3$ phases using CASTEP and present the corresponding simulated MAS spectra in Figure 5-4.

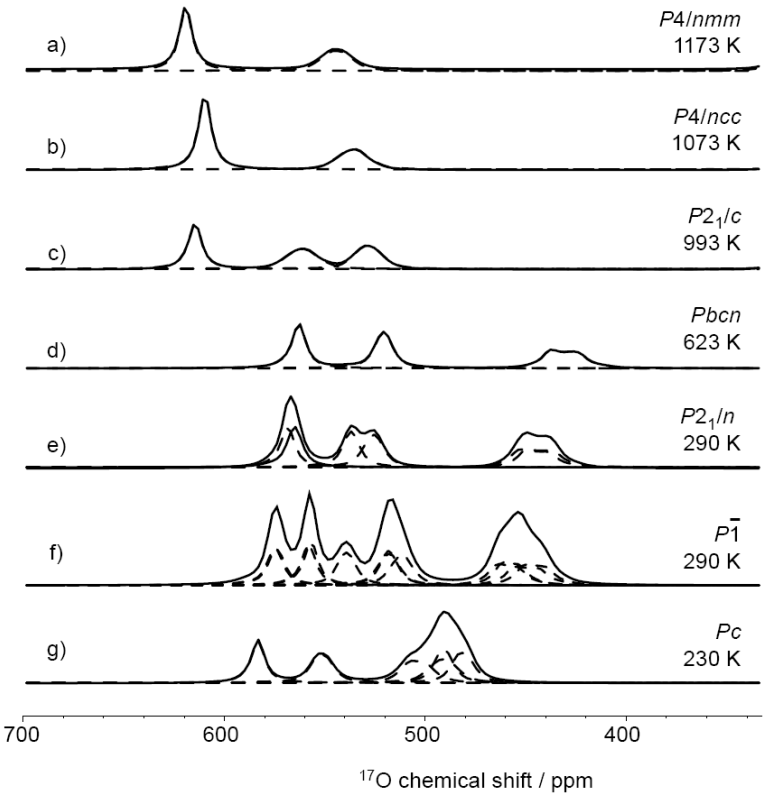


**Figure 5-4 MAS NMR spectra of the different phases of $WO_3$ simulated for a spinning speed of 20 kHz and a line broadening of 500 Hz (based on realistic line widths obtained from experimental data) calculated using CASTEP software package. Spectra a), b) c), d) and e), f), g), h) were calculated using coordinates from reference 3 and reference 10 respectively. The dotted lines show the contour of each individual $^{17}$O site while the full line is the sum of all the $^{17}$O sites and therefore the expected NMR signal.**

It is immediately clear from Figure 5-4 that $^{17}$O NMR is potentially very sensitive to subtle changes in the $WO_3$ structure. This work aims to exploit the information provided by these calculations, it is then crucial to first verify the reliability of these calculations to reproduce experimental data. MAS NMR

experiments can typically be performed between 120 K and 250 K, therefore, only the three lower temperature phases ($P2_1/n$, $P\bar{1}$ and $Pc$) are in principle observable with standard NMR equipment.

### 5.2.1. $^{17}$O solid-state NMR

A $^{17}$O enriched sample of $WO_3$ was previously synthesised by Allen[11] (SA82A) and was used for preliminary studies on the NMR behaviour of $WO_3$ at room and low temperatures.
Considering the observations reported in the literature at least three phases exist close and below room temperature (see section 5.1.1), we aimed to observe these three phases by $^{17}$O NMR to confirm the sensitivity of NMR to structural changes. Figure 5-4 suggests that the occurrence of these transitions should have a noticeable effect on the $^{17}$O NMR spectrum.

The $^{17}$O MAS NMR spectrum of SA82A recorded at 300MHz was previously reported and discussed by King[12]. We recorded a new $^{17}$O spectrum on the same SA82A sample on a 500 MHz Varian spectrometer using a frequency of 67.77 MHz. The sample was packed in a 4 mm zirconia rotor and span at 17 kHz. The resulting spectrum is presented in Figure 5-5a). The three resonances observed in the experimental spectra were attributed to the three pairs of oxygen sites present in the monoclinic phase and a rather speculative assignment based on asymmetry of the W-O bonds around the oxygen atoms was proposed by King[12].

Figure 5-5 also contains four simulations of the NMR spectrum based on the $P2_1/n$ structural models discussed below. For each simulation calculated spectra were referenced to experimental by adjusting the individual mean of 271 ppm shifts. The first conclusions we can reach is that the calculated spectra show good agreement with the experimental, confirming we have a $P2_1/n$ sample and allowing the assignment of the experimental spectrum.

The simulations in Figure 5-5 b-e have come from different structural models in the literature. One structure reported by Howard et *al*.[3] was obtained using high resolution neutron powder diffraction data while work published by Woodward *et al.*[7] used lower resolution data on a mixture of $P2_1/n$ and $P\bar{1}$ $WO_3$. Interestingly in the Woodward[7] study sets of coordinates using two different Rietveld refinement packages (GSAS[13] and PROFILE[14]) were reported. The authors obtained better agreement factors using GSAS and concluded tentatively that the resulting structural model would be more reliable, but had no independent check of this conclusion. Geometry optimisations in CASTEP were carried out starting from each of the reported structures. Each converged to essentially the same minimum and the calculated NMR spectrum is included in Figure 5-5 e).

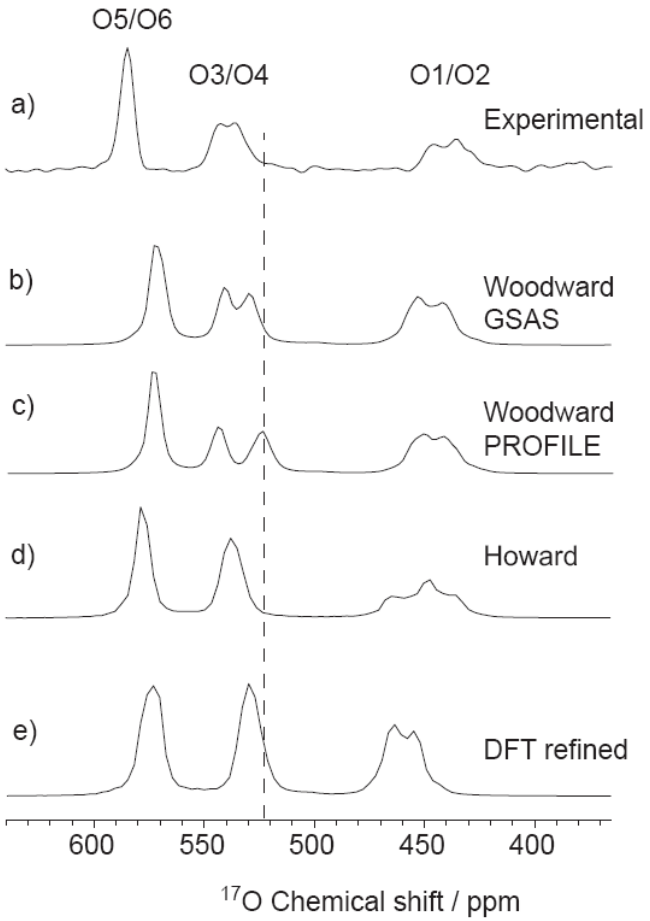


**Figure 5-5 Comparison of the room temperature MAS NMR spectra of $WO_3$ a) and the simulated spectra of different structures of monoclinic $WO_3$ reported in the literature calculated using the CASTEP software package b)-e).**

Although small differences are obvious between the different calculated NMR patterns, all the spectra show good agreement with the experimental data. Each can be separated into three sets of $^{17}O$ signals agreeing with the assignment proposed earlier by King[(12)]. The spectra in Figure 5-5 and the structural information presented in Table 5-2 let us make some comments about the various published models. The spectrum calculated from the most recently published Howard model, Figure 5-5 d), shows an unusual lineshape for the O1/O2 resonance. This is a consequence of a significant difference in calculated isotropic shifts for O1 and O2 (~19 ppm), which combines with the second-order quadrupole broadening to give the overall lineshape observed. Moreover, the chemical shift difference between O3 and O4 (~3.7 ppm) appears slightly underestimated for this structure. The calculated spectra derived from the Woodward refinements however resemble the observed NMR data more closely. In his paper, Woodward suggests the GSAS model as more reliable than the PROFILE one. Our calculations performed on the latter clearly over-estimate the chemical shift difference between O3 and O4. The simulated spectrum obtained from the GSAS model however is more similar to our experimental data. Such observation is consistent with the suggestion made by Woodward that this model is the more reliable.

**Table 5-2 Average bond distances, asymmetry in the W-O bond lengths, calculated $^{17}O$ shifts and quadrupolar coupling using the *P*$2_1$/*n* structures of $WO_3$ reported in reference 7 (GSAS and PROFILE refinement)and 3 and those from DFT geometry optimisation of this structure.**

| | GSAS | | | | PROFILE | | | |
|---|---|---|---|---|---|---|---|---|
| | $d_{av}$(Å) | Δd (Å) | $\delta_{iso}$ (ppm) | $C_Q$ (MHz) | $d_{av}$ (Å) | Δd (Å) | $\delta_{iso}$ (ppm) | $C_Q$ (MHz) |
| W2-O1-W1 | 1.898 | 0.026 | 200.3 | -3.371 | 1.904 | 0.010 | 196.3 | -3.368 |
| W2-O2-W1 | 1.897 | 0.026 | 196.5 | -3.327 | 1.899 | 0.049 | 191.7 | -3.354 |
| W1-O3-W1 | 1.936 | 0.280 | 279.9 | -1.589 | 1.939 | 0.345 | 279.8 | -1.619 |
| W2-O4-W2 | 1.933 | 0.264 | 270.1 | -1.825 | 1.93 | 0.332 | 262.0 | -1.878 |
| W2-O5-W1 | 1.960 | 0.375 | 309.7 | -1.131 | 1.961 | 0.458 | 307.2 | -0.992 |
| W1-O6-W2 | 1.961 | 0.373 | 306.9 | -1.304 | 1.95 | 0.405 | 305.7 | -1.119 |

| | Howard | | | | DFT optimised | | | |
|---|---|---|---|---|---|---|---|---|
| | $d_{av}$(Å) | Δd (Å) | $\delta_{iso}$ (ppm) | $C_Q$ (MHz) | $d_{av}$(Å) | Δd (Å) | $\delta_{iso}$ (ppm) | $C_Q$ (MHz) |
| W2-O1-W1 | 1.909 | 0.023 | 201.1 | -3.444 | 1.898 | 0.027 | 216.3 | -3.077 |
| W2-O2-W1 | 1.882 | 0.015 | 182.2 | -3.102 | 1.897 | 0.028 | 214.4 | -3.044 |
| W1-O3-W1 | 1.936 | 0.318 | 270.4 | -1.733 | 1.936 | 0.291 | 280.0 | -1.815 |
| W2-O4-W2 | 1.929 | 0.343 | 266.7 | -1.756 | 1.934 | 0.272 | 277.4 | -2.084 |
| W2-O5-W1 | 1.960 | 0.447 | 306.9 | -1.003 | 1.958 | 0.372 | 316.9 | -1.286 |
| W1-O6-W2 | 1.949 | 0.411 | 304.6 | -1.178 | 1.959 | 0.370 | 322.6 | -1.473 |

The origins of the difference in chemical shift and quadrupolar coupling ($C_Q$) for the various models can be related to structural features such as W-O bond lengths an the asymmetry of the W-O-W linkages. These details are presented in Table 5-2 and will be discussed in section 5.4.

These results confirm the accuracy of both the CASTEP calculations and the description of the *P*$2_1$/*n* structure at room temperature. Similar investigations on the $P\bar{1}$ and *Pc* phases, also been reported by Woodward, can then be performed using $W^{17}O_3$ sample.

## 5.3. Low temperature investigations

A series of NMR and X-ray experiments have been performed on different samples to probe the *P*$2_1$/*n* to $P\bar{1}$ to *Pc* structural transitions.

### 5.3.1. NMR studies on SA82A $W^{17}O_3$

$^{17}O$ MAS NMR low temperature experiments were carried out on a 500 MHz Varian spectrometer using a frequency of 67.77 MHz. The sample was packed in a 2.5 mm zirconia rotor and spun at 15 kHz. Low temperatures were reached and controlled by blowing gas cooled through a liquid nitrogen dewar and adjusted by a thermostat heater. Our standard solid-state NMR equipment typically allows samples to be studied between 123 K up to 523 K. Considering earlier published studies, one should therefore be able to observe the three low temperature phases with such

equipment. The longest $T_1$ relaxation time was found for the signal appearing at 580 ppm and was as ~55 s. All following experiments were therefore acquired using 16 scans separated by a pulse delay (pd) of 256 s in order to allow the system to relax. The data were consistently processed using a line broadening of 300 Hz.

The $^{17}O$ NMR spectra at 293 K and 183 K of the SA82A $W^{17}O_3$ enriched sample are shown in Figure 5-6.

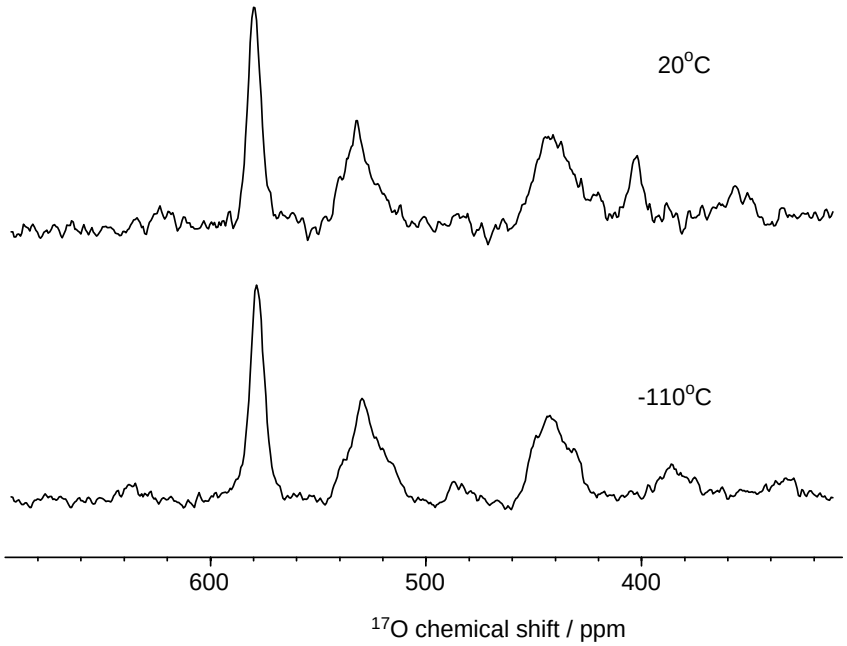


**Figure 5-6 $^{17}O$ MAS NMR spectra recorded on sample SA82A using a 4 mm zirconia rotor with temperatures set at 20 °C and -110 °C and spinning speeds of 12 kHz and 13 kHz respectively showing the presence of the *P*$2_1$/n phase at room temperature.**

When cooling our sample down to -110 °C, no phase transition is observed on our NMR data. In order to understand this and have an idea on the temperatures where the low temperature phase transitions occur, X-ray experiments on our SA82A enriched sample were performed.

### 5.3.2. Variable temperature X-ray experiments on SA82A $W^{17}O_3$

Powder X-ray diffraction experiments were performed on a Bruker d8 Advance diffractometer using a Cu $K_{\alpha 1}$ / $K_{\alpha 2}$ radiation source with average wavelengths of 1.540596 Å and 1.544493 Å respectively. The samples were mounted onto zero background silicon slides using Vaseline. The low temperature experiments were performed using an Oxford cryosystems Phenix closed cycle helium cryostat allowing samples to be cooled down to 11 K. All the X-ray data were acquired for $2\theta$ angle values between 10 ° and 115 °. Each data set was acquired with a step size of 0.008 °and a count time of steps of 0.09 s per step as the sample is continually cooled. The data collection time and cooling rate (6 K / hr) means each successive pattern correspond to a temperature change of ~2 K.

In order to visually observe the occurrence of the phase transitions, the relative intensities of selected diffraction regions obtained from our X-ray data are represented at the experimental temperatures on

a 2D plot. Selected portions of the X-ray data acquired between 300 K and 16 K using a cooling rate of 6 K / hr are shown in Figure 5-7.

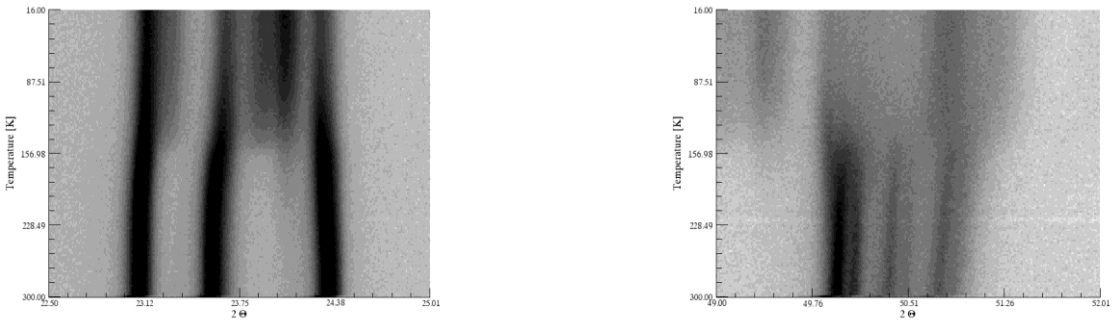


**Figure 5-7 Selected portions (22.5 °<2$\theta$<25 °and 49 °<2$\theta$<52 °) of the X-ray data acquired on SA82A between 300 K and 16 K using a cooling rate of 6 K / hr**

A marked change in diffraction data corresponding to the formation of the *Pc* phase at 150 K is immediately obvious. However, since the $P2_1/n$ and $P\bar{1}$ structures are closely related, it is less straightforward to determine where the $P2_1/n$ to $P\bar{1}$ transition occurs in this sample. This can however, potentially be determined by quantitative Rietveld refinement of each dataset using a three phase model. Such refinements are by no means straightforward as the patterns of the three phases present are extremely similar. This means that it is extremely easy to fall into false minimum during the refinements. In fact, one invariably finds that, due to the higher number of structural parameters a $P\bar{1}$ model can fit a true $P2_1/n$ containing diffraction pattern better than the correct $P2_1/n$ structure.

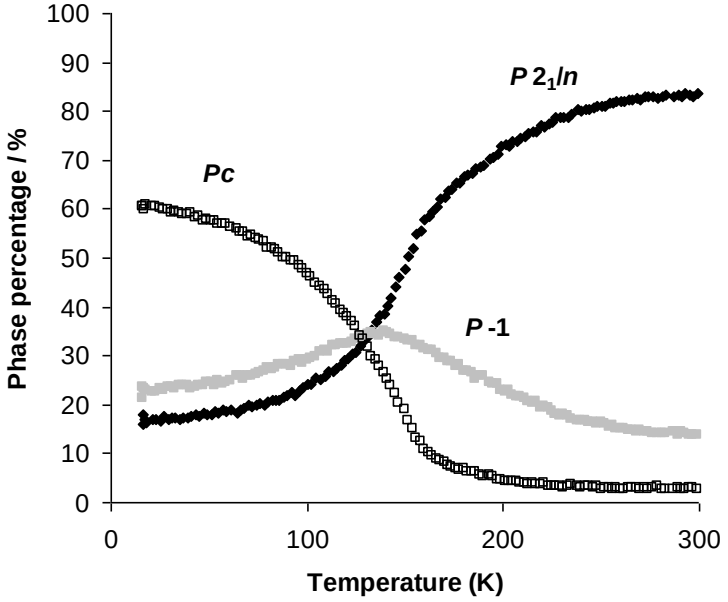


**Figure 5-8 Results of the refinement of the variable temperature (cooling from 300 K to 16 K) powder pattern of Simon Allen's enriched sample (d9_03051). The full, empty and grey data points correspond to the evolution of the $P2_1/n$ (monoclinic), $P\bar{1}$ (triclinic) and *Pc* (monoclinic) phases respectively.**

For all refinements, we have therefore used a surface fitting approach[15] devised by J.S.O. Evans in which all the diffraction data are fitted simultaneously to a model in which cell parameters must evolve smoothly with temperature. This ensures that the fit makes physical sense not only for each individual data but for the entire ensemble of diffraction data. The input file used is included in Appendix and the phase fraction results are shown in Figure 5-8.

These X-ray results show why no changes were observed in the NMR data. A significant amount of the low temperature phases is not formed until about -140 °C. It is likely that the temperature of the sample (due to frictional heating induced by spinning) is well above this value.

For this and later studies, we will define the temperature at which the *P*c phase appears using a parameter $T_{50}$, the temperature at which the *Pc* phase fraction reaches 50% of its final value. For this sample, the final percentage of *Pc* phase is 60.5 %, therefore $T_{50}$=132 K which corresponds to the temperature where 30.2 % of the *Pc* phase ispresent. The temperatures found are well below those that has previously been described in the literature where the $P\bar{1}$ and the *Pc* forms was predominant at 233 K (-40 °C) and 203 K (-70 °C) respectively.

The slow transformation of this sample may be due to the synthetic route employed by Allen described in section 3.3.3. In this synthetic route, the sample was heated in a tube furnace at 1223 K for one hour and quickly cooled down to avoid $^{17}O/^{16}O$ exchange between the sample and air. We therefore decided to investigate the influence of different cooling rates on the low temperature phase transitions initially using unenriched $WO_3$ sample.

### 5.3.3. X-Ray studies on unenriched samples

Two samples were prepared by grinding 5 g of $WO_3$ (Alpha Aesar, 99.8% pure) with an agate mortar and pestle and heating in an platinum crucible. For the first sample, the powder was heated in air to 1000°C over 4 hours and cooled at a rate of 10 K/min (AS027) from 1273 K to 298 K. For the second sample, the sample underwent the same heating treatment but was cooled slower, at a rate of 0.25 K / min (AS028). 150 X-ray scans at temperatures ranging from 300 K to 16 K were recorded. The data are shown in Figure 5-9.

a) b)

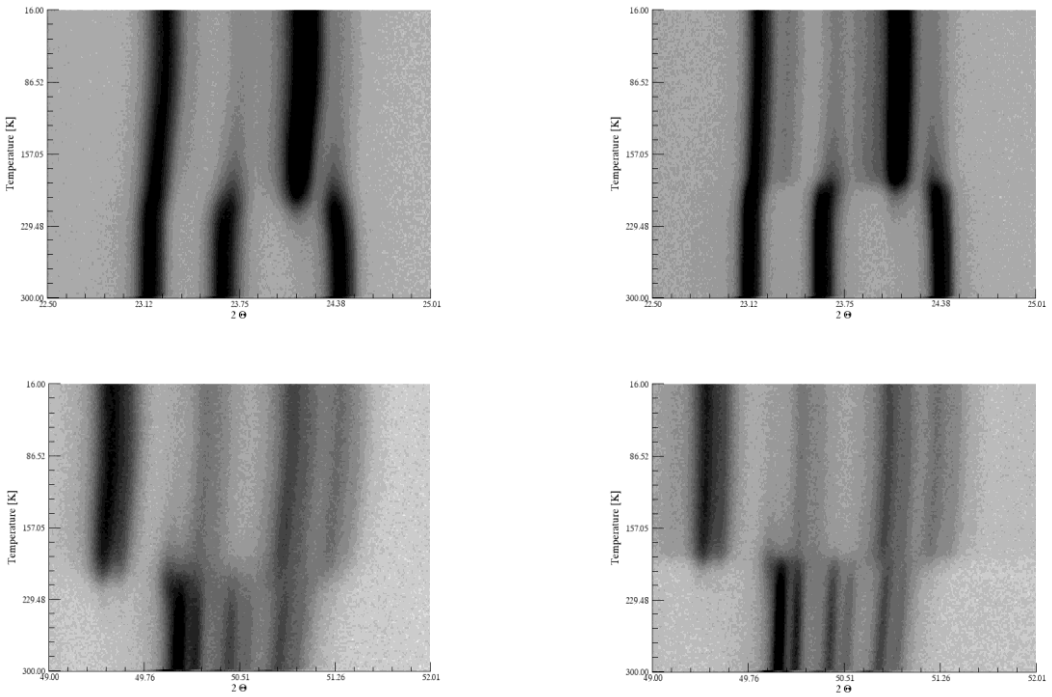


c)

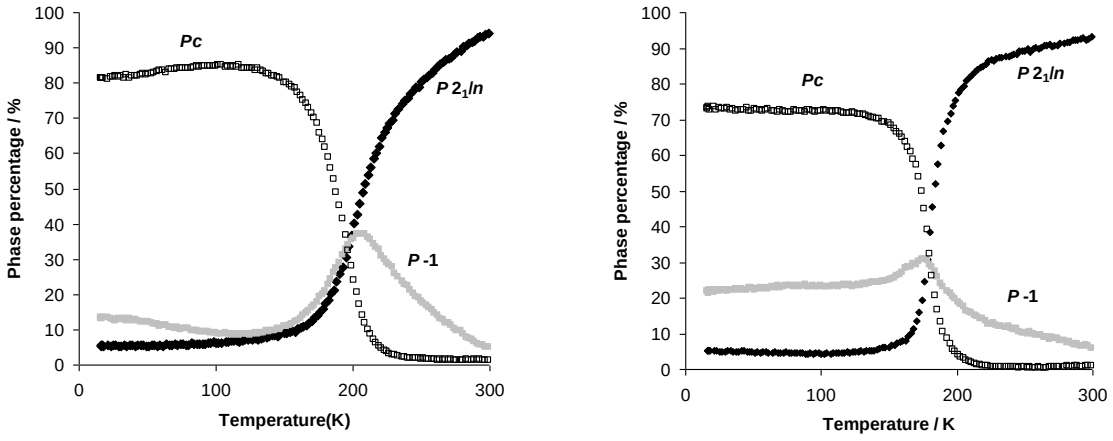


**Figure 5-9 a),b) Selected portions (22.5°<2θ<25°and 45°<2θ<52°) of the X-ray data acquired and c) results of the refinement of the variable temperature (cooling from 300 K to 16 K) powder patterns of AS027 (left) and AS028 (right) unenriched samples experiments (d9_03147 and d9_03151). The full, empty and grey data points correspond to the evolution of the *P*2$_1$/n (monoclinic), *P*$\bar{1}$ (triclinic) and *Pc* (monoclinic) phases respectively.**

The different cooling rates employed on our sample have noticeable effects on the phase transitions. First the 2D plots show that the peaks are considerably narrower for the sample obtained using a slower cooling rate (AS028). For this sample, clear diffraction peaks also appear $2\theta$ angles of 23.4°, 24.0° at low temperature and suggest that a phase distinct from the *Pc* one is also present below 160 K.

The phase fraction plots shown are derived using only the three low temperature structures reported in the literature. The apparent high phase fraction of the $P\bar{1}$ structure at low temperature for AS028 is compensating for the presence of this extra phase.

For AS027 and AS028, the $T_{50}$ values were 192 K and 179 K respectively. The cooling rates employed in both of these syntheses were slower than the one used by Simon Allen and led to the displacement of the $T_{50}$ towards higher temperatures. However, although AS027 was cooled more slowly than AS028, its $T_{50}$ value is slightly lower. Although these two $T_{50}$ values are within the range of what can be observed using our NMR equipment, attempt to record variable temperature experiments on these unenriched samples would have been vain due to the low $^{17}O$ natural abundance. However, these results were encouraging and the synthesis of new enriched samples with controlled cooling rates was performed.

### 5.3.4. Synthesis and studies of enriched $WO_3$ samples

The enrichment route of our $WO_3$ sample was based on the procedure previously described by Simon Allen[(11)]. 2.266 g of $WCl_6$ (Alfa Aesar, 99%) were weighed in a glove box. The powder was then dissolved in 30 ml of dry ether leading to a very dark green solution. When 0.972 g of $H_2{}^{17}O$ was added (a 9:1 $H_2O$ to $WCl_6$ molar ratio), a deep navy blue precipitate was observed (in our synthesis, we observed an deep orange intermediate precipitate not mentioned by Allen turning into dark blue after overnight stirring). After overnight stirring, the ether is evaporated under vacuum using a pre-trap and 1.610 g of a shiny dark blue powder was recovered. In order to remove the chlorine residuals, the sample was heated under vacuum in a tube furnace at 10 K/min to 1173 K for 3 hours. X-ray diffraction on the recovered shiny dark solid (1.176 g) was shown to be $WO_{2.72}$ ($W_{18}O_{49}$ described by Magneli). The powder was then reground and oxidised in air in a tube furnace by heating for 1hr at 1223 K after warming at 10 K/min.

The slow cooling of the sample was performed by sealing the resulting powder in a quartz tube under air and heating it in a furnace at 1223 K for 3 hours. For our first sample, AS026B, the sample was cooled down to room temperature at 0.1 K / min. 1.183 g of a bright yellow powder was obtained (88% yield) and confirmed by X-ray and MAS NMR experiment to be the monoclinic phase of $WO_3$.

Both X-ray diffraction and $^{17}O$ NMR experiments at low temperature were performed on this sample. The results obtained from X-ray diffraction on cooling are shown in Figure10 a) and the low temperature NMR experiments are shown in Figure 5-11.

a)

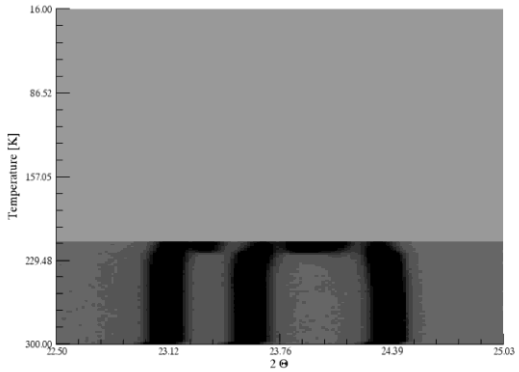


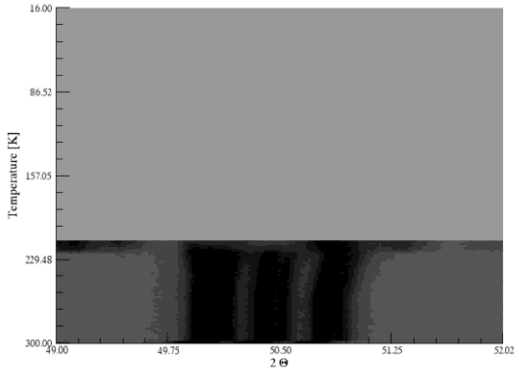


b)

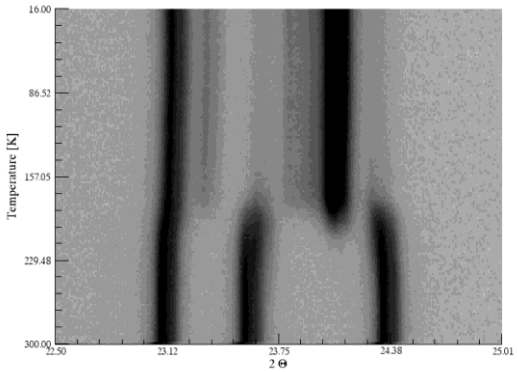


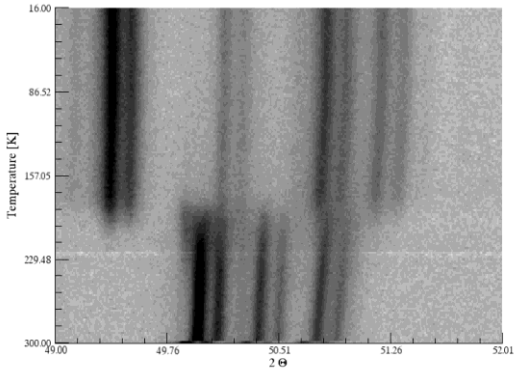


c)

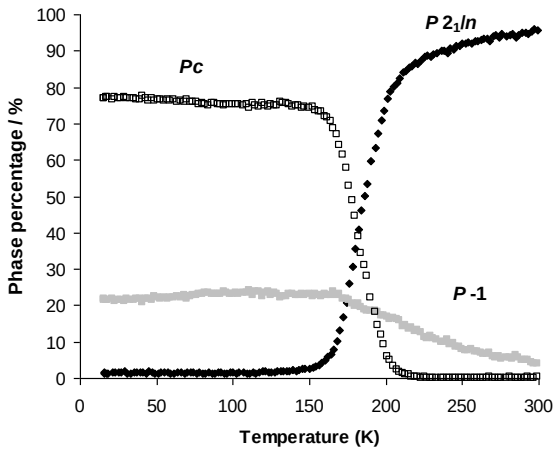


**Figure 5-10 a),b) Selected portions (22.5 °<2$\theta$<25 °and 49 °<2$\theta$<52 °) of the X-ray data acquired and c) Results of the refinement of the variable temperature (cooling from 300 K to 16 K) powder pattern of AS026B (left) and AS026C (right) enriched sample experiments (d9_02979 and d9_03124 respectively). The full, empty and grey data points correspond to the evolution of the *P*2$_1$/n (monoclinic), *P*$\bar{1}$ (triclinic) and *Pc* (monoclinic) phases respectively.**

Due to a failure in our equipment and the limited amount of sample, we have not been able to perform X-ray experiments on AS026B at temperature lower than 209 K. However, we can still comment on the results. From the limited data we have, the $T_{50}$ in AS026B is expected at about 173 K. However, the $^{17}$O MAS NMR spectra recorded at 13 kHz with the temperature controller set to 163 K did not

show any phase transition. This can again be explained by the fact that while spinning, the sample is heated up and therefore the actual temperature of the sample is higher (around 10 K more for this temperature and spinning speed) than the one displayed on the control panel.

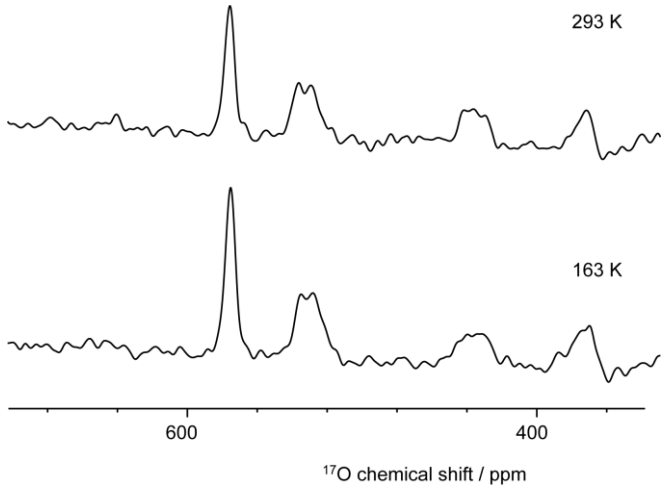


**Figure 5-11 $^{17}$O MAS spectra of AS026B recorded for a spinning speed of 13 kHz on a 500 MHz Varian spectrometer using a frequency of 67.77 MHz.**

Considering the effect of the cooling rate on the phase transition temperature shown previously on our unlabelled sample, we decided to reheat AS026B for 3 hours in a sealed quartz tube and recool it at a slower rate of 0.04 K / min to see if we observe the phase transition to occur at higher temperature. The powder 3D plot of the variable temperature X-ray data are shown in Figure 5-10 b) (AS026C).

While looking at AS026C diffraction patterns, and compare them with AS026B, we can see that the phase transitions occur at approximately the same temperatures. However, the peaks are much narrower in the AS026C sample. Two important conclusions can be made. Firstly, AS026C shows sharper diffraction peaks than AS026B suggesting a more crystalline sample. Secondly, the variable temperature Rietveld analysis shows clearly that the low temperature *Pc* phase should be accessible by $^{17}$O NMR experiments.

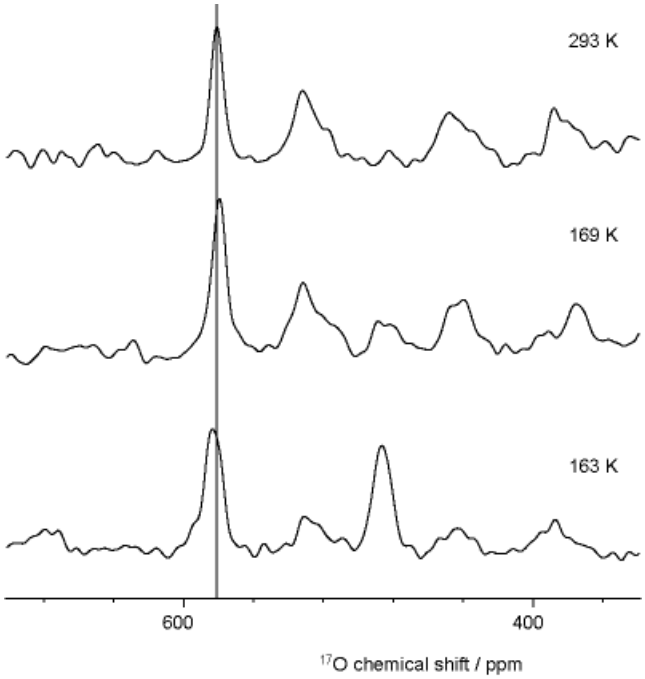


**Figure 5-12 $^{17}$O MAS spectra recorded during variable temperature experiment performed on AS026C for a spinning speed of 13 kHz on a 500 MHz Varian spectrometer using a frequency of 67.77 MHz.**

Figure 5-12 shows the NMR data for AS026C. A clear peak appears at 520 ppm as the temperature is lowered. The peak is almost indistinguishable from the noise level at 169 K but becomes significant at 163 K. Two of the resonances present at room temperature also disappear over this range of temperature. These observations suggest that the appearence of the new phase occurs simultaneously with the disappearance of the room temperature phase. Looking at our different variable temperature refinements, such behaviour occurs between the $P2_1/n$ and the *Pc* phases. Therefore, the $^{17}$O NMR spectra observed here probably corresponds to the *Pc* phase. The non observation of the $P\bar{1}$ phase in the NMR spectra can be explained by the relative small amount of this phase that is ever present in this range of temperature. However, previous studies (and some of our data on AS026B not presented here) reveal that the triclinic phase is the room temperature form of $WO_3$ when the sample is heated back from an undetermined (yet) low temperature. We can therefore propose later studies where an enriched sample can be cooled down to low temperature and the NMR spectra of the $P\bar{1}$ structure determined at room temperature. The calculated patterns presented in Figure 5-4 also support the fact that the *Pc* phase forms. The bottom spectrum in Figure 5-12 suggest that at 163 K, most of the $P2_1/n$ phase is converted into the *Pc* phase with only small residual signals appearing at about 440 ppm and 520ppm. The signal at 580 ppm is mostly due to the oxygens of the *Pc* phase. The poor signal to noise ratio doesn't allow an accurate integration of the signals, however, a rough approximation of these intensities suggests a 3:1 proportion of the *Pc* phase relative to the $P2_1/n$ phase at 163 K.

## 5.4. Correlations between structure and NMR spectra using DFT calculations

As mentioned in section 5.1.1, seven phases of $WO_3$ have been described in the literature. Using the reported crystal structures and CASTEP calculations, the NMR spectra were simulated and shown in Figure 5-4. The simplicity of the $WO_3$ stoeichiometry makes it an interesting candidate for preliminary investigations of the effects of structural changes on different NMR parameters provided by CASTEP calculations.

### 5.4.1. Room temperature $^{17}$O MAS spectrum studies

The individual $^{17}$O isotropic chemical shifts and the quadrupole coupling values obtained via our calculations, the average W–O distances ($d_{av}$), the asymmetry (difference in O–W bond lengths around a given oxygen defined as $\Delta d = |d_1 - d_2|$) are listed in Table 5-2.

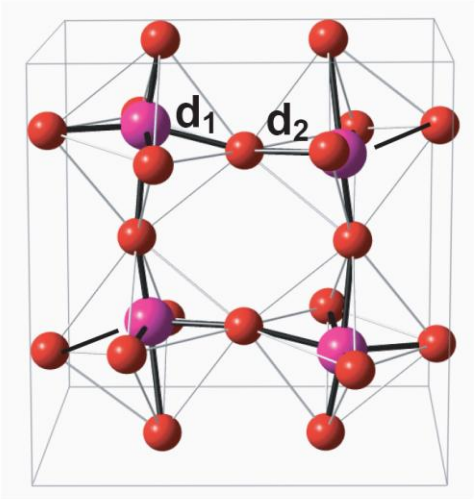


**Figure 5-13 Schematic representation of the $WO_6$ arrangement on *P*2$_1$/*n* $WO_3$ structure showing the $d_1$ and $d_2$ distances and the expressions of the average bond distance ($d_{av}$) and asymmetry ($\Delta$d) around a given oxygen.**

The good agreement of our calculations to the experimental data shown in section 5.2 allows us to investigate further how to relate NMR to structural parameters. Looking more closely at the data given by Table 5-2, we notice an overall tendency of the isotropic chemical shift values to increase with the asymmetry ($\Delta$d) as well as with the average W-O bond distance around a given oxygen site. The O1 and O2 sites lie in the most symmetrical local environment and are assigned to the lowest chemical shifts values which correspond to the broad overlapped resonances at 440 ppm. The O3 and O4 sites, with longer average distances and a much larger local asymmetry appear in the intermediate chemical shift range (peaks at 540 ppm). Finally O5 and O6 which have a longer still average distance and still higher asymmetry correspond to the peaks at ~590 ppm. The quadrupole couplings show analogous trends with $C_Q$ (O1/2) > $C_Q$ (O3/4) > $C_Q$ (O5/6). The apparent splitting in the O1/2 peak of Figure 5-5 is not the result of a resolution of O1 and O2 sites but a strong second order broadening from the larger quadrupole interaction. The O3–O6 peaks show less noticeable quadrupolar broadening. The differences between the simulated spectra suggest that the NMR parameters are extremely sensitive

to very subtle structural changes. The DFT optimised structure (Figure 5-5 e)) doesn't seem to give better agreement than any of the other structures.

The easiest NMR parameters to observe experimentally are the isotropic chemical shift and the quadrupolar coupling constant. We investigate here how these two are influenced by structural changes. The correlation plots between the asymmetry and both the isotropic chemical shift ($\delta_{iso}$) and the quadrupolar coupling ($C_Q$) for the monoclinic phase are shown in Figure 5-14.

a)

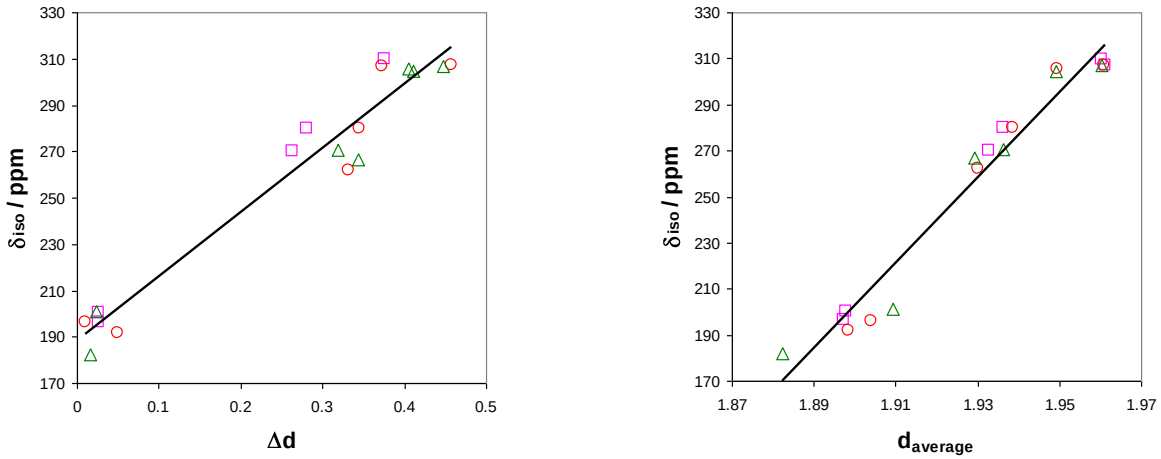


b)

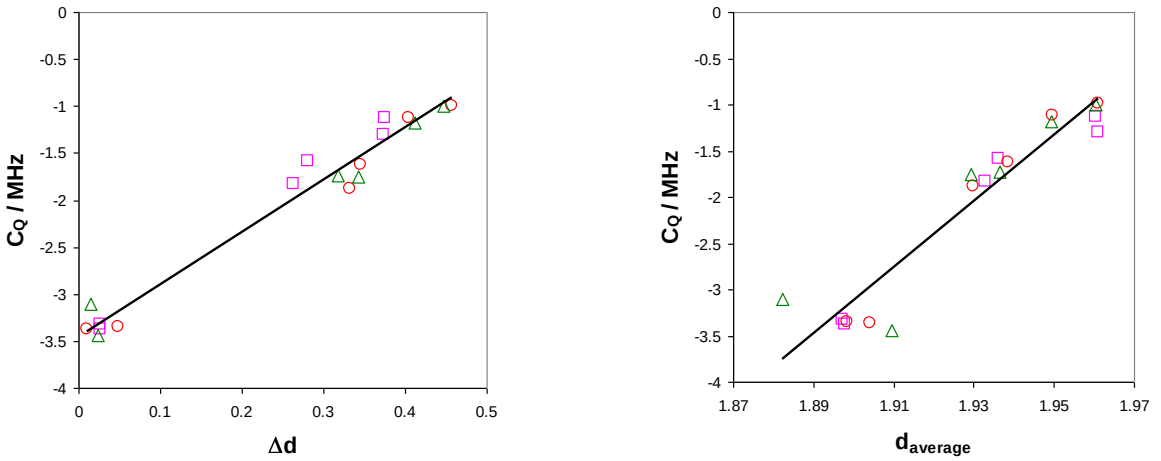


**Figure 5-14 Relationship between the W-O bond distances around a given oxygen and a) the isotropic chemical shift value and b) the quadrupolar coupling constant for the *P*2$_1$/n monoclinic form of WO$_3$. On the left hand side, the values are plotted against the asymmetry of the W-O distances around a given oxygen (Δd= d1 – d2). On the right hand side, against the average bond distances ($d_{av}$=(d1+d2)/2). The parameters calculatedfrom the GSAS, PROFILE and Howard structures are presented as squares, circles and triangles respectively.**

Looking closely at the data, consistent trends appear between the NMR and structural parameters. Both $\delta_{iso}$ and $C_Q$ tend to increase with the asymmetry of the W-O-W environment. This observation is expected for the quadrupolar coupling constant which is dependant on the asymmetry around the nucleus. More interestingly is the effect of such asymmetry on the chemical shift variation. Indeed the

isotropic chemical shift is probably the easiest parameter to extract from a MAS NMR spectrum and therefore this correlation could be an interesting tool for probing structural variations.

However, even if a linear trend seem to exists while looking at the relatively large ranges of $\delta_{iso}$ or $C_Q$, divergence from this linearity are clearly observed while looking at oxygen with similar environments (comparable $\Delta$d and $d_{av}$). This could suggest that even if these parameters have the main influence on the NMR response, other structural factors are likely to affect the response in more subtle ways.

### 5.4.2. Correlations over the $WO_3$ phase transition series

A number of interesting conclusions can be drawn by looking at the changes in calculate NMR patterns for the whole series of phase transitions which were shown in Figure 5-4. Firstly, the increase of symmetry as the temperature is increased is readily apparent. Secondly, significant shift of the overall spectrum towards higher chemical shift values is observed when passing from the $P2_1/c$ to the *Pbcn* phase. In the literature this transition is described as first order while later ones from (*Pbcn* to *Pc*) are described as second order (with some uncertainties regarding the $P\bar{1}$ to *Pc* transition). As might be anticipated NMR is thus sensitive to the relative magnitudes of changes at different transitions.

We can also explore the correlations observed between $\delta_{iso}$ and $C_Q$ with both $d_{av}$ and $\Delta$d that were apparent in the $P2_1/n$ structure to see if they hold for all the different structural models. Figure 5-15 shows equivalent plots to Figure 5-14 but for all the different phases.

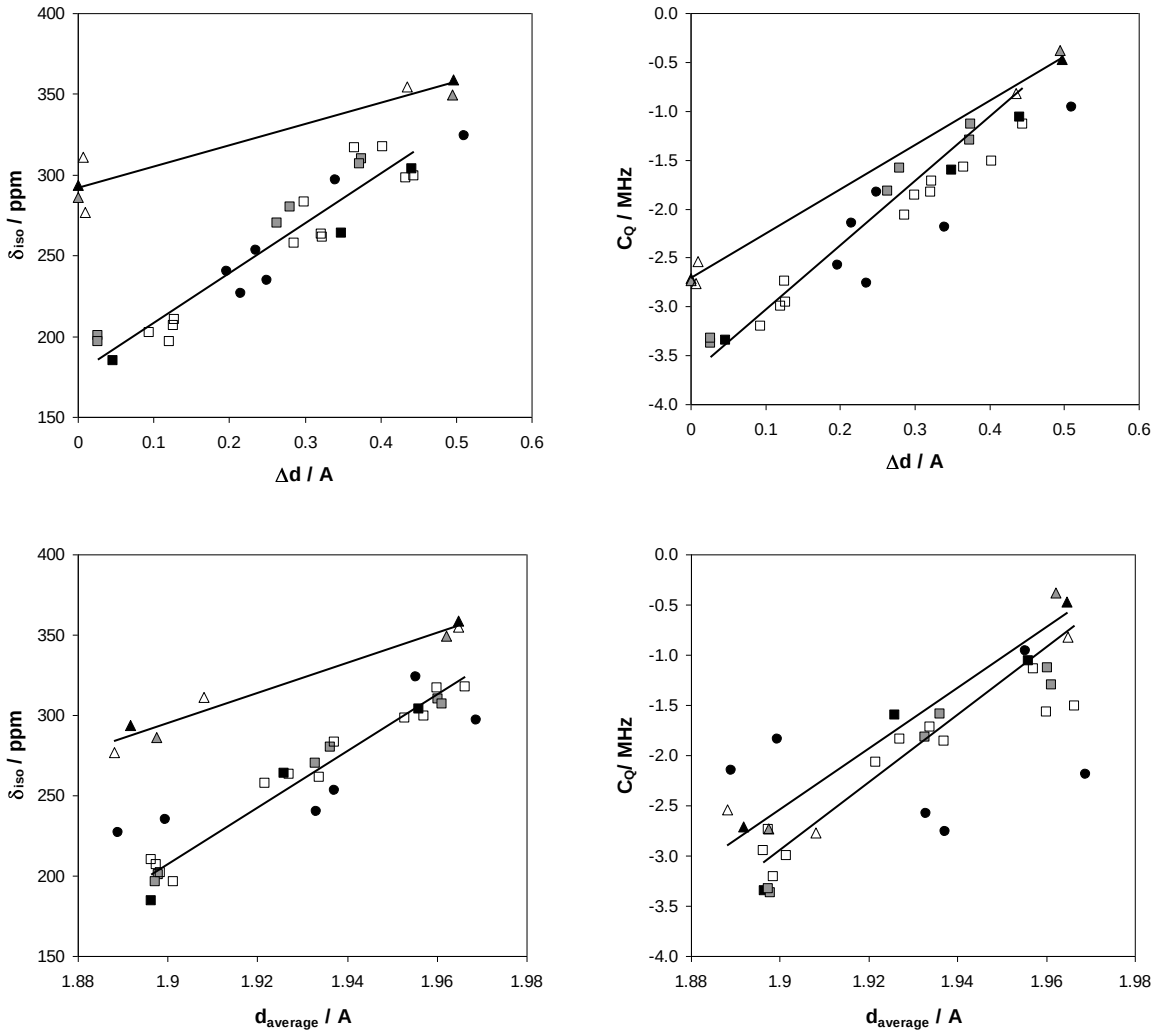


**Figure 5-15 Relationship between the asymmetry of the W-O (Δd= d1 – d2) bond distance around a given oxygen and a) its isotropic chemical shift value and b) its quadrupolar coupling constant for the seven forms of $WO_3$. The parameters from the three high temperature structures *P*4/*nmm*, *P*4/*ncc* and *P*$2_1$/*c* are presented by full, grey and empty triangles respectively. The data for *Pbcn*, *P*$2_1$/*n* and *P*$\bar{1}$ phases are represented as black, grey and white squares respectively. The parameters for the *Pc* are represented by black circles. The drawn lines show the linear regressions of the data for the high temperature phases (*P*4/*nmm*, *P*4/*ncc* and *P*$2_1$/*c*) and three of the low temperature phases (*Pbcn*, *P*$2_1$/*n* and *P*$\bar{1}$).**

Obvious correlations between the bond distances around a given oxygen and its calculated NMR patterns are observed. Clear linear correlations between the chemical shift values and both the asymmetry (Δd) and the average ($d_{av}$) of the W-O bond distances are observable. A few discrepancies from a linear correlation are observable, and a closer look at these discrepancies reveals additional interesting features. We can notice that the sets of phases related by second order phase transition (*P*4/*nmm*, *P*4/*ncc*, *P*$2_1$/*c* on one hand and *Pbcn*, *P*$2_1$/*n* and *P*$\bar{1}$ on another hand) tend to lie on separate linear trends - i.e the squares and triangles plotted show slightly different behaviours.

Some correlation is also observed between the amplitude of the $C_Q$ and both Δd and $d_{av}$ with asymmetry increasing with the increase of these two structural parameters. Although it seems that

some discrepancies remain, such behaviour is less obvious than while looking at the isotropic chemical shifts correlations.

For other systems in the literature M-O bond length has been shown to correlate both with $\delta_{iso}$ and $C_Q$ whereas $C_Q$ also correlates with M-O-M angles. Figure 5-16 shows a scatter plot of both $\delta_{iso}$ and $C_Q$ against W-O-W bond angle for all oxygens in all $WO_3$ phases.

a) b)

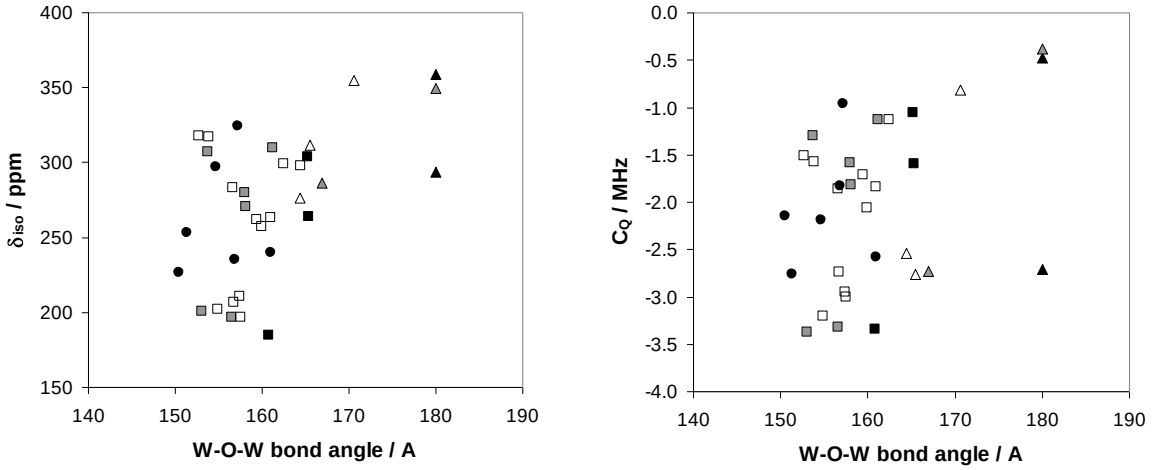


**Figure 5-16 Relationship between the W-O-W bond angles and a) the $^{17}O$ isotropic chemical shift values and b) the quadrupolar coupling constants for the seven forms of $WO_3$. The parameters from the three high temperature structures *P4/nmm*, *P4/ncc* and *P2$_1$/c* are presented by full, grey and empty triangles respectively. The data for *Pbcn*, *P2$_1$/n*, *P*$\bar{1}$ and *Pc* phases are presented as black, grey and white squares respectively. The parameters for the *Pc* are represented by black circles.**

In Figure 5-16, no obvious correlation appears between $\delta_{iso}$ or $C_Q$ and the M-O-M bond angle values.

### 5.4.3. Study of the *Pbcn* to *P2$_1$/n* phase transition

When a structure undergoes a phase transition even though the structure changes gradually, its symmetry changes abruptly. The symmetry transformation can be described by relating the "parent" and the sub-structure by irreducible representations (irrep) or distortion modes. Each distortion is associated with a structural change and is therefore likely to influence the NMR spectrum. If one knows the parent and the distorted structures and the cell relationships between them, the ISODISPLACE online tool[(16)] can be used to quantify and visualise the group theory allowed displacements that give rise to the distortions associated with a given phase transition. In this work, the amplitude of a mode describes the maximum distance by which any atom can be moved by the distortion.[b]

In its full notation, a distortion mode is written by ISODISPLACE as *Pcnb*[0,0,0]GM1+(a)[W1:d]A_3(a). *Pcnb* is the parent structure space group. k=[0,0,0] is the origin of the 1-dimensional $\Gamma_1^+$ irrep in

[b] The conventions used in ISODISPLACE to quantify the amplitudes of a mode have recently been modified but these modifications have no influence on the following discussion.

reciprocal-space, [W1:d] represents the Wyckoff site of the parent structure involved in the distortion. And point group irrep A_3 is the symmetry adapted parameter.

The distortions are labelled depending on the atom displaced by the transformation. Therefore the GM2OaA1 distortion involves the movement of the Oa atoms of the *Pbcn* structure.

$$Pm\bar{3}m\left[\frac{1}{2},\frac{1}{2},0\right]M_3^+\ \ 0,0,a\quad O:d\ \ Eu\ \ a$$

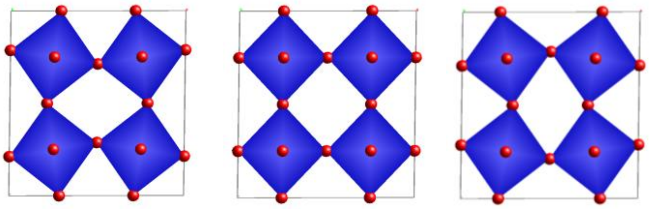


*a* = -0.30 *a* = 0 *a* = +0.30

**Figure 5-17 Sketch of the distortion modes amplitudes.**

At the phase transition temperature, the distortion mode amplitudes representing the displacement of atoms between the parent and daughter structures are zero. Therefore, we can consider the parent structure in ISODISPLACE to be the high symmetry or high temperature phase and the distorted structure to be that at lower temperature. Intermediate structures can then be generated using ISODISPLACE by varying the different distortion mode amplitudes.

In this study we have decided to focus on the *Pbcn* to $P2_1/n$ phase transition occurring at 673 K (400 °C). We have chosen this as accurate structures have been reported at temperatures just above and below the phase transition temperatures[(4)]. We can then investigate the effect of the various symmetry allowed distortion modes on the NMR by setting all their amplitudes to zero to represent the high symmetry *Pbcn* structure and adjusting them to the magnitude required to reproduce the $P2_1/n$ structure of Vogt. The ultimate goal of this study is to see whether direct relationships can be established between NMR parameters and the symmetry-allowed distortion amplitudes which are a natural language for describing the transition.

In ISODISPLACE, the two structures reported by Vogt (at 573 K and 673 K) were used. The parent structure being the more symmetric *Pbcn* (673 K) phase and the distorted structure the $P2_1/n$ structure (573 K). At the phase transition, each of the atoms present in the high temperature structure (one tungsten atom and three different types of oxygen) splits into two. Therefore the $P2_1/n$ phase has two tungsten atoms and three pairs of oxygens. Here we label the Pcnb sites as W1, Oa, Ob and Oc. These split to sites W1/W2 and oxygens O1/O2, O3/O4 and O5/O6 respectively. This transition can be described by two irreducible representations containing eleven non-zero distortion modes each (see

Table 5-3). The amplitudes of the various distortion modes are not the same and can be loosely separated in two sets. We will refer to distortions with an amplitude (maximum atom displacement) greater or equal to 0.1 as “primary distortions” as they are likely to be the one to energetically drive the phase transition and the modes with smaller amplitudes as “secondary distortions”.

**Table 5-3 Distortion modes and their amplitudes for the two irreducible representations existing between 573 K and 673 K in $WO_3$. In this table, the mode label *Pcnb*[0,0,0]GM1+(a)[W1:d]A_3(a) as described in the text is simplified as GM1W1A3 and its amplitude given.**

| GM1 | W1 A1 | W1 A2 | W1 A3 | GM2 | W1 A1 | W1 A2 | W1 A3 |
|---|---|---|---|---|---|---|---|
| | 0.011 | -0.007 | -0.003 | | -0.004 | 0.007 | 0.027 |
| | Oa A1 | Oa A2 | Oa A3 | | Oa A1 | Oa A2 | Oa A3 |
| | 0.004 | -0.008 | -0.006 | | 0.007 | -0.012 | 0.023 |
| | Ob A1 | Ob A2 | Ob A3 | | Ob A1 | **Ob A2** | Ob A3 |
| | 0.005 | 0.003 | -0.017 | | -0.015 | **0.136** | -0.027 |
| | Oc A1 | Oc A2 | Oc A3 | | Oc A1 | Oc A2 | **Oc A3** |
| | 0.016 | -0.012 | 0 | | -0.04 | 0 | **-0.114** |

We then want to see how the variation of the amplitudes of each distortion is likely to affect the NMR spectra. To simplify the problem and reduce the number of displacements to investigate, we first thought that using only the primary distortions would be sufficient to describe the evolution of the NMR and that the secondary distortions would only have a very small effect. Looking at Table 5-3, only two modes, GM2ObA2 and GM2OcA3, are primary distortions. We therefore simulated four structures for which the amplitudes of both distortions and cell parameters were varied linearly as presented in Table 5-4. Similarly, intermediate structures where all the distortions (both primary and secondary) were simultaneously introduced were generated.

**Table 5-4 Evolution of the cell parameters in $WO_3$ while varying the amplitude of the distortion modes from the structure described from 300 °C to 400 °C**

| Temperature(°C) | Relative amplitude of the distortions | a (Å) | b (Å) | c (Å) | β (°) |
|---|---|---|---|---|---|
| 300 | 1 | 7.3271 | 7.5644 | 7.7274 | 90.488 |
| | 0.8 | 7.32962 | 7.5664 | 7.73096 | 90.3904 |
| | 0.6 | 7.33214 | 7.5684 | 7.73452 | 90.2928 |
| | 0.4 | 7.33466 | 7.5704 | 7.73808 | 90.1952 |
| | 0.2 | 7.33718 | 7.5724 | 7.74164 | 90.0976 |
| 400 | 0 | 7.3397 | 7.5744 | 7.7452 | 90 |

A linear evolution of the $^{17}O$ chemical shifts was observed as the amplitudes of the distortion were varied linearly. Only the simulated spectra for the two structures obtained for relative amplitudes of 1 for all and only the primary distortions are presented in Figure 5-18. These spectra were simulated using the NMR parameters determined from CASTEP calculations on the structures generated by ISODISPLACE. The calculated spectrum for the high temperature (400 °C) *Pbcn* structure is also shown which corresponds to distortions amplitudes of zero. No noticeable differences are observed in

the quadrupolar couplings between these three spectra, therefore in the following, we will only look at the variations in chemical shifts. An initial conclusion from these simulations would be that the NMR data simulated using just two distortion amplitudes is very similar to that using all 24 distortions. O3 and O4 chemical shift differences are reproduced well although O5 and O6 differences are a little underestimated. This would be encouraging conclusion in it would suggest that $^{17}$O NMR can potentially extract information directly on the structural parameters. This conclusion should, however be taken with caution since the effects of distortions being ignored might accidentally cancel in this case. We explore this possibility below.

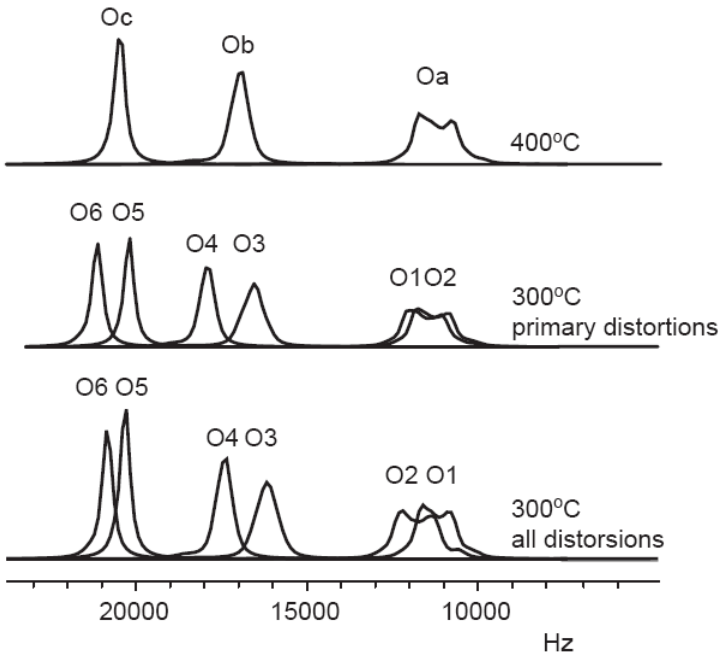


**Figure 5-18 Calculated $^{17}$O NMR spectra of the two structures obtained for relative amplitudes of 1 by varying linearly all and only the primary distortions. The calculated spectrum for the high temperature (400 °C) *Pbcn* structure is shown at the top.**

The importance of a correlation between the $^{17}$O chemical shifts and the W-O bond distances has been mentioned previously. It is then of interest to look at how those distances are modified while applying the distortions in this case. The bond distances, the asymmetry ($\Delta$d) and average $d_{av}$ around the six oxygens in $P2_1/n$ are listed in Table 5-5. The dependence of $\delta_{iso}$ and $C_Q$ on these parameters is shown in Figure 5-19.

**Table 5-5 Average bond distances and asymmetry of the W-O bond lengths of the simulated $WO_3$ obtained for structures expected at 300 °C when two main distortion (GM2ObA2 and GM2OcA3) or all the distortions involved in the *Pbcn* to *P2$_1$/n* transition are applied**

| | | O1 | O2 | O3 | O4 | O5 | O6 |
|---|---|---|---|---|---|---|---|
| Main distortions | d1 | 1.86397 | 1.86441 | 1.74885 | 1.77693 | 1.70373 | 1.72393 |
| | d2 | 1.91605 | 1.92401 | 2.11587 | 2.07431 | 2.18613 | 2.19532 |
| | Δd | 0.05208 | 0.0596 | 0.36702 | 0.29738 | 0.4824 | 0.47139 |
| | $d_{av}$ | 1.89001 | 1.89421 | 1.93236 | 1.92562 | 1.94493 | 1.959625 |
| All distortions | d1 | 1.86447 | 1.85590 | 1.81346 | 1.73670 | 1.70674 | 1.71916 |
| | d2 | 1.91670 | 1.93634 | 2.05098 | 2.11600 | 2.19392 | 2.20029 |
| | Δd | 0.05223 | 0.08044 | 0.23752 | 0.3793 | 0.48718 | 0.48113 |
| | $d_{av}$ | 1.890585 | 1.89612 | 1.93222 | 1.92635 | 1.95033 | 1.959725 |

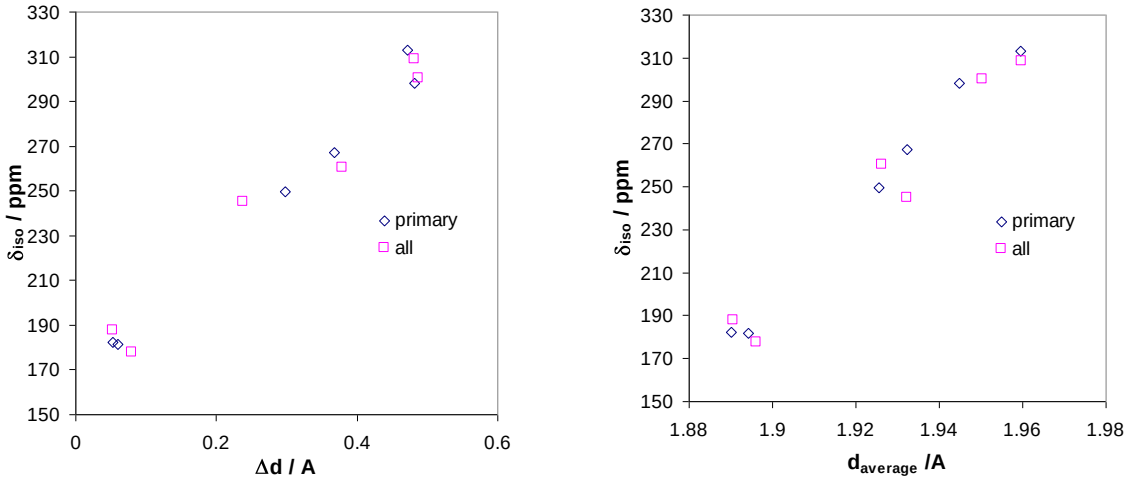


**Figure 5-19 Relationship between the W-O bond distances around a given oxygen and a) the isotropic chemical shift value and b) the quadrupolar coupling constant for the structure obtained by varying all (pink squares) distortions and only the primary distortions (blue diamonds). On the left hand side, the values are plotted against the asymmetry of the W-O distances around a given oxygen (Δd= d1 – d2). On the right hand side, against the average bond distances ($d_{av}$=(d1+d2)/2).**

The expected gross correlation between $\delta_{iso}$ and $C_Q$ for the six oxygens is shown when using either just primary distortion modes or all modes. However, the subtleties distinguishing similar sites (e.g O3 vs O4) are missed. Therefore, it seems that for atoms in very similar chemical environment, these correlations are no longer sufficient to fully describe the behaviour of the NMR response to more subtle changes.

Considering two distortions involves the displacement of two different types of atoms in the 400°C structure and makes other correlation between structure and NMR more difficult to spot. It is then interesting to simplify the problem and look at how a single distortion (displacement of a given atom) influences the NMR response of the surrounding $^{17}O$ sites. We already highlighted some correlations between W-O bond distances and the isotropic chemical shifts values.

### 5.4.4. Single distortion studies

To investigate the effect of each individual distortion amplitude mode on the NMR response, we fixed its amplitude to the values reported in Table 5-3 and set all the others to zero. In Table 5-3, the GM2OcA2 distortion is reported to have amplitude of zero. CASTEP calculations were performed on these structures and the resulting calculated NMR spectra are shown in Figure 5-20.

We focus our discussions here on the influence of the GM2 modes for brevity. The calculated spectrum in such case corresponds to the only effect of the modification of the unit cell parameters (see Table 5-5) on the NMR spectrum. This pattern can then be used as a reference from which to compare the influence of other distortions.

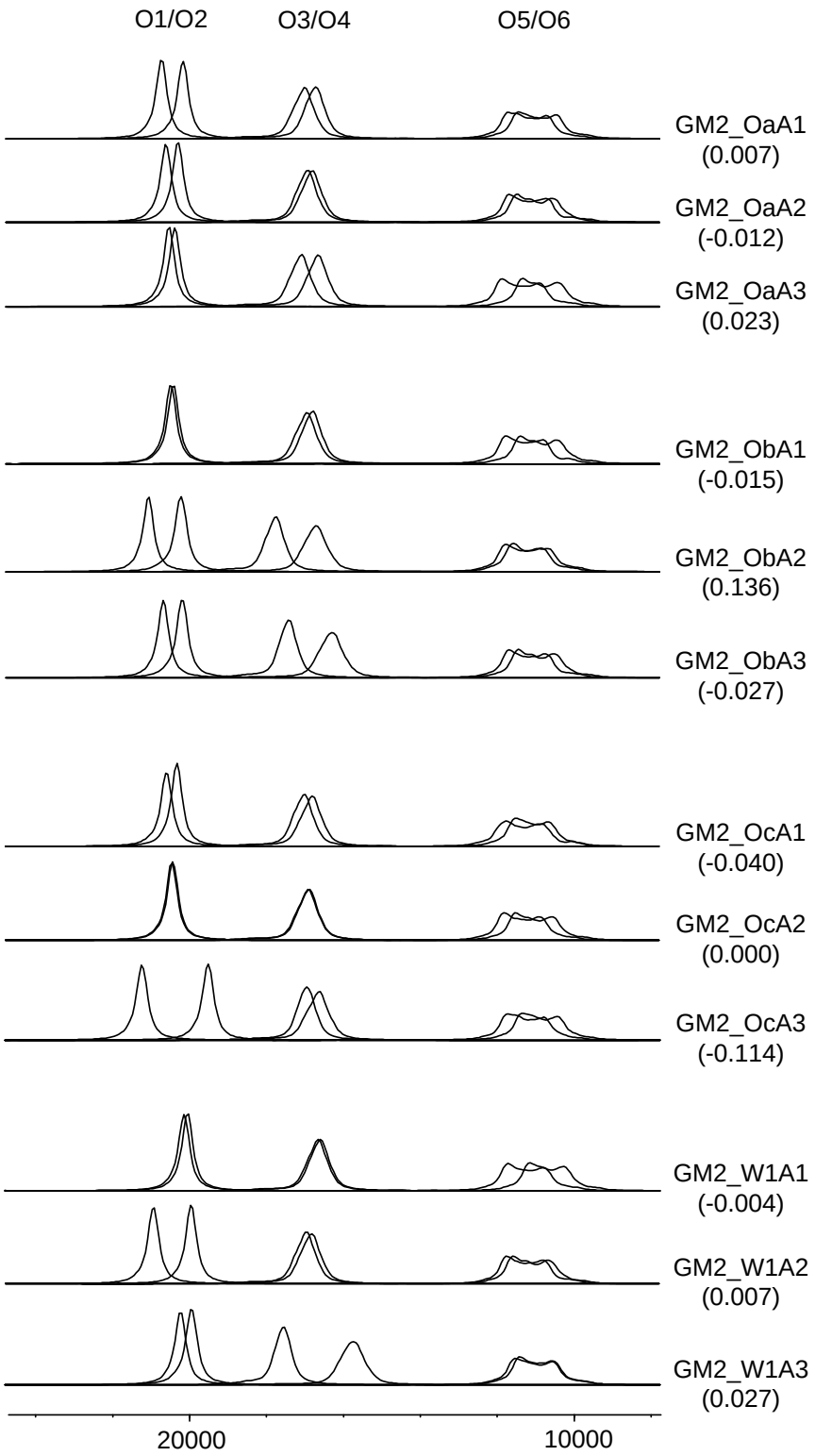


**Figure 5-20 Calculated NMR spectra obtained from the CASTEP calculations on the structures generated by ISODISPLACE with only one non-zero distortion. The labels on the right hand side of each spectrum indicate the distortion involved and the amplitude of the distortion (in brackets).**

These simulations suggest that even distortions associated with very small amplitudes (see Table 5-3) can have a dramatic effect on the NMR response relative to the GM2OcA3 reference pattern. For example, the amplitude of the GM2OaA1 mode is 0.007 but the corresponding calculated pattern shows a significant NMR response.

We will start off our argument by only looking at the GM2OaAn distortions. The asymmetry and average of the W-O bond distances resulting from the structures are listed in Table 5-6.

**Table 5-6 W-O bond distance changes due to the GM2OaAn distortion modes**

| | | O1 | O2 | O3 | O4 | O5 | O6 |
|---|---|---|---|---|---|---|---|
| GM2OaA1 | $\Delta$d | 0.0379 | 0.07378 | 0.33253 | 0.33362 | 0.48144 | 0.47395 |
| | $d_{av}$ | 1.89001 | 1.89421 | 1.924315 | 1.92445 | 1.94878 | 1.949015 |
| GM2OaA2 | $\Delta$d | 0.05498 | 0.05633 | 0.33253 | 0.33362 | 0.48144 | 0.47395 |
| | $d_{av}$ | 1.89142 | 1.892875 | 1.924315 | 1.92445 | 1.94878 | 1.949015 |
| GM2OaA3 | $\Delta$d | 0.05746 | 0.05423 | 0.33253 | 0.33362 | 0.48144 | 0.47395 |
| | $d_{av}$ | 1.88718 | 1.897305 | 1.924315 | 1.92445 | 1.94878 | 1.949015 |

Looking at the values in Table 5-6 and the calculated spectra in Figure 5-20, some obvious remarks can be made. Even though the $\Delta$d and $d_{av}$ values are vary for the O1 and O2 atoms (the ones generated by the displacement of Oa), the NMR responses calculated for O3, O4, O5 and O6 are very different. This suggests that considering only the effect of the W-O bond distances observed in our previous studies is not sufficient to explain the $^{17}$O NMR behaviour of $WO_3$.

Similar observations are made when looking at the GM2ObAn and GM2OcAn distortions as the only differences in distances are due to the movement of the Ob and Oc atoms from *Pbcn* structure respectively. These modes would therefore only be expected to influence O3/O4 and O5/O6 respectively whereas changes are seen elsewhere.

In the case of W1 displacements, the trend reported in our earlier studies is confirmed ($\delta_{iso}$ increases with $d_{av}$ and $\Delta$d) so we will from now only consider the effect of the oxygen displacements.

The correlation between W-O bond distances and $\delta_{iso}$ described in previous sections is insufficient to describe fully influence of the structure on the $^{17}$O NMR behaviour. We can therefore consider each oxygen as being at the centre of a larger atomic arrangement. In the $WO_3$ structure, each oxygen can be represented as the centre of a distorted cube which geometry is defined as shown in Figure 5-21.

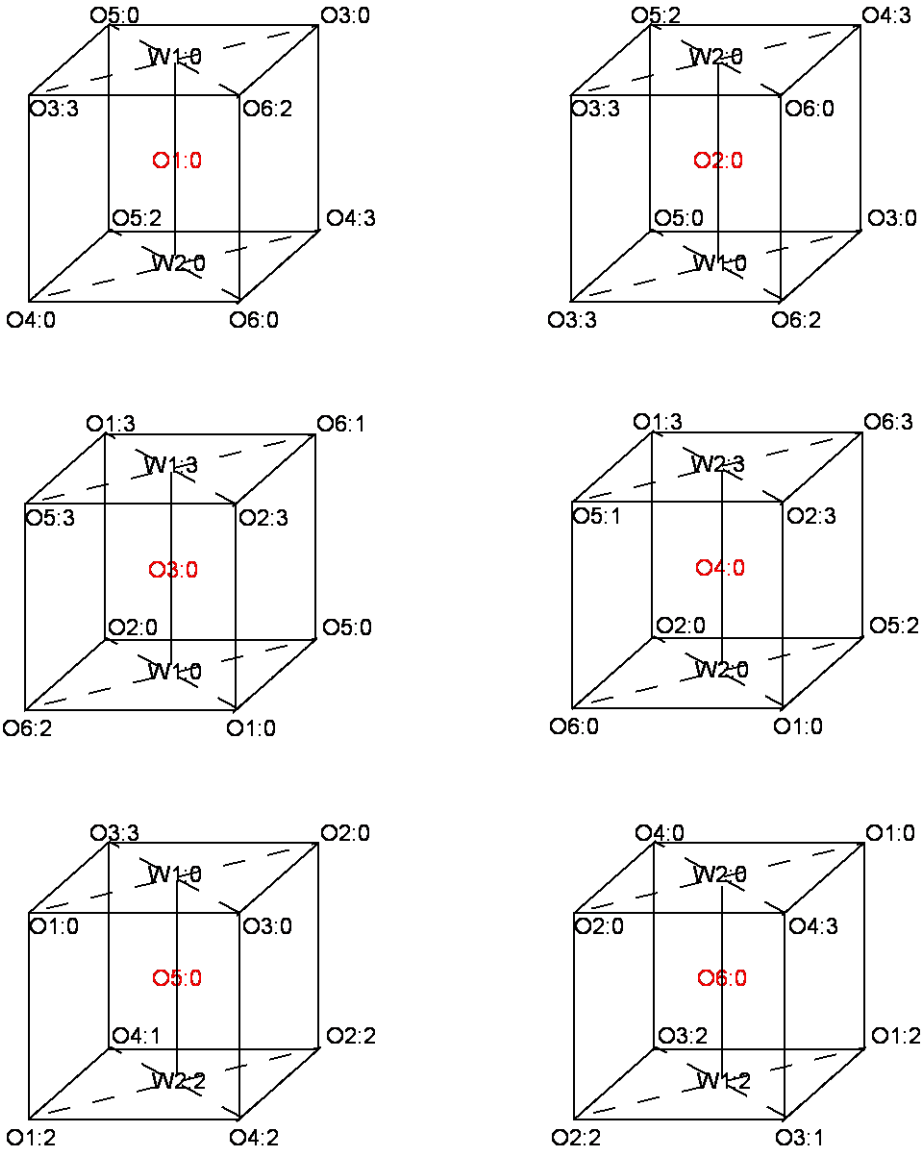


**Figure 5-21 Schematic representations of the oxygen environments in the distorted *Pbcn* structure**

In this representation, we see that a large number of parameters can potentially modify the oxygen environment and therefore influence the NMR responses. However, the problem is hugely simplified while looking at a single distortion, as only the distances associated with the displacement of one oxygen in the parent phase (*Pbcn*) are modified. For consistency with our previous studies and to simplify further the investigations, we decided here not to consider the influence of the different bond angles.

If we consider a non-zero Oa distortion, all the distances around O1 and O2 will be modified, in such case, we will look only at the changes in distances around O3, O4, O5 and O6 for which it turns out that only four of the relative surrounding atoms positions are modified. A representation of the different W-O distances that arise around O3 and O4 is given below for the three GM2Oa distortions (Figure 5-22). Similar data for O5 and O6 are shown later.

We first consider O3 and O4 that can be distinguished from the other oxygens in the $WO_3$ structure as they form chains involving only two types of atoms (O3/W1 and O4/W2 respectively) across the structure. Therefore, they are surrounded by two exactly identical types of octahedra to which they are connected through different bond lengths. Moreover, the asymmetry of the W-O bonds around these two oxygens is larger than the one around O1/O2 and smaller than around O5/O6. The differences in chemical shifts values between these two oxygens are therefore expected to depend mainly on the differences between the $W1O_6$ and $W2O_6$ octahedra.

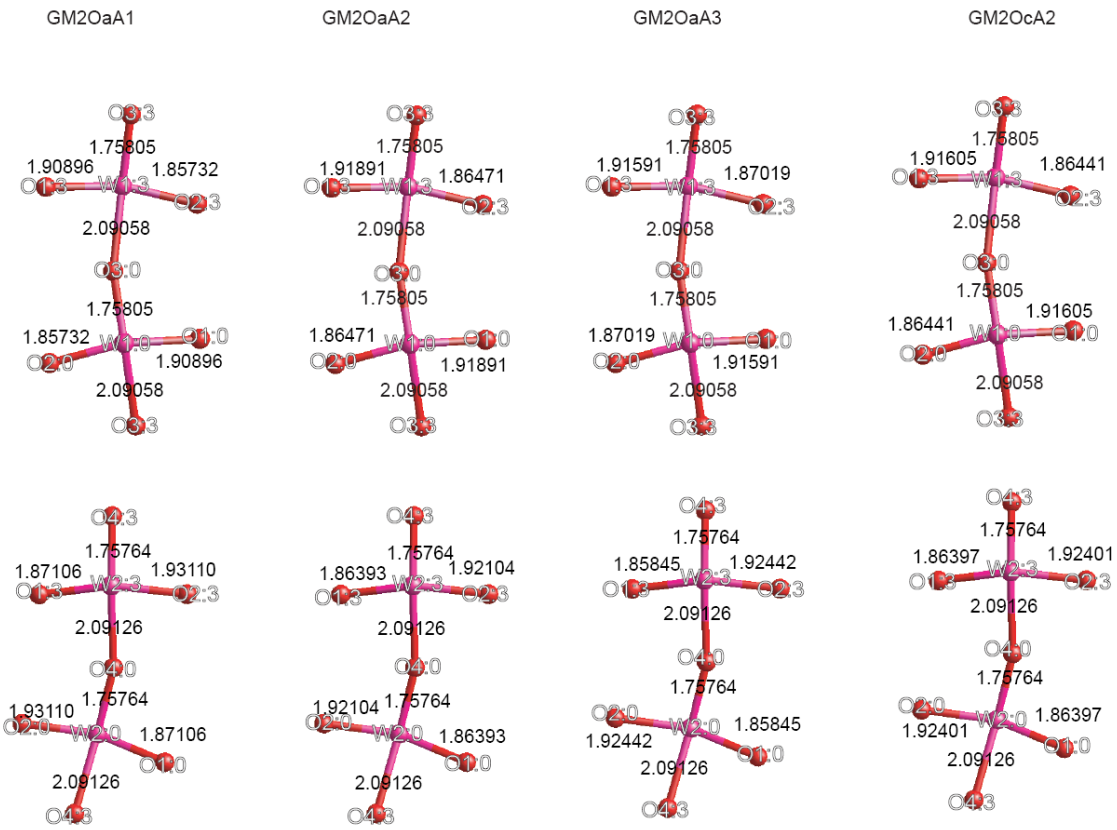


**Figure 5-22 W-O bond lengths around O3 and O4 in $WO_3$ structure for different distortion modes.**

Looking at the bond distances in Figure 5-22, the reference structure "GM2OcA2" and "GM2OaA2" present very similar $W1O_6$ and $W2O_6$ octahedra. These similarities are reflected in the O3/O4 chemical shifts in the calculations in Figure 5-20. The two octahedra around O3 and O4 in the GM2OaA1 and GM2OaA3 structures are, however, quite different which is also reflected in the chemical shifts of the two oxygens sites. However Figure 5-20 suggests more differences in between O3 and O4 environments when applying the GM2OaA1 than GM2OaA3 but the NMR shift does not exactly reveal this feature.

The geometry of the $WO_6$ octahedra seems to some extent to influence the NMR behaviour of O3 and O4. However we can also suppose that through-space O-O interactions may be of importance. The O-O bond distances for the corresponding distortions are presented in Table 5-7. In this table, the O-O bond distances around O3 and O4 are denoted D1, D2, D3, D4 and $\Delta$1, $\Delta$2, $\Delta$3, $\Delta$4 respectively

**Table 5-7 O-O distances around O3 and O4 for selected distortion modes**

| | | GM2OaA1 | GM2OaA2 | GM2OaA3 | GM2OcA1 | GM2OcA2 | GM2OcA3 |
|---|---|---|---|---|---|---|---|
| O3 | D1 | 2.61197 | 2.61652 | 2.60406 | 2.68765 | 2.61774 | 2.6436 |
| | D2 | 2.61753 | 2.62265 | 2.60409 | 2.70732 | 2.62199 | 2.713 |
| | D3 | 2.70316 | 2.70682 | 2.72702 | 2.72053 | 2.70741 | 2.76053 |
| | D4 | 2.70704 | 2.71389 | 2.72586 | 2.78822 | 2.71267 | 2.7934 |
| O4 | Δ1 | 2.62752 | 2.6229 | 2.63553 | 2.66833 | 2.62174 | 2.59679 |
| | Δ2 | 2.62811 | 2.62317 | 2.64159 | 2.71551 | 2.62363 | 2.6286 |
| | Δ3 | 2.71325 | 2.70973 | 2.69061 | 2.72016 | 2.70897 | 2.79957 |
| | Δ4 | 2.72221 | 2.71525 | 2.70235 | 2.78911 | 2.71657 | 2.86842 |

The O-O bond around O3 and O4 distances obtained for a given distortion mode were compared by evaluating $D_{OO} = \sqrt{(D1-\Delta1)^2 + (D2-\Delta2)^2 + (D3-\Delta3)^2 + (D4-\Delta4)^2}$ . The $D_{OO}$ values obtained and the corresponding difference between O3 and O4 isotropic chemical shifts are reported in Table 5-8.

**Table 5-8 $D_{OO}$ and O3/O4 calculated chemical shifts differences ($\delta_{iso}$(O3)–$\delta_{iso}$(O4)) obtained from structures generated from distortions involving displacements of the Oa and Oc oxygens in the high temperature structure.**

| | GM2OaA1 | GM2OaA2 | GM2OaA3 | GM2OcA1 | GM2OcA2 | GM2OcA2 |
|---|---|---|---|---|---|---|
| $D_{OO}$ | 0.020325 | 0.003898 | 0.065066 | 0.019381 | 0 | 0.122601 |
| $\delta_{iso}$(O3)–$\delta_{iso}$(O4) | 4.4886 | 1.5825 | 5.936 | 2.6078 | 0.55 | 3.3285 |

The amplitude of the chemical shift difference seems to be somehow correlated to $D_{OO}$. Due to the small number of data points no definitive conclusions can be drawn, however it is interesting to visually picture this behaviour (Figure 5-23).

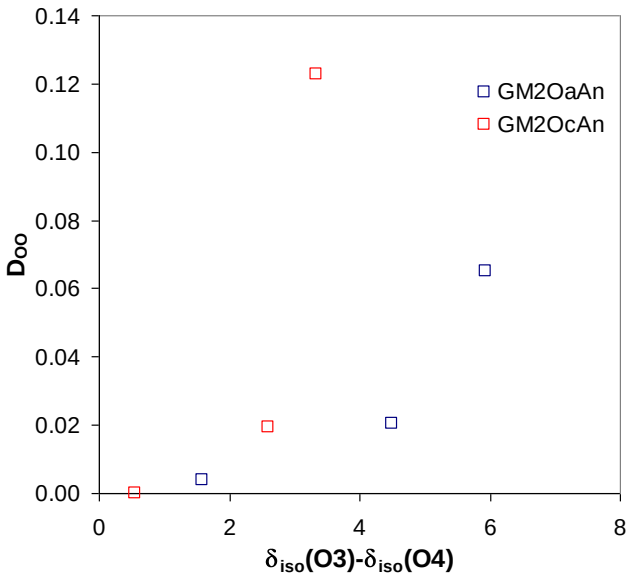


**Figure 5-23 Correlation between O-O bond distances and $^{17}$O chemical shift differences**

Although the trend is not entirely consistent between the distortions involving the displacement of Oa and Oc, the O-O bond distance as well as the W-O bond distances seem to have a consistent effect on the NMR behaviour of O3 and O4.

### 5.4.5. O1/O2 and O5/O6

Unlike O3 and O4, O1/O2 and O5/O6 form chains involving four different types of atoms (O1/W1/O2/W2 and O5/W1/O6/W2 respectively) across the structure. Therefore, the comparison of their octahedral environment is likely to more complex that for O3 and O4 for which the surrounding octahedra were identical. More over, the asymmetry of the W-O bonds around O3/O4 is larger than the one around O1/O2 and smaller than around O5/O6.

O1 and O2 are the oxygens with the most similar W-O bond distances. Therefore we may expect some consistent effect of the surrounding (W-O and OO distances) on the chemical shift values variations. O5 and O6 however show the greatest W-O asymmetry and therefore may be expected to show a more complicated NMR response.

The schematic representation of the W-O bond distances around O1/O2 and O5/O6 are shown in Figure 5-24 and Figure 5-25 respectively. The $D_{OO}$ and isotropic chemical shift values are shown in Table 5-9 and Table 5-10.

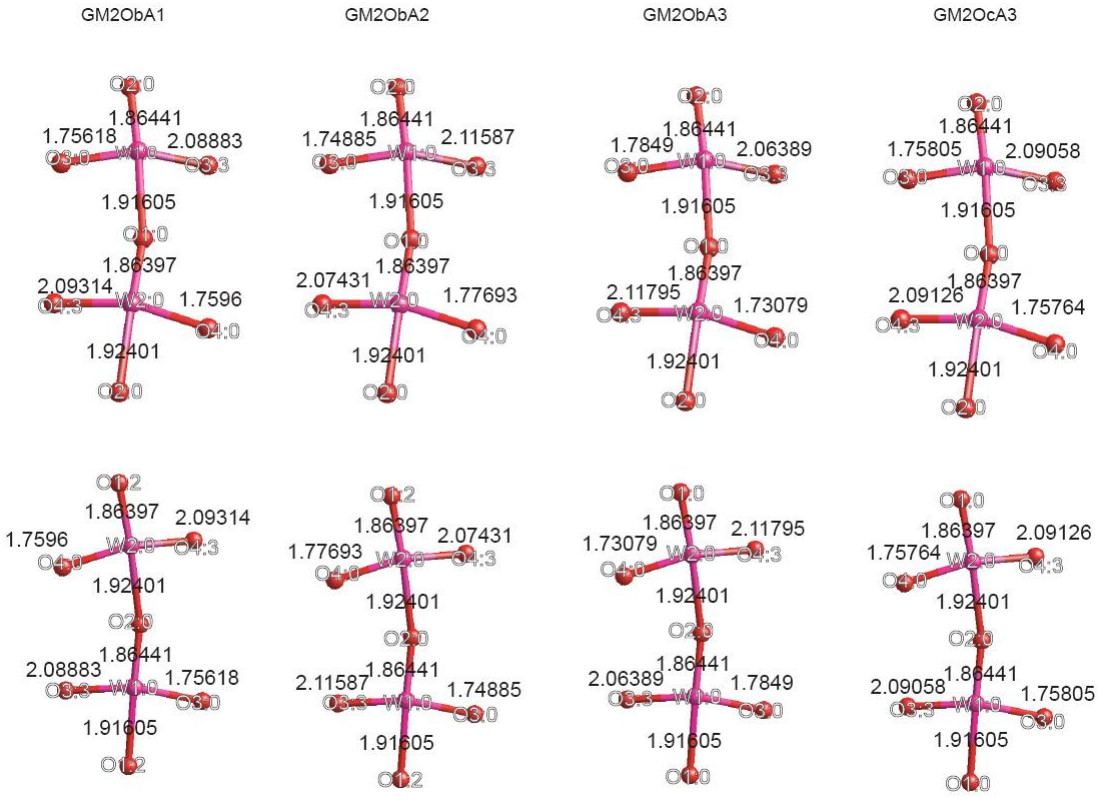


**Figure 5-24 W-O bond lengths around O1 and O2 in $WO_3$ structure for different distortion modes**

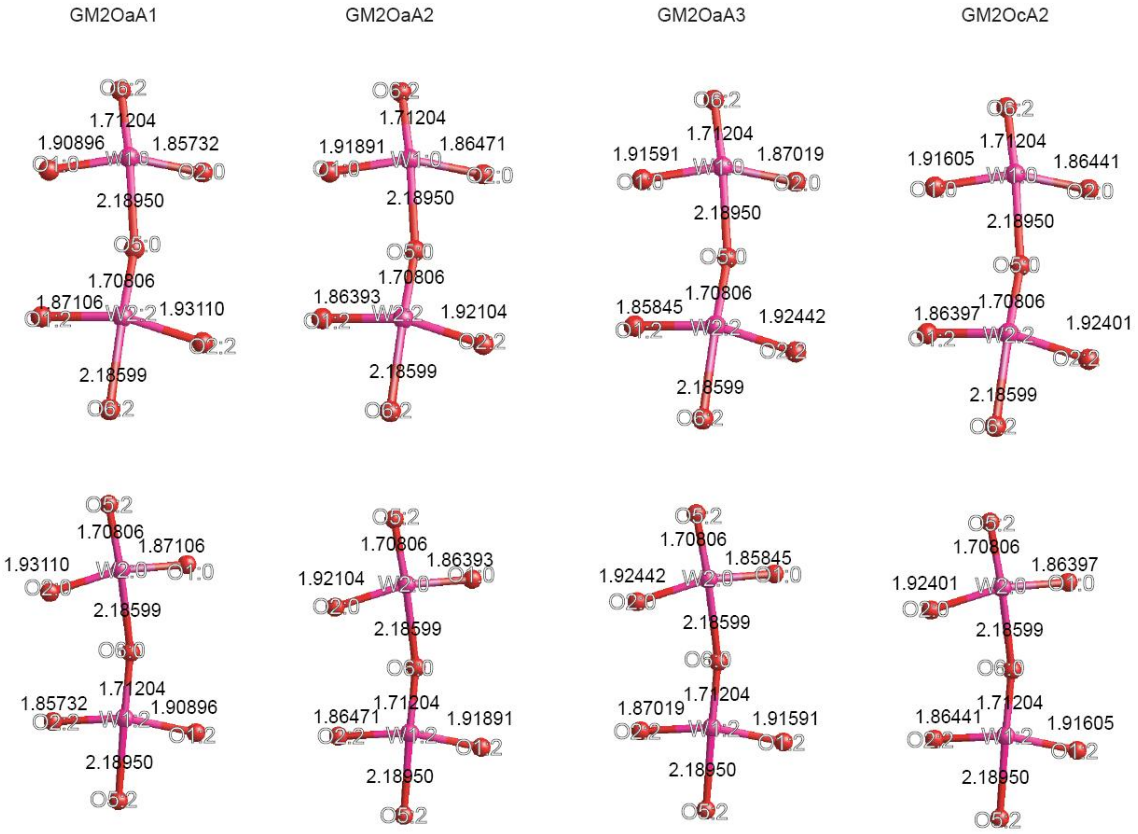


**Figure 5-25 W-O bond lengths around O5 and O6 in $WO_3$ structure for different distortion modes**

From these two figures and the chemical shift values reported in Tables 9 and 10, no correlation between the different W-O bond distances and the isotropic chemical shift seem to be obvious even when looking at the more symmetric O1/O2 environment.

**Table 5-9 $D_{OO}$ and O1/O2 calculated chemical shifts differences ($\delta_{iso}$(O1)–$\delta_{iso}$(O2)) obtained from structures generated from distortions involving displacements of the Ob and Oc oxygens in the high temperature structure.**

| | GM2ObA1 | GM2ObA2 | GM2ObA3 | GM2OcA1 | GM2OcA2 | GM2OcA2 |
|---|---|---|---|---|---|---|
| $D_{OO}$ | 0.040369 | 0.048691 | 0.036784 | 0.108064 | 0 | 0.016574 |
| $\delta_{iso}$(O1)–$\delta_{iso}$(O2) | -5.2372 | -2.4838 | -3.279 | 5.2465 | -4.484 | -5.8259 |

**Table 5-10 $D_{OO}$ and O5/O6 calculated chemical shifts differences ($\delta_{iso}$(O5)–$\delta_{iso}$(O6)) obtained from structures generated from distortions involving displacements of the Oa and Ob oxygens in the high temperature structure.**

| | GM2OaA1 | GM2OaA2 | GM2OaA3 | GM2ObA1 | GM2ObA2 | GM2ObA2 |
|---|---|---|---|---|---|---|
| $D_{OO}$ | 0.006297 | 0.2169 | 0.007241 | 0.057392 | 0.151804 | 0.073663 |
| $\delta_{iso}$(O5)–$\delta_{iso}$(O6) | 7.9666 | 4.6403 | -2.1938 | 0.8853 | 11.7595 | -6.846 |

## 5.5. Conclusions

$WO_3$ shows complicated phase transitions and the $^{17}O$ NMR patterns of the phases present a different temperature have been calculated using CASTEP. These calculations can be used to correlate structural features to NMR parameters that would be difficult to extract otherwise.

We showed that X-ray diffraction NMR and DFT calculations can bring new insights to some controversies on the phases present below room temperature in $WO_3$. $W^{17}O_3$ enriched samples were synthesised and the synthetic route used seems to have an effect on the quality of the sample as well as on the phase transition temperatures.

Observing the $^{17}O$ NMR signal at room temperature using our enriched sample was possible and our observed experimental spectrum matches the DFT calculations obtained for the $P2_1/n$ structure. We do show that the NMR data can help distinguishing closely related models in the literature. NMR seems more sensitive to subtle structural distortions than even neutron powder diffraction.

Combining low temperature X-ray and NMR observations, we have been able to measure $^{17}O$ NMR spectra of the Pc phase for the first time. Significant changes in the observed pattern confirm CASTEP calculations and the high sensitivity of the NMR methods for following subtle transitions.
Analysis by Rietveld was performed using the three low temperature structures but there is some issues of the existence of an extra phase present at low temperatures.

We have also attempted to relate the local structure of oxygens to NMR parameters. Looking at the influence of structural variations on the NMR spectra, some correlations have been found. At a crude level we have shown a clear relationship between $\delta_{iso}$ and $C_Q$ with both the asymmetry and the average bond distances around a given oxygen ($\Delta d$ and $d_{av}$).

We have also attempted to use distortion mode amplitudes to try and probe more subtle relationships between NMR and structural parameters. It is clear from these studies that whilst broad correlations can be observed, relatively minor distortions can also have significant effects on calculated parameters. Such relatonships have emerged but further investigation is needed to fully understand all effects.

For O3-W1-O3-W1 and O4-W2-O4-W2 a consistent trend has been found between the isotropic chemical shifts and the O-O distances. For O1-W1-O2-W2 and O5-W1-O6-W2 chains, no clear correlation is observed but again a combined influence of the W-O and O-O distances is probable.

Further analysis using more complex mathematical procedures such as PCA (Principal Component Analysis) could be used in future works to quantify the effect of the different changes in the oxygen environments.

## 5.6. References


1. W. L. Kehl, R. G. Hay, D. Wahl, *Journal of Applied Physics* **23**, 212-215 (1952).
2. K. R. Locherer, J. Chrosch, E. K. H. Salje, *Phase Transitions* **67**, 51-63 (1998).
3. C. J. Howard, V. Luca, K. S. Knight, *Journal of Physics: Condensed Matter* **14**, 377-387 (Jan 28, 2002).
4. T. Vogt, P. M. Woodward, B. A. Hunter, *Journal of Solid State Chemistry* **144**, 209-215 (Apr, 1999).
5. G. Andersson, *Acta Chemica Scandinavica* **7**, 154-158 (1953).
6. S. Tanisaki, *J. Phys. Soc. Jpn.* **15**, 566-573 (1960).
7. P. M. Woodward, A. W. Sleight, T. Vogt, *Journal of Physical Chemistry in Solids* **56**, 1305-1315 (Oct, 1995).
8. A. M. Glazer, *Acta Crystallographica Section A* **31**, 756-762 (1975).
9. B. T. Matthias, E. A. Wood, *Physical Review* **84**, 1255-1255 (1951).
10. P. M. Woodward, A. W. Sleight, T. Vogt, *Journal of Solid State Chemistry* **131**, 9-17 (Jun, 1997).
11. S. Allen, *PhD thesis, Durham University* (2003).
12. I. J. King, *PhD thesis, Durham University* (2003).
13. R. A. Robinson, A. C. Lawson, A. C. Larson, R. B. Vondreele, J. A. Goldstone, *Physica B.* **213**, 985-989 (Aug, 1995).
14. J. K. Crockroft, *http://img.chem.ucl.ac.uk/www/cockcroft/profil.htm*.
15. G. W. Stinton, J. S. O. Evans, *Journal of Applied Crystallography* **40**, 87-95 (Feb, 2007).
16. B. J. Campbell, H. T. Stokes, D. E. Tanner, D. M. Hatch, *Journal of Applied Crystallography* **39**, 607-614 (2006).

# Chapter 6. Conclusions and future work

In this thesis, new ways of combining experimental and theoretical techniques have been investigated and shown to open great prospects for investigations of crystalline materials. Although the two analytical techniques (X-ray diffraction and solid-state NMR) are routinely allied for structure determination in crystalline samples, recent progress in calculating properties in the solid state by density functional theory (DFT) can be brought in as an invaluable third technique to validate the structures proposed by X-ray and/or correlate structural information to the NMR data .

In the case of $(MoO_2)_2P_2O_7$, early diffraction studies revealed only an approximate structure and hinted at the existence of a superstructure at room temperatures. However, the displacements of the light atoms (oxygen and phosphorus) responsible for this decrease of symmetry are barely observable using standard X-ray equipment and new attempts to determine this structure were performed. Variable-temperature $^{31}P$ solid-state NMR clearly revealed continuous structural changes of the phosphorus environments. Quantitative analysis of the different NMR $^{31}P$ signals as well as techniques exploiting dipolar and scalar couplings between the $^{31}P$ nuclei were used to differentiate between different models compatible with diffraction data analysis. In pyrophosphates, the nature of the high to lower symmetry transition is explained by the existence of a wider range of P-O-P bond angles values in the lower symmetry structure. Looking at the structure and the NMR experimental data, The $^{31}P$-$^{31}P$ $^2J$ coupling and the $^{31}P$ chemical shift values were shown to be influenced by the P-O-P bond angles. Ab initio calculations on model structures confirmed these assumptions showing that the J-coupling values increase with the P-O-P angle. The P1/P2 chemical shift difference tends to decrease for larger P-O-P values with a possible swapping of the P1/P2 resonance frequencies when passing through a specific P-O-P bond angle value. The results of the DFT calculations, combined with 2D dipolar and J-coupling experiments, were used to propose an assignment of the $^{31}P$ signals from $(MoO_2)_2P_2O_7$.In future studies, more detailed investigations in the intermediate phase (existing between 30°C and 110°C) will be considered. J-coupling measurements can give information on a possible gradual evolution of the P-O-P angle values. Recent developments in calculating J-couplings by DFT could also be exploited. The results could be compared to the J-coupling values obtained experimentally on high and low temperature structures. Geometry optimization DFT methods can also be used to optimize model high temperature structures as an alternative method to DLS with intermediate bond angle values and to perform calculations of NMR parameters. These methodologies could then be extended to other isostructural $A_2P_2O_7$ structures (A=Mg, Ca) and pyrophosphates.

In $Zr_2WO_8$, $^{17}O$ spectra of the three phases generated at different pressures were recorded and are consistent with the structures proposed by diffraction studies in earlier publications. The determination of the NMR parameters using DFT calculations performed on the two crystalline phases ($\alpha$ and $\gamma$) show good agreement with the experimental results. These results confirm the $^{17}O$ chemical shift assignment in the $\alpha$-phase and suggest that the $^{17}O$ chemical shift is influenced by the nature of the

bonding cations around the oxygens in the $\gamma$-phase with the W-$^{17}$O-W and Zr-$^{17}$O-W chemical shifts being clearly separated. In the amorphous phase, the $^{17}$O spectrum clearly rules out the hypothesis that this phase could be a mixture of $WO_3$ and $ZrO_2$. For better understanding of the $\gamma$-phase, complementary NMR experiments could potentially be performed to extract the $^{17}$O oxygen quadrupolar parameters (quadrupolar couplings and asymmetry). The comparison with EFG parameters obtained from our calculations could potentially be exploited for further assignment. DLS-constrained models in combination with ab-initio calculations also confirmed a proposed mechanism for the negative thermal expansion (NTE) in the $\alpha$-phase. Very subtle linear $^{17}$O chemical shift variations were observed experimentally as a function of temperature and reproduced with our calculations on modelled structures. It would also be interesting to similarly investigate the behaviour of the $^{17}$O chemical shift in the $\gamma$-phase during the NTE process.

The final chapter aims to investigate $WO_3$ by $^{17}$O NMR. The determination of the structures and phase transition temperatures in this material are of considerable complexity. DFT calculations performed on the seven $WO_3$ structures reported at different temperatures suggest that the $WO_3$ phases should easily be distinguished by $^{17}$O MAS NMR. Enrichment procedures were therefore performed for observing the structures existing at room temperature and below with our standard NMR equipment. The $^{17}$O enrichment route described by a previous student was reproduced and variable temperature experiments were performed. We show by powder X-ray diffraction that the phase transition temperature and the quality of the sample are very sensitive to cooling rate over the synthesis process. After several attempts, a phase transition was observed by $^{17}$O and, by comparison with simulated spectra based on DFT calculations, the two observed phases are thought to be the $P2_1/n$ and Pc phases, which are present over significantly different temperature ranges to the ones reported in the literature. X-ray experiments showed a restricted temperature domain of existence and the small proportion of conversion into $P\bar{1}$ on cooling. For these reasons and considering the low $^{17}$O signal to noise ratio, we can understand why this intermediate phase was not observed during our NMR experiment. However, the $P\bar{1}$ phase can be “captured” by heating the sample back from very low temperature as it then remains the stable form at room temperature. This process could allow the $P\bar{1}$ form to be observed using $^{17}$O NMR.Considering the parameters obtained by our DFT calculations, we observed some interesting trends. The asymmetry and average values of the bond distances around a given oxygen appear to be linearly correlated to some of NMR parameters over the whole $^{17}$O chemical shift range for a given phase. The slope of this linear trend seems to be similar for phases related by second order phase transitions while the slope changes significantly between set of phases separated by first order transition. When then looking at smaller chemical shift ranges (i.e oxygens with more similar environments), correlations between the structural and NMR parameters are less obvious. Preliminary studies suggest that taking into account only the distances of the oxygens to their bonded atoms is insufficient. A detailed and rigorous statistical analysis using techniques such as Principal Component Analysis to correlate the different structural parameters (bond angles and

distances) to NMR features could potentially bring great new insight into the subtle structural significance of changes in $^{17}O$ NMR pattern.